

JGR Space Physics



RESEARCH ARTICLE

10.1029/2023JA031734

Key Points:

- Europa's plasma interaction and induced magnetic field cause only subtle changes to energetic electron influx patterns on the moon's surface
- Integrated across Europa's entire surface, impinging magnetospheric electrons deposit a similar amount of energy as magnetospheric ions
- Magnetospheric electron and ion impacts release comparable numbers of oxygen molecules from Europa's surface into the moon's exosphere

Correspondence to:

P. Addison,
paddison6@gatech.edu

Citation:

Addison, P., Liuzzo, L., & Simon, S. (2023). Surface-plasma interactions at Europa in draped magnetospheric fields: The contribution of energetic electrons to energy deposition and sputtering. *Journal of Geophysical Research: Space Physics*, 128, e2023JA031734. <https://doi.org/10.1029/2023JA031734>

Received 29 MAY 2023
Accepted 8 AUG 2023

Surface-Plasma Interactions at Europa in Draped Magnetospheric Fields: The Contribution of Energetic Electrons to Energy Deposition and Sputtering

Peter Addison¹ , Lucas Liuzzo² , and Sven Simon^{1,3} 

¹School of Earth and Atmospheric Sciences, Georgia Institute of Technology, Atlanta, GA, USA, ²Space Sciences Laboratory, University of California, Berkeley, CA, USA, ³School of Physics, Georgia Institute of Technology, Atlanta, GA, USA

Abstract We calculate the time-varying spatial distribution of energetic magnetospheric electron influx onto Europa's surface by combining a hybrid model of the moon's draped electromagnetic environment with a relativistic particle tracer. We generate maps of the energetic electron influx patterns at four distinct locations of Europa relative to the center of the Jovian magnetospheric current sheet. For a full synodic rotation of Jupiter, these results are applied to constrain the averaged number and energy influx patterns as well as the O₂ sputtering rates associated with energetic electron precipitation. We also determine the relative contributions of magnetospheric ions and electrons to surface erosion and exospheric genesis at Europa. Our major results are: (a) Except for a small region near Europa's downstream apex, the moon's entire surface is exposed to heavy irradiation by magnetospheric electrons. (b) The spatial distribution of energetic electron influx onto Europa's surface is only slightly modified by field line draping and the induced magnetic field from the moon's subsurface ocean. (c) The contributions of magnetospheric electron and ion impacts to energy deposition onto Europa's surface are of the same order of magnitude. (d) Within uncertainties, impinging magnetospheric electrons and ions make similar contributions to O₂ sputtering from Europa's surface. (e) The spatial distribution of electron energy influx and the observed concentrations of sulfuric acid (H₂SO₄) are only weakly correlated, suggesting that energy deposition by magnetospheric electron impacts is not a necessary agent for H₂SO₄ production within Europa's surface.

1. Introduction

Europa, the smallest of the Galilean moons of Jupiter (radius $R_E = 1,561$ km), orbits its parent planet at an average distance of 9.4 Jupiter radii ($R_J = 71,492$ km). As such, the moon is located deep within Jupiter's magnetosphere, and is exposed to continual bombardment from charged magnetospheric particles. This influx of charged particles erodes and chemically alters Europa's icy surface, causing various global asymmetries in its surface coloration and albedo observed by the Hubble Space Telescope (HST), the Galileo spacecraft, and Earth-based telescopes (e.g., Hendrix et al., 2011; Ligier et al., 2016; McEwen, 1986). Magnetospheric particle impacts also sputter material from Europa's surface, generating a tenuous exosphere surrounding the moon (Johnson et al., 2009; Plainaki et al., 2013; Vorburger & Wurz, 2018). Sputtered particles which escape Europa's gravitational influence populate a neutral torus along the moon's orbit (Mauk et al., 2004; Smith et al., 2019).

Jupiter's internal magnetic field is approximately dipolar at Europa's orbital distance, with a maximum 15% contribution from the quadrupole moment to any of the field components (Connerney et al., 2022). Ionization of neutral matter emitted from Io's volcanoes supplies a disc-like plasma sheet located near the planet's centrifugal equator, which extends beyond the orbits of the Galilean satellites (e.g., Connerney et al., 1981; Khurana et al., 2022). The plasma within this sheet approximately corotates with Jupiter in the inner and middle magnetosphere (e.g., Bagenal et al., 2016; Connerney et al., 1981). Azimuthal currents within the plasma sheet cause the quasi-dipolar Jovian field lines to stretch outward, generating a significant radial (relative to Jupiter's rotation axis) component of the magnetic field above and below the center of the sheet. Voyager and Galileo era descriptions of the Jovian magnetospheric field (Connerney et al., 1998; Khurana, 1997) have recently been honed by data from the Juno spacecraft (e.g., Connerney et al., 2020, 2022; Momoki & Toh, 2022; Wang et al., 2021), whose polar orbit and many magnetodisc crossings allowed for refinement of both the internal and external field models.

The 9.6° tilt between Jupiter's magnetic and rotational axes causes the planet's magnetic equator and the equatorial plasma sheet to continuously “sweep” above and below Europa over the course of a synodic rotation (≈ 11 hr).

©2023. The Authors.

This is an open access article under the terms of the [Creative Commons Attribution License](https://creativecommons.org/licenses/by/4.0/), which permits use, distribution and reproduction in any medium, provided the original work is properly cited.

As such, the ambient magnetospheric field vector at Europa's position periodically varies. The Galileo spacecraft found that this variation is strongest (approximately half of the overall field strength $|B_0|$) in the magnetic field component along the Europa-Jupiter line, although a weak variation of 20% of the total field strength was also found in the component along the moon's orbital direction (Kivelson et al., 1999, 2000). Europa is continually exposed to the flow inside the Jovian plasma sheet, which overtakes the moon's orbital trailing hemisphere at a relative velocity of approximately 100 km/s, roughly 85% of the corotation speed (e.g., Kivelson et al., 2009). This incoming plasma ionizes neutral particles in Europa's exosphere, mainly via electron impacts (Saur et al., 1998), generating an ionosphere around the moon (e.g., Bagenal & Dols, 2020). The injection of slow-moving ionospheric particles drains momentum from the upstream plasma, causing it to slow and accumulate above the moon's upstream hemisphere (e.g., Arnold, Liuzzo, & Simon, 2020; Harris et al., 2021; Rubin et al., 2015). The Jovian magnetic field lines pile up in this region, leading to an enhanced magnetic field magnitude above the moon's orbital trailing hemisphere (e.g., Saur et al., 1998). North and south of the moon, the magnetic field lines form a draping pattern, with a flow-aligned (south) and anti-flow aligned (north) component, respectively, which can attain values up to half that of the Jovian background field (e.g., Arnold, Liuzzo, & Simon, 2020; Rubin et al., 2015). At larger distances to the moon, the plasma interaction propagates electric currents to Jupiter's polar ionosphere through the formation of Alfvén wings (Neubauer, 1980, 1998; Simon et al., 2021).

The nature of Europa's interaction with the upstream plasma varies over a synodic rotation, since the plasma density decreases as the moon moves away from the center of the plasma sheet (e.g., Bagenal & Delamere, 2011). The time-variation of the background Jovian field and plasma interaction induces electric currents in Europa's conductive subsurface ocean, leading to the generation of an induced, quasi-dipolar magnetic field centered at the moon (e.g., Kivelson et al., 1999; Schilling et al., 2007; Vance et al., 2021; Zimmer et al., 2000). This induced field "twists" the field lines within the Alfvén wings, reduces the wings' cross-sections, and diminishes the electric currents along the wing characteristics (Neubauer, 1999).

In addition to the thermal plasma of the Jovian plasma sheet, Europa's surface is continually irradiated by energetic ions and electrons with energies ranging from ≈ 5 keV up to 10s of MeV. Energetic ions and electrons bounce back and forth along the Jovian magnetospheric field lines between Jupiter's polar regions and continually impinge upon Europa from the north and south. The energy distribution of these particles near Europa's orbit has been measured by both the Galileo Energetic Particle Detector (EPD) instrument (Mauk et al., 2004; Paranicas et al., 2000, 2001, 2002) and Juno JEDI instrument (Clark et al., 2020; Kim et al., 2020; Ma et al., 2021; Shen et al., 2022). The energetic ion population at Europa consists primarily of protons and singly/multiply charged oxygen and sulfur ions (Cooper et al., 2001; Kim et al., 2020; Paranicas et al., 2009). Within the energy range from 10 keV–1 MeV, Galileo EPD observations show that the ambient energetic electron flux near Europa is one to two orders of magnitude higher than the ion flux (Paranicas et al., 2009). The large energies of these particles allow most of them to pass through Europa's exosphere without colliding with the neutral gas, and implant into the surface (Lindsay & Stebbings, 2005; Plainaki et al., 2018).

Sputtering of water ice and its dissociation products (e.g., H_2 , O_2) via charged particle impacts is the main process by which Europa's dilute exosphere is generated (e.g., Johnson et al., 2009; Plainaki et al., 2018; Saur et al., 1998). Molecular and atomic hydrogen are too light to be bound by Europa's gravity, and rapidly escape into the neutral torus (Nénon & André, 2019; Roth et al., 2017; Smith et al., 2019). Sputtered H_2O efficiently refreezes to Europa's surface and is therefore rapidly removed from the exosphere on timescales of minutes (Eviatar et al., 1985; Smyth & Marconi, 2006). Nevertheless, a localized, persistent H_2O exosphere has recently been detected by HST above Europa's subsolar point, which at the time of observation was located in the moon's orbital trailing hemisphere (Roth, 2021). Evidence for this local H_2O exosphere was also found in Galileo magnetometer data from the E12 flyby (Cervantes & Saur, 2022). Neutral oxygen largely remains bound by Europa's gravity, and does not efficiently stick to the surface ice upon re-impacting (Eviatar et al., 1985), residing in the exosphere on timescales of tens of hours (Smyth & Marconi, 2006). As such, molecular oxygen dominates the total column density of Europa's exosphere, and is the main constituent of the moon's neutral gas envelope below approximately 300 km altitude (Plainaki et al., 2018; Roth et al., 2016; Vorburget & Wurzel, 2018).

While both ions and electrons can sputter material from ice (e.g., Johnson et al., 1982; Orlando & Sieger, 2003), ions have long been considered to be the primary sputtering agents at Europa (e.g., Johnson et al., 2009, and references therein). Cassidy et al. (2013) used particle-tracing simulations to calculate the spatial distribution of sputtering rates of H_2O and O_2 from both thermal and energetic H^+ , O^{2+} , and S^{3+} ions incident upon Europa's

surface. These authors found that energetic ions preferentially precipitate onto the moon's polar regions, while thermal ion impacts are confined to the upstream hemisphere. The ion sputtering rate was found to maximize near the moon's upstream apex, and to decrease with distance from this point. To calculate the trajectories of the incident magnetospheric ions, Cassidy et al. (2013) considered a single, averaged case of the dynamic magnetospheric conditions near Europa, with a uniformly southward magnetic field vector at all points. However, Galileo magnetometer measurements have shown that the interaction of the thermal plasma with Europa's ionosphere and induced dipole field substantially alters the electromagnetic field configuration near the moon, and hence, the forces acting on impinging energetic particles (e.g., Arnold et al., 2019; Arnold, Liuzzo, & Simon, 2020; Harris et al., 2021; Rubin et al., 2015). Since Europa's induced field arises mainly from the *non*-southward magnetic field components (e.g., Saur et al., 2010), it was also not included in the model setup of Cassidy et al. (2013).

In order to calculate the effect of Europa's perturbed electromagnetic environment on ion influx patterns onto the surface, Breer et al. (2019) and Addison et al. (2021) combined a hybrid model (kinetic ions, fluid electrons) of the draped electromagnetic fields with a particle-tracing code to calculate the trajectories of magnetospheric ions near the moon. They demonstrated that the inclusion of magnetic field pileup and draping substantially alters the pattern of ion influx onto the surface, compared to a setup that uses uniform fields. Addison et al. (2021) showed that field-line draping partially protects Europa's upstream hemisphere from thermal ion bombardment while simultaneously deflecting many of the upstream thermal ions onto the moon's low-latitude downstream hemisphere. This finding is in stark contrast to surface flux patterns calculated with uniform fields, where *no* thermal plasma can reach the mid-to-low latitude downstream hemisphere (Cassidy et al., 2013). Utilizing a multifluid MHD model, Harris et al. (2021) found a similar redistribution of the thermal ion flux onto Europa's downstream hemisphere.

The study of Addison et al. (2021) also revealed that the draping of the magnetic field lines causes many energetic ions to gyrate into Europa's surface closer to the poles than when the fields are uniform. This mechanism reduces the energetic ion influx onto the region near Europa's upstream apex by approximately 50% (Addison et al., 2021) compared to that calculated with uniform fields. Nordheim et al. (2022) independently confirmed this reduction of energetic ion flux near the upstream apex with particle-tracing simulations, using the same electromagnetic field configurations as Harris et al. (2021).

In a follow-up study, Addison et al. (2022) calculated the spatial distribution of ion sputtering rates of H₂O, O₂, and H₂ from Europa's surface. Their model revealed that the inclusion of field-line draping reduces the total sputtering rate of H₂O from Europa's surface by approximately 50% compared to uniform electromagnetic fields. These authors also found that only the O₂ sputtering rates calculated with perturbed electromagnetic fields reproduce observed O₂ column densities from HST. In addition, Addison et al. (2022) showed that, despite the deflection of a significant portion of the incident ion population onto the downstream hemisphere, the sputtering rate of H₂O with perturbed electromagnetic fields features a highly localized maximum near the moon's upstream apex. This is consistent with the localized H₂O exosphere observed by Roth (2021) in the same region.

A potentially significant contribution of electron impacts to energy deposition and surface modification at Europa has been hypothesized since the Galileo era (Cooper et al., 2001; Paranicas et al., 2001). The study of Cooper et al. (2001) estimated that electrons contribute 75% of the total energy deposited by particle impacts into the moon's surface. Electrons also penetrate more than 50 times deeper into Europa's icy surface than ions (e.g., Teolis et al., 2017; Ziegler & Manoyan, 1988), and as such are important agents in modifying the optical properties observed by telescopes and spacecraft, as well as in the destruction of potential biosignatures (Nordheim et al., 2018). Recent laboratory studies of electron sputtering yields from water ice (e.g., Galli et al., 2018; Meier & Loeffler, 2020) have enabled the first estimates of global sputtering rates across Europa's entire surface from magnetospheric electron impacts (Davis et al., 2021; Vorburger & Wurz, 2018). These studies assume that electron influx uniformly reaches every location on Europa's surface, and combine these fluxes with laboratory measurements of electron sputtering yields to calculate the global production rates. The results of Vorburger and Wurz (2018) and Davis et al. (2021) suggest that the O₂ production rate by electron sputtering may rival, or even exceed, that of ion sputtering. This idea would drastically alter the paradigm of exospheric generation at Europa being largely driven by ion impacts.

Modeling of electron bombardment at Europa requires the inclusion of their motion through the global Jovian magnetospheric field, as the electrons bounce between Europa's orbit and Jupiter's polar ionosphere sufficiently fast to initially miss the moon, but still impact after returning from a bounce (Paranicas et al., 2001, 2009).

For example, a 100 keV electron with a pitch angle of 45° requires approximately 7 s to leave Europa's local environment, bounce, and return (Paranicas et al., 2009), while it requires 30 s for the field line along which it travels to traverse Europa's disc (Paranicas et al., 2009). Such an electron would only be displaced $0.5 R_E$ during a bounce period, and its trajectory would intersect Europa's disc upon its return. In contrast, the vast majority of ions bounce too slowly to re-impact the moon or encounter its perturbed electromagnetic environment (Paranicas et al., 2009). Only the highest energy protons (≈ 10 MeV), which are sparse in the upstream distribution, can return less than $1 R_E$ downstream after a bounce, and therefore make multiple attempts to impact the moon (Nordheim et al., 2022).

Paranicas et al. (2001) combined energy spectra observed by the Galileo spacecraft with an analytical model to calculate the spatial distribution of 10 keV–10 MeV electron influx onto Europa's surface. Since the electron gyroradii at Europa are smaller than 10% of the moon's radius in this energy range, the approach of Paranicas et al. (2001) does not trace individual particles, but rather approximates their dynamics by considering the motion of the magnetospheric field lines along which their guiding centers travel. These authors reasoned that, since the bounce times of energetic electrons at Europa are significantly smaller than the time required for a Jovian magnetic field line to cross the moon in the azimuthal direction, a field line that comes into contact with the surface gradually depletes its population of energetic electrons as it moves across Europa's disc. Electrons at the lower edge of the studied energy range studied require more time to bounce, and therefore return farther downstream than higher-energy electrons. Thus, lower energy electrons can impact not only near the upstream equatorial region, but also at higher latitudes. Influx of higher energy (>1 MeV) electrons was found to be confined to a narrow region near the moon's upstream equator, since these particles bounce so quickly that their population is depleted by impacts at low latitudes. The resulting electron surface flux pattern in the model of Paranicas et al. (2001) therefore resembles a “lens” feature, with maximum flux at low latitudes on Europa's upstream hemisphere, and decreasing flux with greater distances from the equator. Paranicas et al. (2001) also suggested that, since electrons are displaced by less than $1 R_E$ toward downstream after a bounce, they cannot precipitate onto the downstream hemisphere. Their modeled electron energy deposition pattern was shown to be consistent with the distribution of sulfuric hydrate on Europa's upstream surface observed by Galileo. Therefore, Paranicas et al. (2001) concluded that energetic electrons are a principal agent of radiolytic surface chemistry on Europa. The model of Paranicas et al. (2001) was also applied in the studies of Patterson et al. (2012), Dalton et al. (2013), and Nordheim et al. (2018) to investigate various surface modification processes at Europa.

In addition, Dalton et al. (2013) implemented the particle-tracing model of Cassidy et al. (2013) to calculate the trajectories of energetic electrons near Europa, thereby including gyration effects not captured in the approach of Paranicas et al. (2001). Utilizing this tracing model, Dalton et al. (2013) showed that gyration prevents some electrons from reaching Europa's equator, as their gyromotion carries them into the surface before they can reach the low latitudes. This cuts out an equatorial “belt” (where the surface flux is reduced) from the lens-shaped pattern determined by Paranicas et al. (2001). The tracing model of Dalton et al. (2013) therefore found that the electron energy flux onto Europa's surface maximizes in two crescent-shaped regions near 30° northern or southern latitude, in contrast to the equatorial maximum derived from the model of Paranicas et al. (2001). The study of Dalton et al. (2013) combined their electron surface fluxes with the modeled ion surface flux maps from Cassidy et al. (2013) to search for correlations between charged particle bombardment patterns and observed non-uniformities in Europa's surface composition. They found that local enhancements of sulfuric acid surface concentration observed by Galileo correlate strongly with areas where both sulfur ion number influx and electron energy influx are high. Dalton et al. (2013) hypothesized that electron bombardment locally “heats” the surface, allowing magnetospheric sulfur ions to implant more deeply and create the observed sulfuric acid patterns. The studies of Paranicas et al. (2001), Patterson et al. (2012), Dalton et al. (2013), and Nordheim et al. (2018) all considered electron dynamics in spatially and temporally uniform electromagnetic fields near Europa, that is, without the inclusion of the moon's induced field or plasma interaction effects.

Truscott et al. (2011) modeled energetic electron trajectories and irradiation of Europa's surface while including the moon's induced field for the conditions of the Galileo E4 flyby, though these authors did not draw conclusions on the influence of the induced field on their electron surface flux patterns. Similar to Paranicas et al. (2001), the study of Truscott et al. (2011) found that the electron flux onto the surface is concentrated in a lens-like pattern on the moon's low latitude upstream hemisphere. However, they found that the influx patterns are deformed compared to a scenario that does not include the induced dipole.

Magnetic field line draping has already been found to play a critical role in determining ion precipitation patterns at Europa (Addison et al., 2021, 2022; Breer et al., 2019; Harris et al., 2021; Nordheim et al., 2022). Preceding studies by Liuzzo et al. (2019a, 2022) also revealed that electron precipitation patterns onto Callisto are substantially affected by the moon's plasma interaction. Specifically, Liuzzo et al. (2019a) showed that magnetic field line draping and the induced dipole field are capable of protecting entire regions of the Callisto's surface from electron bombardment. In a follow-up study, Liuzzo et al. (2022) systematically examined electron influx patterns at Callisto over the course of a synodic rotation. They found that the stretching of the moon's magnetic pileup region into the anti-Jovian hemisphere (due to large pickup ion gyroradii) partially deflects impinging electrons away from this region when Callisto is embedded in the Jovian plasma sheet. Liuzzo et al. (2022) also showed that electrons which have already drifted several moon radii downstream of Callisto can be channeled by the draped field lines back toward upstream and into the moon's downstream hemisphere. Such electrons would not be able to impact the moon when the fields are treated as uniform, stressing the need to include a realistic field configuration when modeling electron irradiation patterns of the Galilean satellites. Since the gyroradii of energetic electrons at Europa are typically much smaller than 10% of the moon's radius, the locations where they precipitate onto the surface are largely determined by the shape of the magnetic field lines. Therefore, even subtle alterations to the local magnetic field line geometry may drastically influence where electrons impact the surface.

To constrain the role of the electromagnetic field perturbations in modifying electron surface flux patterns at Europa, we use the three-dimensional AIKEF hybrid model (Müller et al., 2011) to calculate the structure of the draped field lines near the moon. We then compute maps of the energetic electron surface fluxes at several distinct points during a Jovian synodic rotation using a modified version of the GENTOO particle tracing tool (e.g., Addison et al., 2021, 2022; Liuzzo et al., 2019b; Liuzzo et al., 2022), while incorporating the latest Juno-era models of Jupiter's global magnetospheric field to determine electron bounce motion. Finally, we calculate maps of the sputtering rates of O₂ from the moon's surface using empirical models of electron sputtering yields from the literature (Davis et al., 2021; Teolis et al., 2017; Vorburger & Wurz, 2018). By averaging over a full synodic period we then constrain the average surface erosion patterns associated with electron bombardment over geologic timescales. Combination of our results with those obtained by Addison et al. (2021, 2022) for magnetospheric ion precipitation allows us to determine the relative contributions of energetic ions and electrons to exosphere generation and surface modification at Europa.

The paper is structured as follows. In Section 2 we describe the AIKEF hybrid code simulations, the GENTOO particle-tracing tool, our implementation of Jupiter's global magnetospheric field, and our treatment of the electron sputtering yields. In Section 3.1 we present AIKEF model results for the perturbed electromagnetic fields near Europa at four different system III longitudes of the moon. In Section 3.2 we present maps of the differential electron surface flux as a function of electron energy at each system III longitude. Maps of the electron number flux, energy flux, and O₂ sputtering rates, integrated across the entire energy range considered, are presented in Section 3.3. Also presented in Section 3.3 are the total precipitation rates, power deposition, and O₂ production rate integrated across Europa's surface. Section 3.4 presents the energetic electron number flux, energy flux, and sputtering rates averaged across a full synodic rotation. Also presented in Section 3.4 is a comparison to the influxes and sputtering rates of magnetospheric ions, obtained from our previous studies (Addison et al., 2021, 2022). Finally, in Section 3.5, we briefly constrain the robustness of results by investigating the role of the pitch angle distribution in shaping energetic electron influx onto Europa. Our major findings are summarized in Section 4. Additional results that support our conclusions are included in Appendices A, B, and C.

2. Modeling Energetic Electron Influx Onto Europa

2.1. Modeling of Europa's Perturbed Electromagnetic Environment

In order to calculate the three-dimensional electromagnetic field structure near Europa, we employ the AIKEF hybrid plasma simulation code (Müller et al., 2011). AIKEF models the interaction between Europa and the upstream, thermal magnetospheric plasma. The hybrid approach allows for a complete description of the full thermal ion velocity distribution, which contains particles with velocity vectors that depart substantially from the corotation direction. Addison et al. (2021) showed that ions whose velocities are significantly inclined against the corotation direction may contribute significantly to thermal ion influx onto Europa's downstream hemisphere. AIKEF has been extensively applied to analyze the plasma environments of the Galilean moons, including six studies of plasma dynamics at Europa (Addison et al., 2021, 2022; Arnold et al., 2019; Arnold, Liuzzo, &

Table 1
Simulation Parameters for the AIKEF Model

Position w.r.t mag. equator	Center (southward sweep)	Center (northward sweep)	Max. above	Max. below
λ_{III}	110°	284°	191°	26°
\mathbf{B}_0 [nT]	(82, 0, -401)	(-63, 0, -376)	(-3, -224, -403)	(4, 209, -385)
B_0 [nT]	409	381	461	438
\mathbf{M}_{ind} [$\times 10^{27}$ J/nT]	(-1.56, 0, 0)	(1.20, 0, 0)	(0.006, 4.26, 0)	(-0.008, -3.97, 0)
n_0 [cm ⁻³]	200	200	40	40
\mathbf{u}_0 [km/s]	(100, 0, 0)	(100, 0, 0)	(100, 0, 0)	(100, 0, 0)
\mathbf{E}_0 [mV/m] ^a	(0, -40.1, 0)	(0, -37.6, 0)	(0, -40.3, 22.4)	(0, -38.5, -20.9)
$k_B T_0$ [eV]	100	100	100	100
$V_{A,0}$ [km/s] ^b	147	136	370	351
$M_{A,0}$ ^c	0.68	0.73	0.27	0.28

Note. The background magnetic field vectors were calculated with the Jovian magnetospheric field models of Connerney et al. (2020); Connerney et al. (2022).

^aConvective Electric Field $\mathbf{E}_0 = -\mathbf{u}_0 \times \mathbf{B}_0$. ^bAlfvén Speed $V_{A,0} = \frac{|\mathbf{B}_0|}{\sqrt{\mu_0 m_0 n_0}}$. ^cAlfvénic Mach Number $M_{A,0} = \frac{|\mathbf{u}_0|}{V_{A,0}}$.

Simon, 2020; Arnold, Simon, & Liuzzo, 2020; Breer et al., 2019), and seven investigations at Callisto (Liuzzo et al., 2015, 2016, 2017, 2018, 2019a, 2019b, 2022). The study of Arnold et al. (2019) found excellent quantitative agreement between AIKEF output and magnetometer data from the Galileo E26 flyby of Europa, even reproducing fine-scale signatures in the observed field components associated with a local water vapor plume. The setup of AIKEF at Europa has been described extensively in our previous publications, and we therefore present only a brief summary of the major input parameters here. Compared to our previous studies (Addison et al., 2021, 2022), the input parameters for the model have been updated using the latest Juno-era magnetospheric field models.

We use the Cartesian, moon-centered EPhiO system to describe Europa's interaction with Jupiter's corotating plasma. In this system, the x axis points along the direction of corotation, the z axis is parallel to Jupiter's rotation axis, and the y axis completes the right-handed system, pointing toward Jupiter. The unit basis vectors in this system are denoted \hat{x} , \hat{y} , and \hat{z} . Similar to Addison et al. (2021, 2022), we treat the upstream thermal plasma as consisting of thermal electrons and a composite, singly-charged ion species with mass $m_0 = 18.5$ amu (e.g., Kivelson et al., 2009). The temperature of both the thermal ions and electrons is set to $k_B T_0 = 100$ eV, based upon Galileo observations (Bagenal et al., 2015; Kivelson et al., 2009). The bulk velocity of the upstream plasma is set to $\mathbf{u}_0 = (100, 0, 0)$ km/s. In agreement with Galileo observations (Bagenal et al., 2016), we do not include any components of the upstream flow velocity away from the (+ x) direction. The AIKEF domain in our simulations encompasses the cuboid defined by $-9 R_E \leq x \leq 21 R_E$, $-10 R_E \leq y \leq 10 R_E$, and $-30 R_E \leq z \leq 30 R_E$. We use two levels of grid refinement centered at Europa in order to achieve sufficiently high resolution near the moon. The size of a grid cell in our simulations is $0.02 R_E$ for $|x|, |y|, |z| \leq 1.5 R_E$, then $0.04 R_E$ for $1.5 R_E < |x|, |y|, |z| \leq 3 R_E$, and $0.08 R_E$ for $|x|, |y|, |z| > 3 R_E$. The highest level of refinement allows for the resolution of Europa's O₂ exosphere, which has a scale height on the order of $0.06 R_E$ (Plainaki et al., 2018).

To systematically investigate electron precipitation onto Europa, we apply AIKEF to calculate the electromagnetic field configuration at four distinct locations of the moon relative to the Jovian magnetic equator (i.e., four different Jovian System III west longitudes λ_{III}), distributed (approximately) equally in time over the course of a synodic rotation. The ambient magnetospheric field vector \mathbf{B}_0 is determined using the JRM33 internal magnetic field model of Connerney et al. (2022) and the magnetodisc field model of Connerney et al. (2020). These two models take into account the latest data from the Juno spacecraft, and are in excellent agreement with magnetometer observations in the inner-to-middle magnetosphere. System III longitudes, ambient magnetospheric field vectors, and plasma parameters for each of the four cases examined in this study are given in Table 1. The magnetic field lines which intersect Europa's center at each of the four locations studied here, calculated with the models of Connerney et al. (2020, 2022), are displayed in Figure 1. The illustration utilizes a left-handed

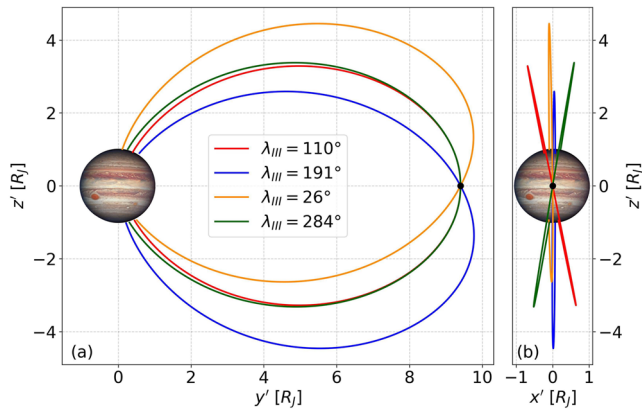


Figure 1. Jovian magnetospheric field lines which intersect the center of Europa at the four system III longitudes given in Table 1, calculated with the internal field model of Connerney et al. (2022) and the magnetodisc model of Connerney et al. (2020). The plot is given in a left-handed, Jupiter-centered coordinate system, with the x' and z' axes parallel to the respective x and z axis in the EPhiO system, and the y' axis pointing from Jupiter's center to Europa's center (i.e., antiparallel to the EPhiO y axis). Panel (a) displays the magnetic field lines projected into the plane perpendicular to Europa's orbital direction and containing the moon's center, while panel (b) displays the field lines projected into the plane containing Europa's orbital velocity vector (in the $+x'$ direction), the z' (south-north) axis, and the moon's center. Europa is denoted with a black dot, and is not to scale.

coordinate system with its origin at Jupiter's center, with the x' axis parallel to the EPhiO x axis, the y' axis antiparallel to the y axis, and the z' axis parallel to the z axis.

We model Europa's electromagnetic environment at the two points in time when the moon crosses the planetary magnetic equator, both when the equator sweeps *southward* over the moon (system III west longitude $\lambda_{III} = 110^\circ$, red field line in Figure 1) and when it sweeps *northward* over the moon ($\lambda_{III} = 284^\circ$, green field line). In both of these cases, the $B_{0,y}$ component of the ambient magnetospheric field (i.e., the component along the Europa-Jupiter line) is zero (Figure 1a). However, the tilt of the Jovian magnetic moment with respect to Europa's orbital plane entails that the moon experiences a field component parallel/antiparallel to the corotation direction (i.e., $\pm \hat{x}$) when it crosses the magnetic equator (Figure 1b). This azimuthal component is at most 20% of the total field strength $|\mathbf{B}_0| = B_0$ (e.g., Connerney et al., 2020, 2022; Kivelson et al., 1999; Schilling et al., 2007). Since the x direction of the EPhiO system changes along Europa's orbit, the sign of this $B_{0,x}$ component depends upon whether the magnetic equatorial plane sweeps over the moon from north to south or from south to north. When the magnetic equator passes southward over the moon, the $B_{0,x}$ component of the ambient field is positive, and vice versa (see, e.g., Figure 1 of Kivelson et al., 1999). As such, it is necessary to investigate *two* distinct configurations of the ambient magnetospheric field when Europa is located at the magnetic equator. We note that in our previous study of ion irradiation at Europa (Addison et al., 2021), the two magnetic equator cases were represented by only a single AIKEF scenario.

In addition, we calculate the structure of Europa's electromagnetic environment when the moon is located at maximum elongation above ($\lambda_{III} = 191^\circ$, blue field line in Figure 1) or below ($\lambda_{III} = 26^\circ$, orange field line) the magnetic equator. At these positions, Europa is connected to planetary magnetic field lines that are further stretched outwards by the magnetodisc field, and therefore have strong radial ($B_{0,y}$ in the EPhiO system) components. When the moon is located above the Jovian magnetic equator (blue field line in Figure 1), the ambient magnetospheric field points away from the planet, and $B_{0,y}$ is therefore negative. Below the magnetic equator, the magnetic field vector points toward the planet, and $B_{0,y}$ is positive (Figure 1a, orange field line). The strength of these radial field components reaches approximately 50% of the total field magnitude (Connerney et al., 2022; Kivelson et al., 1999; Schilling et al., 2007). Since the magnetic moment of Jupiter is perpendicular to the corotation direction at these two orbital positions, the $B_{0,x}$ component of the ambient field at Europa is nearly zero (see Figure 1b and, e.g., Kivelson et al., 1999; Schilling et al., 2007). The southward component of the background field $B_{0,z}$ remains largely constant over the course of a synodic rotation, not varying by more than ≈ 25 nT, or 5% of B_0 (Connerney et al., 2020, 2022; Kivelson et al., 1999). Juno magnetometer data revealed a non-negligible north-south hemispheric dichotomy in the Jovian internal magnetic field, with the non-dipolar field moments largely confined to the northern hemisphere (Connerney et al., 2020; Moore et al., 2018). This dichotomy is likely due to non-uniformities in the convective, dynamo layer within the planet. The magnetic field magnitudes above and below the magnetic equator in our model are therefore not equal (Table 1).

Using the Jovian magnetospheric field vectors calculated at each of the four system III longitudes, we determine Europa's induced magnetic moment \mathbf{M}_{ind} using Equation 2 from Addison et al. (2021). This equation treats Europa as a perfectly conducting sphere, that is, the inductive response has an amplitude of one (normalized to the response of a perfect conductor) and a phase lag of zero relative to the inducing field. Analysis of Galileo magnetometer data from the Europa flybys by Zimmer et al. (2000) showed that the inductive response of a perfect conductor is consistent with the observed magnetic field within the uncertainties introduced by the plasma interaction and the limited coverage of Europa's interaction region provided by Galileo. A recent study by Vance et al. (2021) considered depth-dependent electrical conductivity profiles of Europa's subsurface ocean to model the moon's inductive response. These authors found that, depending on the interior model used, the (normalized) amplitude of the inductive response may be as low as 0.85, and the phase delay between the induced and inducing field may be as high as 15° . The assumption of a perfectly conducting sphere therefore provides an upper limit

on the role that the induced field may play in modifying electron influx at Europa. The uncertainties introduced by varying treatments of Europa's inductive response are small (e.g., amplitude of 0.85 vs. 1) compared to the those introduced by, for example, varying estimations of the plasma density at Europa (factor of 4, e.g., Bagenal & Delamere, 2011; Roth et al., 2014).

The induced magnetic moment vectors for all four system III longitudes examined in this study are given in Table 1. The oscillation of the $B_{0,x}$ and $B_{0,y}$ components of the background Jovian field over the course of a synodic rotation leads to varying orientation and strengths of Europa's induced dipole field. When the moon is located at the magnetic equator, the induced magnetic moment is oriented parallel or antiparallel to the x axis, and the magnitude of the induced field is roughly 20% of the background field magnitude. At maximum elongation above or below the magnetic equator, the induced magnetic moment is oriented along the $\pm y$ axis, and the induced magnetic field attains strengths of approximately half of the background magnetic field magnitude.

The number density of the upstream thermal plasma n_0 at Europa slowly varies over the course of a synodic rotation as the center of the magnetospheric plasma sheet sweeps above and below the moon. The density approximately depends on the distance to the center of the plasma sheet h_{ps} according to a Gaussian profile $n_0 = n_{p,0} \exp[-(h_{ps}/H)^2]$, where $n_{p,0}$ is the density at the center of the sheet, and H is a scale height (Bagenal & Delamere, 2011; Hill & Michel, 1976). The number density is therefore maximized at the center of the plasma sheet ($\lambda_{III} = 110^\circ, 284^\circ$) where $h_{ps} = 0$, and minimized at maximum elongation ($\lambda_{III} = 26^\circ, 191^\circ$). Analysis of Galileo Plasma Subsystem (PLS) and Plasma Wave Subsystem (PWS) data by several authors has produced different estimates of the values of $n_{p,0}$ and H at Europa (e.g., Bagenal & Delamere, 2011; Roth et al., 2014). In order to facilitate comparison to the energetic ion influx maps calculated by Addison et al. (2021, 2022), we adopt the same values used in our two preceding studies: $n_{p,0} = 200 \text{ cm}^{-3}$ and $H = 0.9R_J$. These parameters were obtained from a Gaussian fit to Galileo PWS data from the targeted Europa flybys (Roth et al., 2014). At maximum elongation, Europa deviates by approximately 9.6° in latitude from the magnetic equator, but only by about 7° from the centrifugal equator, where the center of the plasma sheet is located (Khurana, 1997; Kivelson et al., 2009; Phipps & Bagenal, 2021). At the maximum distance between Europa and the center of the plasma sheet, we then find an upstream density of $n_0 \approx 40 \text{ cm}^{-3}$. The plasma sheet structure along Europa's orbit is not affected by local time (Bagenal & Delamere, 2011; Bagenal et al., 2016).

The AIKEF model treats Europa's exosphere as consisting entirely of O_2 (e.g., Plainaki et al., 2018), and ionizes the exosphere purely through electron impacts, which have been shown to be the dominant ionization mechanism (Saur et al., 1998). The neutral density profile in our model is the same as used in all six of our preceding studies of Europa (Addison et al., 2021, 2022; Arnold et al., 2019; Breer et al., 2019; Arnold, Liuzzo, & Simon, 2020; Arnold, Simon, & Liuzzo, 2020). In the moon's downstream hemisphere ($x > 0$), the neutral density in our model depends only on altitude, and follows a barometric profile. Above the upstream hemisphere ($x < 0$), the exosphere in our model features a "bulge" centered at the $x = -1 R_E$ apex, that is, the density is maximized above the upstream apex and decreases with angular distance from it, transitioning smoothly into the downstream profile in the $x = 0$ plane (see, e.g., Equation 4 of Addison et al., 2021). In agreement with HST observations, we use a scale height of 100 km for the entire exosphere (Roth et al., 2016). The surface density of the O_2 gas in the downstream hemisphere is set to a constant value of $5 \times 10^{13} \text{ m}^{-3}$, consistent with HST measurements of the O_2 column density (Hall et al., 1995; Roth et al., 2016). In the upstream hemisphere, the surface density decreases with distance from the upstream apex. The exospheric surface density at the upstream apex is eleven times greater than in the downstream hemisphere, that is, $5.5 \times 10^{14} \text{ m}^{-3}$. This exospheric configuration was found by Arnold et al. (2019) to most accurately reproduce magnetometer data from the Galileo E26 flyby. Harris et al. (2022) investigated the role of different exospheric surface densities and scale heights on Europa's plasma interaction, varying the surface density at the upstream apex from $5 \times 10^{13} \text{ m}^{-3}$ to $1.5 \times 10^{14} \text{ m}^{-3}$, and the scale height from 33 to 330 km. They found that only scale heights and surface densities that drastically depart from those observed by HST can substantially alter which magnetic field lines are in contact with the moon.

Using an MHD model, Cervantes and Saur (2022) recently investigated the influence of an additional H_2O exosphere above Europa's upstream apex, as identified by Roth (2021), on the local electromagnetic field structure during the Galileo E12 flyby. By including such a localized H_2O exosphere they were able to explain several fine structures in the magnetometer data from this flyby which could not be reproduced with their radially symmetric, barometric O_2 exosphere (see Figure 10 from that paper). However, these authors used a more dilute O_2 exosphere than is included in our study, with a column density above the upstream apex that is approximately

an order of magnitude lower than considered here. The combination of their O₂ and H₂O exospheres yields a column density above the upstream apex of approximately $3.2 \times 10^{19} \text{ m}^{-2}$, only slightly lower than the value used in our study for O₂ alone ($5.5 \times 10^{19} \text{ m}^{-2}$). Laboratory data on electron impact ionization frequencies of H₂O is not available in the peer-reviewed literature. Therefore, Cervantes and Saur (2022) utilized the same electron impact ionization frequencies for H₂O as for O₂, similar to Arnold et al. (2019). Recent theoretical estimates of the electron impact ionization rates with H₂O have shown that the ionization rates are indeed similar to those for O₂ at Europa (Carberry Mogan et al., 2023). Taking into account this similarity in the cross-sections and the masses of the two pickup species, the “bulged” O₂ profile used in our study would produce similar plasma interaction signatures as the combination of an O₂ and H₂O exosphere employed by Cervantes and Saur (2022). Furthermore, the generation mechanism and dynamics of the localized H₂O exosphere observed by HST are not well understood. At the time of its detection by Roth (2021), Europa's upstream apex (i.e., the sub-plasma point) and subsolar point were collocated. As such, these authors could not discern whether the H₂O density enhancement follows the subsolar point, as it would be if it were driven by sublimation, or whether it is persistently located near the upstream apex, as it would be if it were generated via ion sputtering (Addison et al., 2022). During the E12 Galileo flyby, Europa's subsolar and sub-plasma points were indeed co-located. Therefore, the study of Cervantes and Saur (2022) could not provide any additional insights into the local time dependence of the H₂O exospheric density bulge. In other words, it is currently not feasible to include the proper location of such an H₂O density enhancement as we model Europa's plasma interaction over the course of a synodic rotation. For these two reasons, we do not include an H₂O component to Europa's exosphere when calculating the electromagnetic field perturbations with AIKEF.

2.2. Tracing of Energetic Electrons

In order to calculate the precipitation patterns of energetic magnetospheric electrons onto Europa's surface, we use a modified version of the GENTOO particle tracing code (Liuzzo et al., 2019b, 2020, 2022), which has been employed in three of our previous studies to model ion dynamics near this moon (Addison et al., 2021, 2022; Breer et al., 2019). GENTOO is a backtracing model, meaning that particles of a given energy are initialized on Europa's surface and then traced backwards in time. Particles which re-impact the moon at some point in time after initialization do not possess valid trajectories and are deleted from the simulation. In forward time, these particles would have to travel through the solid body of Europa in order to reach their “launch point” on the surface. Backtraced particles which do not re-impact the moon's surface, but escape into the ambient magnetospheric environment, possess “allowed” trajectories. In a forward-tracing picture, these particles originate outside of Europa's perturbed local environment, precipitate onto the moon, and contribute to surface bombardment. GENTOO treats the energetic electrons as test particles, that is, particles which move through the prescribed electromagnetic fields calculated with AIKEF, since these particles are too dilute to significantly contribute to the field perturbations near Europa (e.g., Cooper et al., 2001).

We initialize backtraced energetic electrons across Europa's surface on a grid which is equally spaced in both latitude and longitude. We use a longitude step of $\Delta\phi = 2^\circ$ and latitude step of $\Delta\theta = 2^\circ$, yielding $90 \times 180 = 16,200$ grid nodes across the moon's surface. At each grid node, electrons are launched with velocity vectors covering a half-sphere in velocity space, with the symmetry axis of the half-sphere given by the local surface normal vector. Each half-sphere in velocity space is also discretized equally in latitude and longitude, with longitude step $\Delta\phi_v = 5^\circ$ and latitude step $\Delta\theta_v = 5^\circ$ (where ϕ_v and θ_v are the longitude and latitude angles defined against the surface normal), yielding 1296 particles launched on each node of the spatial grid. Once an electron is launched from the surface, its equation of motion is solved using an adaptive, *negative* time step that is equal to 1/75 of the *local* gyroperiod in the perturbed magnetic field to which the electron is exposed. Each GENTOO simulation considers electrons of a single energy at Europa's surface. For each field configuration calculated with AIKEF, eight individual GENTOO runs are carried out: electrons are initialized at the grid points on Europa's surface with kinetic energies of $E = 5 \text{ keV}, 10 \text{ keV}, 50 \text{ keV}, 100 \text{ keV}, 500 \text{ keV}, 1 \text{ MeV}, 5 \text{ MeV},$ and 10 MeV , thereby encompassing the energy range where significant energetic electron fluxes have been observed near Europa's orbit (Mauk et al., 2004; Paranicas et al., 2001, 2009). These starting energies for energetic electrons match those used by Addison et al. (2021, 2022) for energetic ions, facilitating comparison between our electron results and the ion influx patterns calculated by those studies. We do not apply GENTOO to calculate the influx patterns of the thermal electron population onto Europa's surface. In contrast to energetic ions and electrons, thermal electrons do not pass through Europa's neutral envelope without strongly interacting with exospheric particles. Rather, thermal

electrons impacts are the dominant ionization mechanism for Europa's exosphere (Saur et al., 1998), as the electron-impact ionization cross-sections fall sharply at energies above the thermal regime (Hwang et al., 1996; Kanik et al., 1993). Including these effects in the numerical modeling framework would require a conceptually different approach and is beyond the scope of the present study. However, we do constrain the robustness of our results by providing analytical estimations on the contributions of thermal electrons to surface irradiation.

Considering the magnetic field vectors given in Table 1, the electron gyroradii in the energy range from 5 keV to 10 MeV vary from 0.04% to 5.34% of Europa's radius at pitch angles of 90°. At the lower end of the energy spectrum, electron dynamics therefore occur at scales which are smaller than the AIKEF grid size. Within an AIKEF grid cell, GENTOO uses trilinear interpolation to determine the electromagnetic field vector at the electron's location from the vectors at the eight adjacent AIKEF grid nodes. Such an approach is accurate to first order (Matsumoto & Omura, 1985), so non-linearities in the electromagnetic fields on the scales of electron gyration are not resolved. However, the perturbed electromagnetic fields at Europa change on scales of multiple AIKEF grid cells (e.g., Arnold et al., 2019; Arnold, Liuzzo, & Simon, 2020). Thus, relevant physics of Europa's electromagnetic interaction is *not* truncated by this approach.

Unlike ions, electrons experience substantial relativistic mass growth in the energy range from 5 keV (Lorentz factor $\gamma = \frac{E}{m_e c^2} + 1 = 1.01$, where m_e is the rest mass of the electron and c is the speed of light) to 10 MeV ($\gamma = 20.6$). As such, it is necessary to solve the relativistic equation of motion for each electron

$$m_e \frac{d(\gamma \mathbf{v})}{dt} = -e(\mathbf{E} + \mathbf{v} \times \mathbf{B}), \quad (1)$$

where \mathbf{v} is the velocity vector of the electron, e is the elementary charge, and \mathbf{B} and \mathbf{E} are the local magnetic and electric field vectors imported from AIKEF, respectively. To solve Equation 1, we apply the numerical method of Vay (2008), which is based upon the leapfrog algorithm and is of second-order accuracy. This method has been applied in previous GENTOO simulations to calculate relativistic electron dynamics at Callisto (Liuzzo et al., 2019a, 2022) and Ganymede (Liuzzo et al., 2020).

Computation of the electron bounce motion between Europa's interaction region and the electrons' mirror points near Jupiter's polar ionosphere requires coupling of Europa's local interaction region with a global model of the Jovian magnetospheric field (e.g., from Connerney et al., 2020, 2022). We set the boundaries of the GENTOO domain at $x = -6 R_E$ (upstream), $x = 12 R_E$ (downstream), $y = -10 R_E$ (anti-Jovian), $y = 10 R_E$ (sub-Jovian), $z = -10 R_E$ (south), and $z = 10 R_E$ (north), which is slightly smaller than the AIKEF box. At these distances, the perturbations to the Jovian magnetospheric field introduced by Europa are negligible, except for within the two highly-localized Alfvén wings (e.g., Addison et al., 2021; Arnold, Liuzzo, & Simon, 2020). The GENTOO domain is extended farther toward downstream than toward upstream, since the electromagnetic field perturbations extend as much as $10 R_E$ downstream, but are limited to within $\approx 5 R_E$ upstream (e.g., Arnold, Liuzzo, & Simon, 2020; Rubin et al., 2015). During the completion of a bounce period between Europa and their mirror points, energetic electrons drift in the azimuthal direction due to corotation, as well as gradient/curvature drifts. Since the drift motion of electrons below ≈ 20 – 25 MeV is toward downstream in a forward-tracing picture (Nordheim et al., 2018; Truscott et al., 2011), particles below 20 – 25 MeV drift toward upstream in a backtracing code such as GENTOO. Backtraced electrons which have not hit Europa's surface finally exit the moon's interaction region after they have drifted sufficiently far upstream that they cannot return and collide with the surface. Thus, we consider electrons to have “allowed” trajectories when they have traveled beyond the upstream face of the GENTOO simulation domain (i.e., $x = -6 R_E$). Such electrons are sufficiently far upstream that neither the field perturbations nor their diminutive gyroradii can carry them back toward Europa and into the moon's surface.

For electrons with energies above ≈ 20 – 25 MeV, the (retrograde, i.e., toward $-\hat{\mathbf{x}}$ in the forward-tracing picture) drift motion due to magnetic gradients and curvature exceeds the (prograde, i.e., $+\hat{\mathbf{x}}$) drift due to corotation (e.g., Nordheim et al., 2018; Truscott et al., 2011). Therefore, these electrons experience a net drift in the $-\hat{\mathbf{x}}$ direction, that is, toward upstream in the *forward-tracing* picture. Such electrons therefore precipitate mainly onto Europa's downstream hemisphere (e.g., Nordheim et al., 2018; Truscott et al., 2011). In the backtracing picture, electrons with allowed trajectories at these energies would exit the simulation domain out of the downstream face at $x = 12 R_E$. However, for our study of integrated electron influxes and sputtering rates, we do not simulate electrons with energies beyond 10 MeV, since the ambient magnetospheric fluxes above this energy are more than seven orders of magnitude lower than those at 10 keV (Paranicas et al., 2009). Furthermore, electron sputtering yields from the

literature either fall (Teolis et al., 2017) or remain constant (Vorburger & Wurz, 2018) at energies above several hundred eV. Thus, electrons at energies above 10 MeV make a vanishingly small contribution to surface influx and resultant sputtering rates and do not need to be considered within the scope of our study. However, we note that, since these high-energy electrons penetrate more deeply into the surface than any other magnetospheric particle population (e.g., Teolis et al., 2017; Ziegler & Manoyan, 1988), they may be important agents of surface processing at depth, as well as the potential destruction of biosignatures embedded within the surface (Nordheim et al., 2018). The model of Guio et al. (2020) suggests a slightly lower energy threshold than Truscott et al. (2011) and Nordheim et al. (2018) for the reversal in electron drift direction, namely 15.5–19.5 MeV versus 20–25 MeV. However, these values are still above the energy range ($E \leq 10$ MeV) investigated in this study. These slight deviations in the reversal energy may stem from different treatments of the Jovian magnetospheric field by the various authors. A reduction in the reversal energy would imply slightly smaller azimuthal displacements of bouncing electrons at all energies we consider. However, this effect would merely shift the features in our electron precipitation maps toward upstream, but would not alter their morphology.

If a backtraced electron leaves the GENTOO simulation domain, but does not yet meet the criterion for an allowed trajectory (i.e., it exits out of either the $y = -10 R_E$, $y = 10 R_E$, $z = -10 R_E$, or $z = 10 R_E$ boundaries of the domain), we consider the electron to be on its way to completing a bounce between Europa and the electron's mirror point. For such a bouncing electron, we calculate the azimuthal displacement r_{az} , that is, the distance in the x direction by which the electron is displaced during a half-bounce period. To determine r_{az} , we proceed analogous to Regoli et al. (2016) and Liuzzo et al. (2019a); Liuzzo et al. (2020, 2022) and employ the approach of Roederer (1967). This method uses the pitch angle of a bouncing electron when it exits Europa's interaction region to compute the distance the particle travels between the moon and its mirror point. By combining this information with the electron's energy, the half-bounce period $\tau_b/2$ is determined (i.e., the time required for the electron to leave Europa's interaction region, travel to its mirror point, and return to the moon) is determined. Combining the half-bounce period with the average azimuthal drift velocity of the electron during its half-bounce allows for the calculation of r_{az} (Roederer, 1967). An electron's azimuthal displacement depends upon its energy as well as its pitch angle at the point where it exits the GENTOO domain. More details on this approach are given in section 2.3.1 and equations 5–9 of Liuzzo et al. (2019a). For the calculation of electrons' azimuthal displacements, we again combine the Jovian internal magnetic field model of Connerney et al. (2022) with the magnetodisc model of Connerney et al. (2020). Since the ambient magnetic field vector within the AIKEF domain and just outside of the simulation domain are both provided by the models of Connerney et al. (2020, 2022), the magnetic field lines are continuous across the boundary. The only exceptions are two highly localized regions within the Alfvén wing tubes. The somewhat lower plasma velocity within the wing tubes may cause bouncing electrons (in the forward-tracing picture) to return farther upstream than they would without plasma effects, thereby shifting our calculated electron precipitation maps toward the upstream apex. However, inclusion of this effect is not feasible: there is no analytical approach (analogous to Neubauer, 1980, 1998) available that describes the propagation of the Alfvén wings toward Jupiter along the field lines of the Connerney et al. (2020, 2022) model. We do not take into account the small drift velocity that an electron would acquire due to gradient and curvature of the ambient magnetospheric field lines inside the AIKEF domain. Such drift motion would mainly affect the trajectories of electrons with pitch angles near 90° which constitute only a small fraction of the ambient electron population near Europa. Including such a drift would be inconsistent with the setup of AIKEF which inherently treats the ambient fields near Europa as uniform (e.g., Müller et al., 2011).

Figure 2 displays the electron azimuthal displacements calculated at $\lambda_{III} = 110^\circ$ (at the magnetic equator, Figure 2a and red field line in Figure 1) and $\lambda_{III} = 191^\circ$ (maximum distance above the magnetic equator, Figure 2b and blue field line in Figure 1) for several different pitch angles α_0 of electrons as they leave Europa's interaction region. Dashed lines indicate electrons which bounce in Jupiter's northern hemisphere ($\alpha_0 > 90^\circ$), while solid lines indicate electrons which bounce in Jupiter's southern hemisphere ($\alpha_0 < 90^\circ$). The azimuthal displacements of electrons with the same velocity perpendicular to the magnetic field, but opposite velocities along the magnetic field, are shown in the same color. The azimuthal displacements for electrons with energies from 1 keV–10 MeV monotonically decrease with increasing energy. When Europa is located at the magnetic equator (Figure 2a), the displacements are nearly symmetric (i.e., solid and dashed lines of the same color nearly overlap) between electrons which bounce in the southern hemisphere of Jupiter ($\alpha_0 < 90^\circ$; solid lines) and electrons which bounce in the northern hemisphere ($\alpha_0 > 90^\circ$; dashed lines). At this point the moon approximately bisects the Jovian field lines between the north and the south (red and green lines in Figure 1). When Europa is located at the magnetic

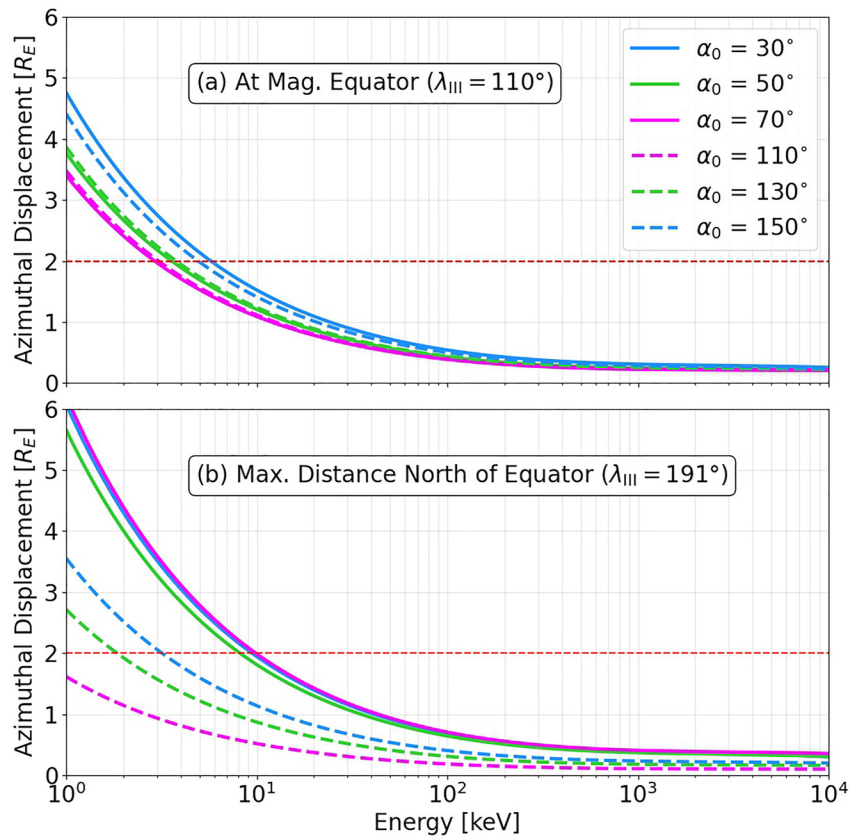


Figure 2. Azimuthal displacements for electrons with energies from 1 keV to 10 MeV, calculated with the model of Roederer (1967) for the *forward-tracing picture* at $\lambda_{III} = 110^\circ$ (Europa located at the magnetic equator, with the equator sweeping southward across the moon, panel (a)), and $\lambda_{III} = 191^\circ$ (Europa located at maximum distance above the magnetic equator, panel (b)). Electrons which bounce in Jupiter's southern hemisphere are denoted with solid lines, while electrons which bounce in the northern hemisphere are represented with dashed lines. Displacements of electrons with identical velocity magnitudes perpendicular to the magnetic field, but oppositely-oriented velocities along the magnetic field, are represented with the same color. Positive values of r_{az} correspond to displacement toward downstream (i.e., in the positive x direction) in the forward-tracing picture. A horizontal, red, dashed line indicates the diameter of Europa's disc, that is, $2 R_E$.

equator, the azimuthal displacements fall below the diameter of Europa's disc ($2 R_E$, dashed red line in Figure 2) above energies of approximately 5 keV, that is, within the entire energy range analyzed in our study. Such electrons bounce too rapidly to drift more than one European diameter in a single half-bounce period, and therefore may make multiple “attempts” to impact the moon. The displacements plateau at approximately $0.2 R_E$ between 100 keV and 10 MeV, regardless of equatorial pitch angle.

When Europa is located at its maximum elongation north of the magnetic equator (blue field line in Figures 1, and Figure 2b), the distance that an electron which bounces in Jupiter's southern hemisphere (solid lines) must travel along the Jovian field lines to reach its mirror point is substantially larger than when the moon is located at the equator. The half-bounce periods of electrons that bounce in the south are therefore larger, and the particles return farther downstream after a half-bounce (in the forward-tracing picture). In contrast, electrons which bounce in Jupiter's northern hemisphere must travel a shorter distance along the field lines compared to when Europa is at the magnetic equator, and their azimuthal displacements are shortened (dashed lines in Figure 2). For example, a forward-traced, 10 keV electron which bounces in Jupiter's southern hemisphere with $\alpha_0 = 30^\circ$ (solid blue line in Figure 2b) is displaced by $r_{az} \approx 2 R_E$ toward downstream during a half-bounce period. An electron with the same energy and velocity perpendicular to the magnetic field, but which bounces in Jupiter's northern hemisphere (i.e., $\alpha_0 = 150^\circ$, dashed blue line in Figure 2b), is only displaced by $r_{az} \approx 1.2 R_E$. Therefore, an electron which bounces in the south will return farther downstream than an electron which bounces to the north. Thus, electrons bouncing in Jupiter's northern hemisphere potentially have greater access to the moon's downstream ($x > 0$) surface. The reverse is true when Europa is located at its maximum distance *below* the

magnetic equator ($\lambda_{III} = 26^\circ$, orange field line in Figure 1). In this case the displacements of electrons which bounce in Jupiter's northern hemisphere are enhanced, and those of electrons which bounce in Jupiter's southern hemisphere are reduced.

After completing a half-bounce period, backtraced electrons are re-injected into the simulation domain with their x coordinate shifted by $-r_{az}$. The y and z coordinates of the electron are returned to their values at the point when it exited the domain. While the approach of Roederer (1967) provides the *location* of the electron when it re-enters the GENTOO domain, it does not provide information on the returning electron's gyrophase. As such, the gyrophase of the returning electron must be prescribed within our model. At Europa, the gyroradii of energetic electrons with $5 \text{ keV} \leq E \leq 10 \text{ MeV}$ are much smaller than 10% of a moon radius. Therefore, electrons are not able to avoid impacting the moon purely by gyrating around it. If the tube-like envelope defined by the particle's helical trajectory intersects the moon, the electron will practically always impact the surface, regardless of its gyrophase. The locations where these electrons with "non-valid" trajectories impact the moon do not affect electron precipitation patterns, since these electrons do not possess physical, real-world counterparts in the forward-tracing picture and are deleted from the simulation. Therefore, it is safe to re-inject energetic electrons with the same gyrophase (i.e., the same velocity vector perpendicular to the magnetic field) as when they initially left the simulation domain. The velocity component of the electron along the magnetic field is reversed upon re-injection, that is, the pitch angle is "flipped" across the 90° mark. For example, an electron which exits the simulation domain with a pitch angle of 65° is re-injected with a pitch angle of 115° . Electrons which leave Europa's interaction region with pitch angles below 2° or above 178° have mirror points inside Jupiter's loss cone, and are deleted from the simulation. A returning electron in our model will again travel through Europa's local environment, where it may have another chance to impact the moon. If the electron again evades hitting the moon, it may once again leave the box and embark on another bounce. This process continues until the electron either impacts the moon and becomes forbidden, or exits the upstream face of the box as is considered to have an allowed trajectory.

The contributions of backtraced electrons with allowed trajectories to the surface flux at their "launch point" are calculated using Liouville's Theorem, which states that the phase-space density is conserved along a dynamical trajectory in the absence of collisions or wave-particle interactions. At Europa, ion-cyclotron waves (e.g., Desai et al., 2017; Nénon et al., 2018; Volwerk et al., 2001) and whistler waves (e.g., Shprits et al., 2018) may scatter electrons and produce localized phase-space depletions. However, the locations, growth times, and saturation amplitudes of such wave fields are only scarcely constrained through the limited available observations. The possible occurrence of wave-particle interactions near Europa therefore represents an uncertainty in our model, and constraining the role of this effect is currently not feasible. We therefore apply Liouville's Theorem as an approximation, similar to Cassidy et al. (2013), Poppe et al. (2018), Liuzzo et al. (2020, 2022), and Addison et al. (2021, 2022).

Employing Liouville's Theorem allows for a relation to be drawn between the undisturbed ambient electron differential flux $I(E)$ measured by spacecraft (e.g., Paranicas et al., 2001), and the influx at the surface. The differential surface flux dJ/dE (in electrons/($\text{cm}^2 \text{ s keV}$)) is related to the phase-space density $f(p)$ by the relation (Schulz & Lanzerotti, 1974)

$$\frac{dJ}{dE} = f(p) p^2 |\hat{\mathbf{e}}_p \cdot \hat{\mathbf{e}}_N| d\Omega_v, \quad (2)$$

where

$$p = \gamma m_0 |\mathbf{v}| = \gamma m_0 c \left[1 - \left(\frac{E}{m_0 c^2} + 1 \right)^{-2} \right]^{1/2} \quad (3)$$

is the electron's momentum, $\hat{\mathbf{e}}_p$ is the unit vector parallel to the electron's momentum, $\hat{\mathbf{e}}_N$ is the local surface normal vector, and $d\Omega_v = \sin(\theta_v) \Delta\theta_v \Delta\phi_v$ is the solid angle element in velocity space. Employing Liouville's Theorem to equate the values of $f(p)$ upstream and at the surface yields a relation between the measured upstream differential flux $I(E)$ and the differential surface influx dJ/dE ,

$$\frac{dJ}{dE} = \left(\frac{p_{surf}}{p_{amb}} \right)^2 I(E_{amb}) (\hat{\mathbf{e}}_p \cdot \hat{\mathbf{e}}_N) d\Omega_v. \quad (4)$$

Here p_{surf} and p_{amb} are the electron's momentum at the surface and in the ambient environment, respectively, and E_{amb} is the electron's kinetic energy when it escapes the GENTOO domain and its trajectory becomes "allowed." To represent the undisturbed electron flux outside of the region perturbed by Europa's plasma interaction, $I(E_{amb})$, we adopt the empirical fit of Paranicas et al. (2009), which takes into account observations by the Pioneer, Voyager, and Galileo spacecraft (Cooper et al., 2001; Divine & Garrett, 1983; Paranicas et al., 2001). The Galileo spacecraft measured the electron flux $I(E_{amb})$ near Europa both when the moon was located near the center of the plasma sheet (during the E12 flyby) and near its maximum distance from the center of the plasma sheet (E26, see Paranicas et al., 2001). These measurements showed only a very minor variation between the ambient electron fluxes detected during these flybys, within a factor of ≈ 2 . The electron distribution measured during the E4 flyby, which occurred when Europa was at an intermediate distance from the center of the sheet, showed higher fluxes by approximately an order of magnitude compared to E12 and E26, but only in the energy regime below ≈ 200 keV. However, Paranicas et al. (2009) note that these differences are likely the result of uncertainties related to calibration issues with the detector, and not variability in the magnetospheric environment. We therefore use the same ambient electron flux distribution $I(E_{amb})$ in our model for all four positions of Europa relative to the Jovian plasma sheet. We note that the electron count rates observed by Galileo were saturated at Europa's orbital distance (Kollmann et al., 2018). Therefore, the ambient electron fluxes may indeed be slightly higher than reported by Paranicas et al. (2009). At the time of writing, differential electron fluxes from Juno's crossings of Europa's L-shell or the close flyby on 29 September 2022 were not yet available in the literature.

Energetic electron pitch angle distributions (PADs) within the Jovian magnetosphere vary strongly with both magnetic latitude and radial distance. Galileo and Juno observations (e.g., Ma et al., 2021; Nénon et al., 2022) show that the PAD near Europa varies with the time of observation and magnetic latitude between nearly-isotropic and pancake distributions (which feature the maximum flux near pitch angles of 90°). For our study, we treat the energetic electron PAD at Europa as isotropic. However, in Section 3.5, we constrain the robustness of our results by briefly examining the role that a pancake distribution would play in modifying the electron influx pattern onto Europa.

2.3. Electron Sputtering Yields

In order to determine the sputtering rates (in molecules/(cm² s)) of molecular oxygen from Europa's surface, we multiply the differential electron flux that reaches a given surface location dJ/dE by the respective energy-dependent sputtering yield $Y(E)$ (in molecules/electron) and integrate over the entire energy range studied. The physical mechanisms underlying electron sputtering differ from those of ion sputtering. While both ions and electrons lose energy due to electron excitations in the surface material, the secondary energy loss process for ions is elastic collisions with neutral molecules, while for electrons it is ionization of such molecules (e.g., Teolis et al., 2017). Impinging electrons also penetrate up to several orders of magnitude deeper into Europa's surface than protons or heavy ions, and as such deposit their energy over a substantially larger distance within the surface (up to 1 cm at 10 MeV energies, see Nordheim et al., 2018; Teolis et al., 2017; Ziegler & Manoyan, 1988).

Laboratory data on electron sputtering yields from water ice films at European surface temperatures (≈ 70 – 140 K) are sparse compared to those available for ions (e.g., Davis et al., 2021; Galli et al., 2018; Meier & Loeffler, 2020; Orlando & Sieger, 2003; Vorburger & Wurz, 2018). Radiolysis of H₂O ice in Europa's surface leads to the creation of O₂ and H₂ within the upper layers of the surface ice. Teolis et al. (2017) analyzed the deposition of electron energy with depth in a thin, O₂-bearing ice layer to develop an empirical model of O₂ sputtering yields from electron impacts. The model of Teolis et al. (2017) determines electron sputtering yields of O₂ based upon the energy E and the (energy-dependent) penetration depth $r_0(E) \cos(\theta_v)$, where θ_v is the incidence angle of the projectile measured against the local surface normal. The quantity $r_0(E)$ is the penetration range along the track of the electron within the ice, so $r_0(E) \cos(\theta_v)$ is the depth along the surface normal that the electron penetrates into the ice. Teolis et al. (2017) suggested that the radiolytically-produced O₂ is concentrated in an approximately 28 Å thin layer at the very top of the moon's icy surface. Energetic electrons with energies in the keV–MeV range, which penetrate 10^3 – 10^8 Å into the surface (Teolis et al., 2017; Ziegler & Manoyan, 1988), therefore deposit much of their energy at depths below the sputterable O₂ layer. The electron sputtering yields of Teolis et al. (2017) therefore monotonically fall by several orders of magnitude above 300 eV, since electrons with these energies "waste" most of their energy at surface depths where sputterable O₂ is not present in high concentrations. Radiolytic O₂ production in this 28 Å surface layer increases with surface temperature, causing

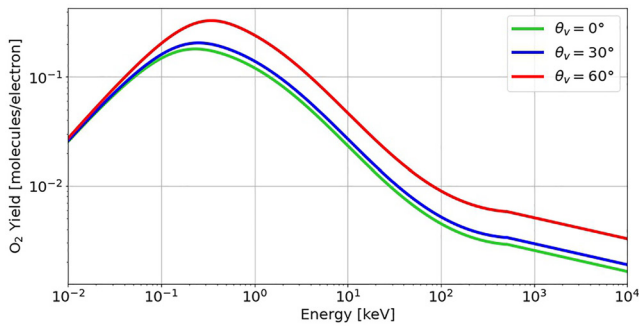


Figure 3. The O₂ sputtering yields from 10 eV–10 MeV electron impacts, calculated with the model of Teolis et al. (2017) for a surface temperature of $T = 100$ K and incidence angles of $\theta_v = 0^\circ$ (green curve, normal incidence), $\theta_v = 30^\circ$ (blue curve), and $\theta_v = 60^\circ$ (red curve). These curves have been scaled with a factor of 0.3, as suggested by Teolis et al. (2017) to match experimental data.

Teolis et al. (2017) suggest that their empirical yield curve be uniformly scaled by a factor of 0.3. In Figure 3 we plot the O₂ sputtering yield $Y(E)$ of electrons from the model of Teolis et al. (2017) for several incidence angles: $\theta_v = 0^\circ$ (i.e., normal incidence, green curve), $\theta_v = 30^\circ$ (blue curve), and $\theta_v = 60^\circ$ (red curve). All three curves have already been multiplied with the scaling factor of 0.3 suggested by Teolis et al. (2017). The yields in Figure 3 were determined with a constant surface temperature of $T = 100$ K, which is approximately the median surface temperature at Europa (Spencer et al., 1999). Initially the yields rise with increasing projectile energy from ≈ 10 to 300 eV, as electrons with higher energies deposit more energy into the O₂-bearing surface layer. However, above 300 eV, the penetration depth of the electrons begins to vastly exceed the O₂ layer thickness of 28 Å, and the electrons deposit most of their energy at depths where the O₂ concentration is negligible. The sputtering yields therefore monotonically decrease by roughly two orders of magnitude from 300 eV to 10 MeV (the highest energy considered in our study). Electrons which impact the surface with incidence angle $\theta_v = 60^\circ$ (red curve) sputter roughly twice as much material as electrons with $\theta_v = 0^\circ$ (green curve) at 10 MeV, demonstrating the sensitivity of sputtering yields to projectile incidence angle.

A recent study by Davis et al. (2021) performed laboratory measurements of the sputtering yields from H₂O ice due to 500 eV electron impacts over a temperature range from 14.5 to 125 K. Their results suggest that a scale factor of 0.14 should be applied to the yield curve of Teolis et al. (2017), rather than a factor of 0.3. We will apply scale factors of both 0.3 and 0.14 to the electron sputtering yields in order to constrain the robustness of our results against the uncertainties introduced by the choice of sputtering model (Davis et al., 2021; Teolis et al., 2017).

In contrast to the model of Teolis et al. (2017), Vorburger and Wurz (2018) suggest that the electron sputtering yields of O₂ plateau at a constant value of $Y = 2$ at energies above the ≈ 300 eV maximum in Figure 3, based upon laboratory experiments by Galli et al. (2018). They therefore modified the electron yield curve of Teolis et al. (2017) at energies $E \leq 300$ eV to increase to a value of $Y = 2$ at 300 eV, and then remain constant at this value for energies above 300 eV. Thus, their approach treats the yields as *constant* over the *entire* energy range analyzed in our study. Their model assumes normal incidence for all impinging electrons, and a constant surface temperature of 125 K, approximately the mean temperature of Europa's *dayside* surface (Spencer et al., 1999). As can be seen from the green curve in Figure 3, the constant value of $Y = 2$ is 1–2 orders of magnitude larger than the yields from Teolis et al. (2017) at normal incidence. We note that such a plateau in the sputtering yields above 300 eV was not observed in a subsequent experimental study by Meier and Loeffler (2020), who instead found a decrease at high energies consistent with the model of Teolis et al. (2017).

By calculating the O₂ sputtering rates with the yield models of Teolis et al. (2017), Davis et al. (2021), and Vorburger and Wurz (2018), we will constrain how different approaches to describe these yields affect the resulting contribution of electron sputtering to exosphere generation at Europa, especially relative to the sputtering contribution of magnetospheric ions.

the yields to grow exponentially with temperature above ≈ 80 K (e.g., Famá et al., 2008; Teolis et al., 2017). H₂ is released stoichiometrically from the surface ice, resulting in a 2:1 ratio between the number of sputtered H₂ and O₂ molecules. The sputtering yields (and associated sputtering rates) of H₂ are therefore exactly twice those of O₂.

The O₂ and H₂ sputtering yields of electrons in the model of Teolis et al. (2017) are dependent upon the incidence angle θ_v of the projectile when it impacts the surface, with nearly tangential impacts sputtering up to an order of magnitude more material than normal impacts (i.e., $\theta_v = 0^\circ$). To facilitate comparison to our earlier results for ion sputtering, we proceed analogous to Addison et al. (2022) and determine O₂ sputtering rates with the actual incidence angle of each electron onto a perfect sphere calculated with GENTOO.

Since the method of Teolis et al. (2017) is a general sputtering model for any projectile species penetrating into water ice, the resulting yield curves need to be multiplied with a scaling factor in order to match laboratory measurements of sputtering yields from specific projectiles. To be consistent with laboratory data on electron sputtering yields at low energies (10–30 eV),

Since O_2 sputtering yields increase with temperature, it is necessary to model Europa's surface temperature profile when calculating maps of the O_2 sputtering rates. The moon's surface temperature varies between 60 K at the poles and 130 K at the sub-solar point (Spencer et al., 1999). The nightside hemisphere does not become as cold as the poles, since Europa's non-zero thermal inertia causes the ice to retain heat as a surface element rotates out of the dayside hemisphere. Over the course of a Europan day (≈ 80 hr), the sub-solar point migrates across the moon's surface. The longitudinal distance between the sub-solar point and the upstream apex therefore varies with time. The albedo of Europa's upstream hemisphere is approximately 0.2 lower than that of the downstream hemisphere (0.45–0.65, respectively), due to darkening by exogenic ion implantation. When illuminated, the upstream hemisphere therefore absorbs more solar irradiation, and heats to a higher temperature than the downstream hemisphere does when it is illuminated. Addison et al. (2022) calculated O_2 (and H_2) sputtering rates from ion impacts with a diurnally-averaged temperature profile in order to take into account spatial variations in Europa's surface temperature that are persistently present. For instance, this approach accounts for the colder polar caps, warmer equator, and higher temperatures around the upstream apex compared to the downstream apex (see Figure 3 in that study). For this study of electron sputtering rates of O_2 and H_2 , we proceed analogous to Addison et al. (2022) and apply the diurnally-averaged temperature profile from their Figure 3. Comprehensively examining the role of both (a) the relative location of Europa's dayside and upstream apices and (b) the moon's position relative to the Jovian magnetic equator would require a prohibitive number of simulations, and is beyond the scope of this investigation.

The sputtering yields of intact H_2O molecules due to electron impacts on water ice are not well constrained in the available literature. While O_2 and H_2 yields grow rapidly with temperature throughout the range of surface temperatures present at Europa, H_2O sputtering is independent of surface temperature in this range (Davis et al., 2021; Famá et al., 2008). Thus, the fraction of H_2O , O_2 , and H_2 in the sputtered material varies with temperature (Davis et al., 2021). Laboratory studies of the composition of sputtered material due to 200 eV–10 keV electron impacts on water ice indicate that the O_2/H_2O ratio of the ejected material is approximately 3.3 at surface temperatures of 90 K (Galli et al., 2018). A study by Abdulgalil et al. (2017) performed a similar laboratory analysis at 112 K, and also found that O_2 was the dominant sputtered product from electron impacts. However, Davis et al. (2021) estimated a significantly lower value of 0.44, that is, H_2O would dominate the composition of the ejecta. These authors attributed this discrepancy to differences in the laboratory setups between their study and those of Galli et al. (2018) and Abdulgalil et al. (2017). In addition to these uncertainties, there is currently no published model of the energy dependence of H_2O sputtering yields from electron impacts onto water ice. As such, we do not model the sputtering rate of H_2O from electron impacts in this study.

3. Model Results

3.1. Europa's Perturbed Electromagnetic Environment

In Figure 4, we present the results of the four AIKEF simulations described in Section 2.1. The first column (Figures 4a–4c) displays the modeled electromagnetic fields while Europa is located at the Jovian magnetic equator, and the equator is sweeping *southward* over the moon ($\lambda_{III} = 110^\circ$), while the second column (Figures 4d–4f) shows the fields while Europa is located at the magnetic equator and the equator is sweeping *northward* over the moon ($\lambda_{III} = 284^\circ$). The third column (Figures 4g–4i) shows the electromagnetic fields while Europa is located at its maximum distance *above* the Jovian magnetic equator ($\lambda_{III} = 191^\circ$), and the fourth column presents the electromagnetic fields when the moon is located at its maximum distance *below* the magnetic equator ($\lambda_{III} = 26^\circ$). The first, second, and third rows display the flow-aligned component of the magnetic field B_x , the magnitude of the magnetic field $|B|$, and the magnitude of the electric field $|E|$, respectively. Each quantity in Figure 4 is presented in the $y = 0$ plane of the EPhiO system. Europa's perturbed electromagnetic environment within the framework of the AIKEF model has been described at length in our previous studies (e.g., Addison et al., 2021, 2022; Arnold, Liuzzo, & Simon, 2020; Breer et al., 2019), and we therefore present only a brief overview of the features that are immediately relevant to the interpretation of our electron influx maps (Sections 3.2–3.5).

Electron impact ionization of Europa's exosphere leads to mass-loading of the plasma above the orbital trailing hemisphere, causing the Jovian magnetospheric field lines to drape around the moon. Mass-loading also powers a pair of Alfvén wings which propagate along their characteristics $\mathbf{u}_0 \pm \mathbf{V}_{A,0}$ (where $\mathbf{V}_{A,0} = \mathbf{B}_0 / \sqrt{\mu_0 m_0 n_0}$ is the Alfvén velocity in the undisturbed upstream flow). The draping and Alfvén wing formation is evident in the flow-aligned field component (B_x) for all four cases (Figures 4a, 4d, 4g, and 4j). Inside the northern Alfvén wing

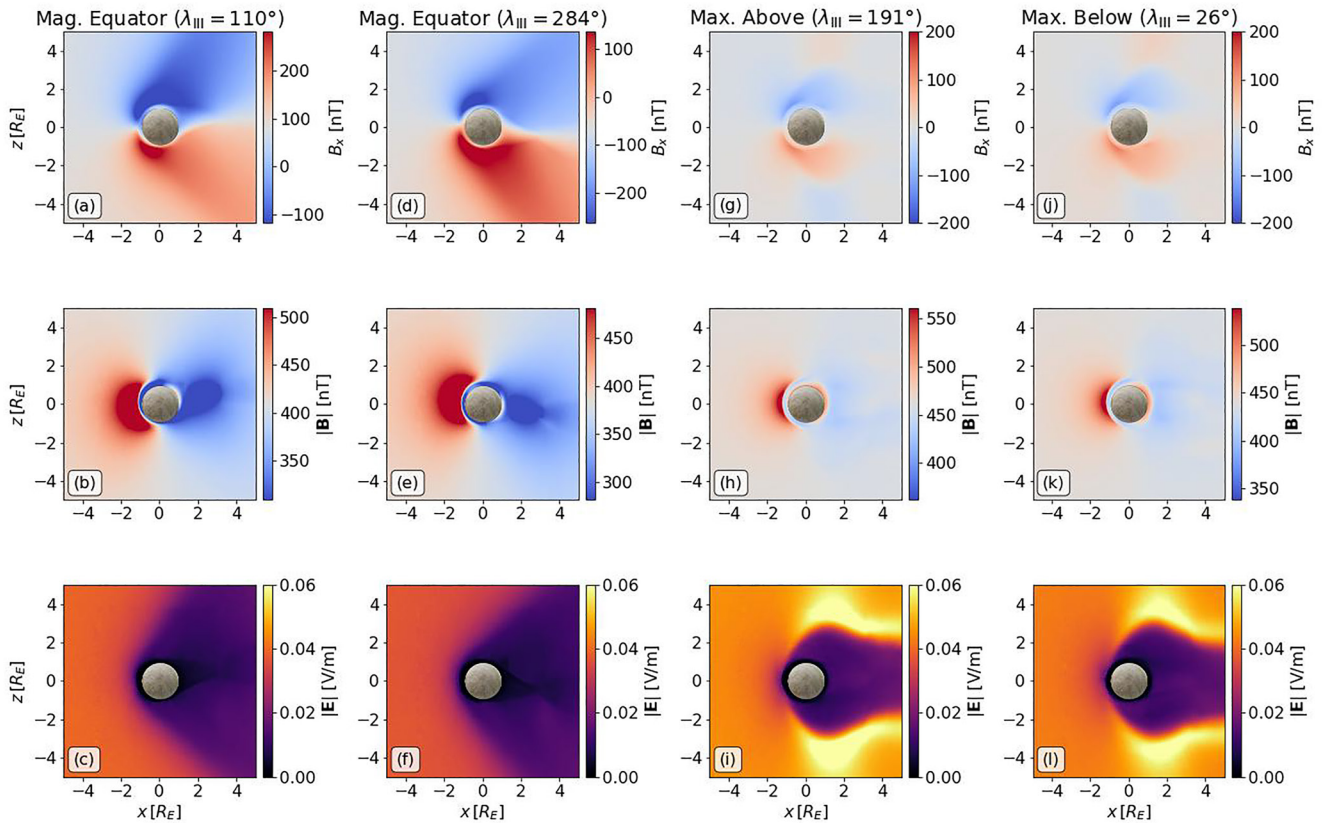


Figure 4. Electromagnetic field configurations near Europa from the AIKEF simulations, calculated for the four system III longitudes given in Table 1. The top row (panels a, d, g, and j) shows the flow-aligned component of the magnetic field B_x , the middle row (panels b, e, h, and k) shows the magnitude of the magnetic field $|B|$, and the bottom row (panels c, f, i, and l) shows the magnitude of the electric field $|E|$. Each quantity is shown in the $y = 0$ cross-section in the EPhiO system, that is, in a plane that contains the corotation velocity vector \mathbf{u}_ϕ , the vector aligned with Jupiter's spin axis z , and the center of the moon.

tube (i.e., $z > 0$) the draping of the magnetic field lines causes the field to have a component oriented antiparallel to the upstream flow, while within the southern wing tube ($z < 0$) the draped field has a component parallel to the flow direction. When the moon is located at the Jovian magnetic equator (first two columns of Figure 4), the $y = 0$ cross-section of the EPhiO system bisects the Alfvén wing tubes (since $B_{0,y} = 0$, see Table 1), and the draping is clearly evident as an extended region of negative B_x north of the moon (blue) and a similar region of positive B_x south of the moon (red). The nonzero $B_{0,x}$ component of the background field rotates the Alfvén wing characteristics clockwise ($\lambda_{III} = 110^\circ$) or counterclockwise ($\lambda_{III} = 284^\circ$) around the $+y$ axis, although this component is insufficient to rotate either of the wings into the space upstream of the moon (e.g., Liuzzo et al., 2021; Simon et al., 2022). In this configuration, the upstream plasma density, and hence the strength of the interaction, is maximized. The magnitude of the perturbation to B_x reaches approximately 30% of the background field strength B_0 in these two cases.

At Europa's maximum elongation above or below the magnetic equator (third and fourth columns of Figure 4, respectively), signatures of field line draping are also present, with perturbations to B_x visible in Figures 4g and 4j. However, in these two cases the Alfvén wing characteristics are rotated around the x axis and out of the $y = 0$ plane by approximately 30° . Therefore, the $y = 0$ cross-sections shown in Figure 4 cut an oblique slice through the Alfvén wing tubes. Near the moon, this slice intersects the draped field lines within the wing tubes, causing a similar signature in B_x as seen at the magnetic equator: negative B_x (blue) north of the moon, positive B_x (red) south of the moon. However, farther from the moon ($z \approx \pm 3 R_E$), the $y = 0$ slice cuts through the outer regions of the Alfvén wing tubes, and encounters regions of positive B_x (red) in the north and negative B_x (blue) in the south. This “anti-draping” of the field outside of the Alfvén wing tubes is required to ensure closure of the magnetic field lines in planes perpendicular to the wing characteristics: in these planes, the field geometry can be described by a magnetic dipole (Neubauer, 1980). Observational confirmation for this “anti-draping”

was found in Cassini magnetometer data from several Titan flybys (Simon et al., 2013). At these large distances between Europa and Jupiter's magnetic equator, the upstream density is lowered by a factor of 5 compared to the center of the plasma sheet (see Table 1). As such, the interaction is weaker (see also Harris et al., 2021), and the perturbations to the B_x component are only roughly 12% of the background field magnitude (Figures 4g and 4j).

Mass-loading of the corotating plasma also causes the Jovian magnetic field lines to pile up above Europa's upstream hemisphere. This accumulation in magnetic flux leads to an enhancement of the field magnitude in this region, visible in the second row of Figure 4 at all four system III longitudes as a red region centered near the upstream apex ($x \approx -1 R_E$, $z = 0$). When Europa is located at the magnetic equator, the field magnitude in the pileup region is enhanced by up to 150 nT ($\approx 35\%$ of B_0). At maximum distance above or below the magnetic equator, the field magnitude in the pileup region is enhanced by only about 50 nT ($\approx 11\%$ of B_0). The upstream pileup is accompanied by a reduction in field strength above the moon's downstream hemisphere (blue region in Figures 4b, 4e, 4h, and 4k). In the downstream region, the field magnitude is reduced by about 50 nT when Europa is located above or below the Jovian magnetic equator. At the magnetic equator this wake reduction in field strength can be up to several hundreds of nT (Figures 4b and 4e). When Europa is located far above or below the Jovian magnetic equator, the moon's induced magnetic moment is oriented along the $\pm y$ axis, and the induced field reaches a peak strength of approximately half of the magnetospheric background field strength at the surface. The induced field amplifies the field strength within approximately $0.2 R_E$ of Europa's downstream hemisphere in the $y = 0$ plane, leading to a localized enhancement in field magnitude there (red crescent-shaped feature near $x = 1 R_E$ in Figures 4h and 4k). Such an enhancement was also found (through both Galileo observations and modeling) above Callisto's downstream hemisphere (see, e.g., Figure 4d of Liuzzo et al., 2016).

Ionization of Europa's exosphere leads to the injection of O_2^+ ions into the ambient magnetospheric plasma. Inside the moon's geometric wake, as well as within approximately $0.5 R_E$ of the surface, these slow-moving ions dominate the plasma density (see also, e.g., Arnold, Liuzzo, & Simon, 2020). Thus, the bulk plasma velocity $|\mathbf{u}|$ in the moon's wake is reduced by nearly an order of magnitude. Farther north and south of the moon, the draped field lines divert the upstream plasma around the interaction region. Since distance is required for the drifting plasma to re-accelerate to the corotation velocity, the plasma velocity is also reduced downstream of the Alfvén wings (purple in Figures 4c, 4f, 4i, and 4l). Hence, immediately downstream of the moon and its Alfvén wings the bulk velocity, and thus the convective electric field $\mathbf{E} = -\mathbf{u} \times \mathbf{B}$, is reduced by approximately a factor of 5 (purple regions in Figures 4c, 4f, 4i, and 4l).

The upstream plasma flow is also accelerated around the flanks of the Alfvén wing tubes, generating localized enhancements in the electric field magnitude. Since at maximum elongation above or below the Jovian magnetic equator the $y = 0$ plane intersects the outer flanks of the wings, these enhancements are visible as bright yellow regions in Figures 4i and 4l. However, the $y = 0$ plane does *not* intersect the outer flanks of the Alfvén wing tubes when Europa is located at the magnetic equator. Thus, such an enhancement in $|\mathbf{E}|$ is not visible in Figures 4c and 4f.

3.2. Spatial Distribution of Energetic Electron Flux Onto Europa's Surface

3.2.1. Europa Located at the Jovian Magnetic Equator (Southward Sweep, $\lambda_{\text{III}} = 110^\circ$)

Figure 5 displays maps of the differential electron surface number flux (in electrons/($\text{cm}^2 \text{ s keV}$)) when Europa is located at the Jovian magnetic equator, and the equator is sweeping *southward* over the moon ($\lambda_{\text{III}} = 110^\circ$, $B_{0,x} > 0$). The left column (Figures 5a, 5c, 5e, and 5g) displays maps of the differential surface flux calculated with a superposition of the Jovian background field and Europa's induced dipole field, that is, without plasma interaction currents. The right column (Figures 5b, 5d, 5f, and 5h) presents maps of the differential number flux onto the surface calculated with the draped electromagnetic fields from AIKEF, that is, with plasma currents included. Each row displays the surface flux from electrons of a specific energy when impacting Europa, sampling the entire energy range under consideration: $E = 10 \text{ keV}$ (Figures 5a and 5b), $E = 100 \text{ keV}$ (Figures 5c and 5d), $E = 1 \text{ MeV}$ (Figures 5e and 5f), and $E = 10 \text{ MeV}$ (Figures 5g and 5h). The maps are presented in the European West Longitude system, with the moon's upstream apex located in the center of each plot at 270°W , the sub-Jovian apex at 0°W , the downstream apex at 90°W , and the anti-Jovian apex at 180°W . The latitude goes from 90°N (Europa's north pole) to 0° (Europa's equator) to 90°S (Europa's south pole). While GENTOO

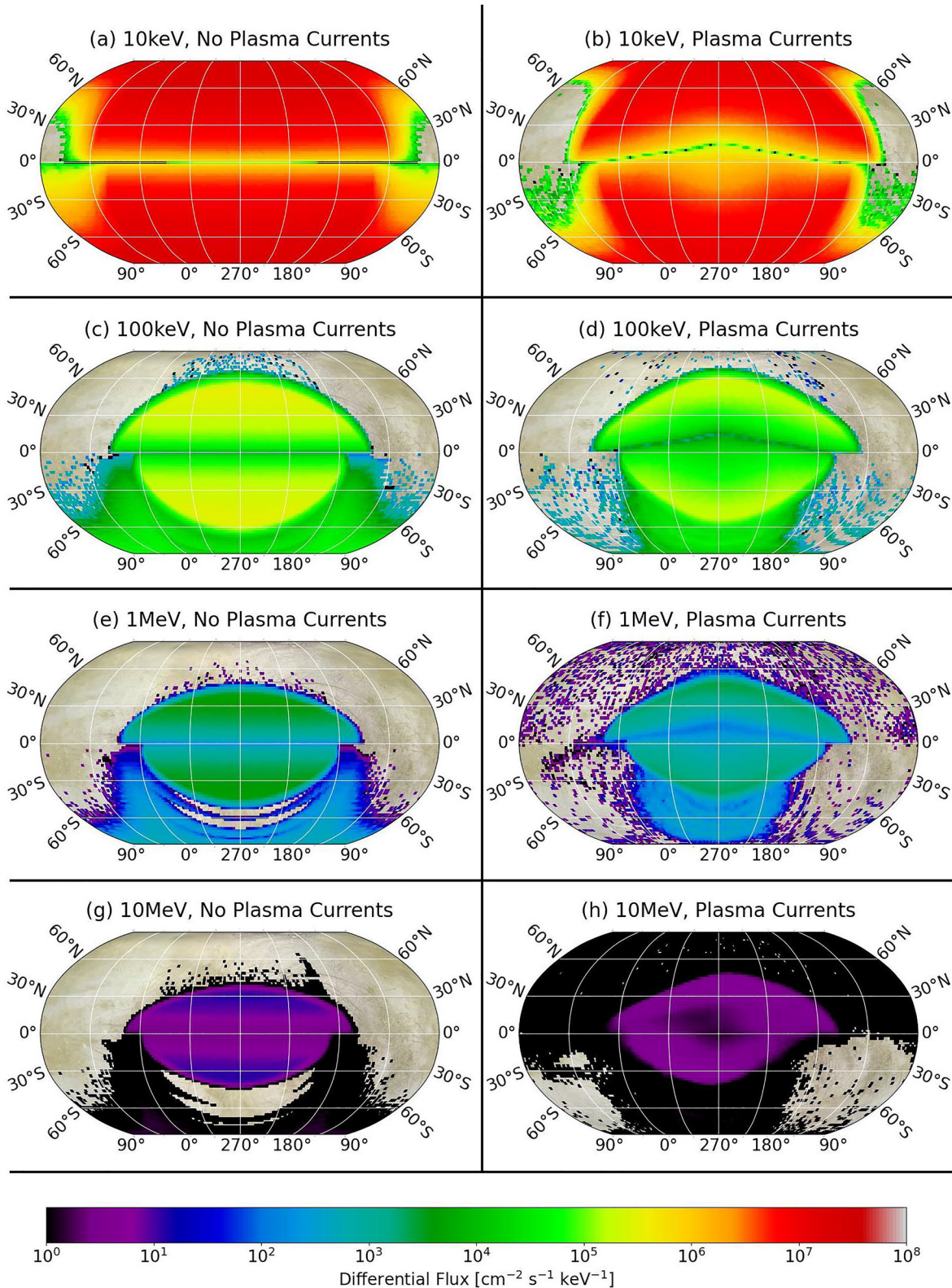


Figure 5.

calculates trajectories backwards in time to enhance numerical efficiency, electron dynamics in this section will be discussed exclusively in a forward-tracing picture to facilitate interpretation of the relevant physics.

When we consider only a superposition of the Jovian background field and Europa's induced field (i.e., no plasma currents are included), 10 keV electrons irradiate almost every region of the moon's surface (Figure 5a). The differential flux of 10 keV electrons is approximately $10^7 \text{ cm}^{-2} \text{ s}^{-1} \text{ keV}^{-1}$ across almost the entire upstream hemisphere (180°W – 0°W longitude), as well as the polar regions of the downstream hemisphere (above latitudes of 60°N and below 60°S). The azimuthal displacement r_{az} experienced by a 10 keV electron that completes a single half-bounce between Europa's interaction region and its mirror point in the Jovian magnetosphere is approximately 1 – $1.5 R_E$ (Figure 2a). Therefore, a flux tube which comes into contact with Europa will gradually deposit its content of 10 keV electrons into the surface as it drifts approximately $1.5 R_E$ toward downstream across the moon's disc. Thus, nearly every surface region which is within $1.5 R_E$ in x direction of the point where an impinging flux tube initially contacts the surface receives approximately a uniform level of irradiation from 10 keV electrons (red regions in Figure 5a).

Once the flux tube has drifted $1.5 R_E$ downstream of its initial contact point with the surface, it becomes nearly depleted of 10 keV electrons. Only electrons with pitch angles around $\alpha_0 = 0^\circ$ or $\alpha_0 = 180^\circ$ can bounce, return, and reach the regions which are $1.5 R_E$ downstream of the point where the flux tube first contacted the moon. Electrons with pitch angles less than 2° or greater than 178° are lost to the planetary loss cone, and cannot irradiate Europa's downstream hemisphere beyond $x = 1.5 R_E$. The electron number flux onto Europa begins to lessen toward the mid-to-low latitudes on the moon's downstream surface (45° – 135° W between 60°N and 60°S) as the flux tube becomes completely depleted of electrons. The differential flux of 10 keV electrons onto the downstream hemisphere equatorward of 30°N/S latitude falls by approximately four orders of magnitude from $45^\circ/135^\circ\text{W}$ to the downstream apex (90°W).

A large swath of the downstream hemisphere between 30°N and the equator receives zero 10 keV electron influx, as any flux tube moving over the moon in x direction is completely depleted of 10 keV electrons by the time it makes it to this region of the surface. This downstream depletion is not symmetric between both sides of the moon's equator; it is slightly displaced toward northern European latitudes. Since the background magnetic field is tilted toward downstream ($B_{0,x} > 0$), the flux tubes which impinge upon Europa form an angle of approximately 11° against the ($-z$) axis. Thus, the regions where drifting field lines first contact Europa's surface are located along the upstream half of a great circle which is tilted by 11° against the x axis. The surface regions which are *farthest* from the initial contact points are located along the downstream portion of this great circle, and can therefore be found around 11°N latitude. Thus, flux tubes which impinge upon Europa's surface are most depleted of electrons before reaching the downstream hemisphere slightly north of the geographic equator. The tilt of the background field therefore causes the zero-flux region of 10 keV electrons on the downstream hemisphere to be skewed toward northern latitudes. However, since the strongest tilt of the background field along the corotation direction (namely, 11°) occurs at the Jovian magnetic equator (e.g., Kivelson et al., 1999), this effect generates rather subtle asymmetries in the surface irradiation pattern.

An exception to the quasi-uniform 10 keV electron surface flux onto the upstream hemisphere is a narrow “belt” along the equator, where the differential number flux rapidly drops by 2–8 orders of magnitude. Even with their diminutive gyroradii (about $5 \times 10^{-4} R_E$ at 10 keV), electrons following field lines which intersect Europa tend to gyrate into the moon before being able to reach the regions where the field lines are tangent to the surface. Interestingly, this reduction belt does *not* occur along the 11° tilted great circle where the background magnetic field is tangent to the surface: the induced field distorts the picture that would be expected from purely uniform magnetic fields. Near Europa's upstream and downstream apices (90° and 270°W), the induced field severely weakens the B_x component of the field, causing the field vectors near the surface to be oriented almost entirely in the $-z$ direction (e.g., Saur et al., 2010; Zimmer et al., 2000). Thus, the ring where the field is almost entirely tangential

Figure 5. Maps of the differential electron number flux onto Europa's surface while the moon is located at the Jovian magnetic equator and the equator is sweeping *southward* across the moon ($\lambda_{\text{III}} = 110^\circ$, $B_{0,x} > 0$). The left column displays differential fluxes calculated with a superposition of the Jovian background magnetic field and Europa's induced dipole field (i.e., no plasma currents included), while the right column displays differential fluxes calculated while also including the plasma currents from the AIKEF model. Each row displays differential fluxes for a select starting energy E of backtraced electrons at Europa's surface, ranging from 10 keV to 10 MeV. The differential flux maps are displayed on a Robinson orthographic projection, with the moon's upstream apex (270°W) located in the center of each plot, the sub-Jovian apex located at the left middle (0°W), the downstream apex located at the left/right edges (90°W), and the anti-Jovian apex located at the right middle (180°W).

to the surface is “pinned” to the near-equatorial region by the induced field. The ring of reduced electron flux is therefore located at the geographic equator, even with a background magnetic field which is slightly tilted in the x direction. A similar mechanism has been identified at Ganymede by Saur et al. (2015), where the induced field from the moon's subsurface ocean was found to reduce the ability of Ganymede's auroral ovals to respond to the time-varying Jovian magnetospheric field. At Europa, an equatorial belt of reduced influx has been identified previously in *ion* irradiation patterns (e.g., Addison et al., 2021; Breer et al., 2019; Nordheim et al., 2022); however the belt is substantially wider (15° north and south in latitude) for ions due to their larger gyroradii.

For energetic electrons, a similar equatorial reduction in surface flux was seen by Dalton et al. (2013) using a particle-tracing model and uniform fields (i.e., without including the induced field and plasma currents). Since their setup featured a purely southward magnetic field (and therefore no induction), the belt of reduced flux seen in that study was naturally located at the moon's geographic equator. Our results suggest that the reduction belt is persistently located near Europa's geographic equator when the moon is near the planetary magnetic equator, even when the ambient magnetospheric field is not aligned with the $-z$ axis. No reduction belt at low latitudes has been predicted by models which treat only the guiding center motion of the energetic electrons (e.g., Nordheim et al., 2018; Paranicas et al., 2001) but not their gyration: these approaches instead predict the electron flux to maximize at the upstream equator.

As their energy increases ($E \geq 100$ keV, Figures 5c, 5e, and 5g), electrons complete a half-bounce more quickly, and return to Europa's interaction region after bouncing with azimuthal displacements $r_{az} < 1 R_E$ (Figure 2). These electrons largely cannot reach Europa's downstream hemisphere, since they are rapidly depleted onto the moon's upstream hemisphere as their magnetic flux tube traverses the surface. As such, two “crescent” shaped regions of increased electron influx are formed on the upstream hemisphere. These regions (yellow regions in Figure 5c, green in Figure 5e, dark purple in Figure 5g) indicate where electrons of a given energy impact the surface while the flux tube which they populate is gradually depleted. The crescent features are separated at the equator by the belt of reduced flux, which remains “pinned” to Europa's geographic equatorial region by the induced field. This depletion belt is widened in latitude at higher energies due to the larger gyroradii of the electrons, which cause a larger fraction of them to gyrate into the surface before reaching Europa's equator (see Figures 5c, 5e, and 5g). For 100 keV electrons (Figure 5c), the azimuthal displacements r_{az} are approximately $0.5 R_E$, and thus the crescent features extend from the equatorial belt of reduced flux to approximately 60° north and south latitude (i.e., $R_E \cos(60^\circ) = 0.5 R_E$ in x direction from the upstream apex). For 1 MeV electrons, r_{az} drops to about $0.25 R_E$, and thus electrons at this energy are limited to impacting within approximately $0.25 R_E$ of where their flux tube first contacts the surface. The maximum latitude of the crescent regions for $E = 1$ MeV therefore shrinks to approximately 45° north or south of the equator (Figure 5e). At 10 MeV, r_{az} is further reduced, and the north/south edges of the upstream flux enhancements only extend to approximately 35° north or south in latitude. Similar crescent-shaped enhancements in electron irradiation have also been identified in previous modeling studies which assumed the electromagnetic fields near Europa to be uniform (e.g., Dalton et al., 2013; Nordheim et al., 2018; Paranicas et al., 2001).

In contrast to the results of models that treat the ambient field as uniform and do not include the induced dipole (e.g., Dalton et al., 2013; Nordheim et al., 2018; Paranicas et al., 2001), the crescent-shaped regions of enhanced electron number flux onto Europa's upstream hemisphere (Figure 5) do not align with each other in longitudinal extent. The southern crescent extends from approximately 180° west longitude (anti-Jovian apex) westward to 360° west longitude (sub-Jovian apex), corresponding to the longitudinal extent of Europa's upstream hemisphere (Figures 5c, 5e, and 5g). The northern crescent, however, extends approximately 20° in longitude beyond the sub-/anti-Jovian apices and into the downstream hemisphere. Since such a longitudinal asymmetry in the electron flux patterns between the northern and southern hemispheres is not seen when the electromagnetic fields near Europa are treated as spatially uniform (see, e.g., Figure 5 of Dalton et al., 2013), it must arise from how the moon's induced field reshapes the magnetic field lines in its vicinity. The induced magnetic moment at system III longitude considered here is oriented along the negative x axis (i.e., pointing toward upstream, see Table 1), and the induced field strength at the surface reaches approximately 20% of B_0 .

Figure 6 displays several magnetic field lines which pass near the anti-Jovian apex of Europa. Figure 6a displays field lines which pass through “anchor” points north of Europa (green dots) located at $y = -1 R_E$, $z = 3 R_E$, and equally-spaced intervals along the x axis. Figure 6b displays field lines which pass through “anchor” points in the south, that is, with $z = -3 R_E$, and again with $y = -1 R_E$ and equal spacing in the x direction. Energetic electrons

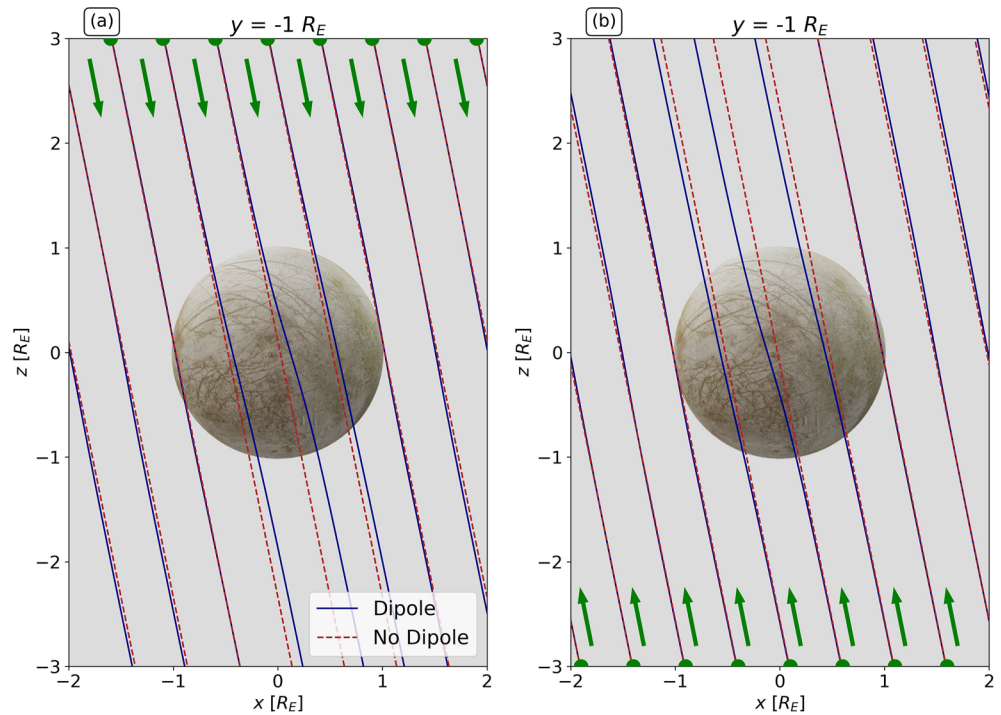


Figure 6. Sample of the magnetic field lines near Europa when the moon is located at the magnetic equator ($\lambda_{III} = 110^\circ$). The field lines shown in panel (a) pass through “anchor points” at $y = -1 R_E$, $z = 3 R_E$, and equally spaced points in x direction, while in panel (b) they pass through anchor points at $y = -1 R_E$, $z = -3 R_E$, and equally-spaced points in x direction. The field lines are projected into the $y = -1 R_E$ plane, which intersects Europa at its anti-Jovian apex. Red, dashed lines are the Jovian background magnetic field lines, while blue lines are the superposition of the Jovian magnetic field and Europa's induced dipole field. Green dots indicate the “anchor” points of the field lines at the outer edges of the domain shown, and green arrows indicate the direction of motion of electrons traveling along these field lines from north to south (panel a), or south to north (panel b).

traveling along these field lines may impact the surface near Europa's anti-Jovian apex, that is, where the longitudinal extent of the northern and southern crescents is different. The red, dashed lines represent the Jovian background magnetospheric field lines, while the blue lines denote a superposition of the Jovian background field and Europa's induced dipole field. Electrons which impinge near Europa's anti-Jovian apex while traveling from north to south follow field lines which are bent toward *downstream* by Europa's induced field, compared to an unperturbed field line which passes through the same anchor point (red vs. blue lines in Figure 6a). Such particles therefore impinge upon Europa's anti-Jovian surface displaced slightly toward *downstream*, compared to the case without an induced field. In this way, the induced dipole expands the longitudinal extent of the northern crescent feature into the downstream hemisphere.

In contrast, electrons which impinge near Europa's anti-Jovian apex while traveling from south to north follow field lines which are bent toward *upstream* by the induced field, again compared to the unperturbed magnetospheric field line which passes through the same anchor point south of Europa (Figure 6b). These electrons are thus deflected toward *upstream* by the induced field, and impact the southern hemisphere closer in longitude to the upstream apex than in the case without an induced field. The presence of the induced field therefore shrinks the longitudinal extent of the southern crescent. The longitudinal expansion of the northern crescent, combined with the shrinking of the southern crescent, causes the misalignment of the two crescent features seen in the irradiation patterns of $E \geq 100$ keV electrons near 180° west longitude (Figures 5c, 5e, and 5g). Since \mathbf{B}_0 and the induced dipole moment are parallel to the $y = 0$ plane, Europa's magnetic environment is symmetric between the $y > 0$ and $y < 0$ half spaces. Therefore, the same effect occurs on the opposite side of the moon near the sub-Jovian point (0° W), causing a similar misalignment there.

The magnitude of the differential electron number flux onto Europa's surface falls sharply with increasing electron energy, reflecting the decaying high-energy tail of the electron energy distribution: the intensity $I(E)$ of

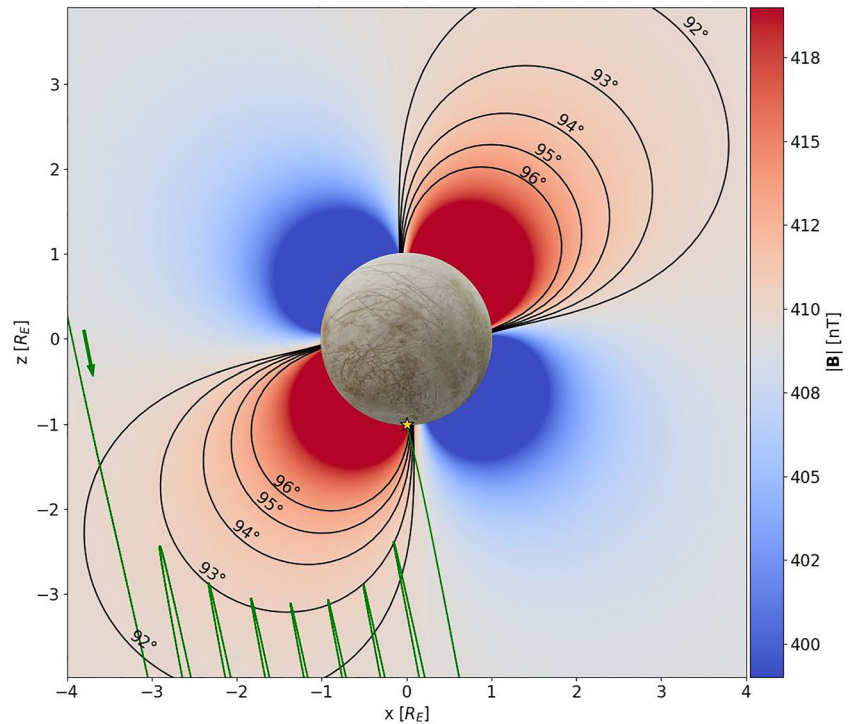


Figure 7. Trajectory of a 100 keV electron (green) which impacts Europa's south pole, projected into the $y = 0$ plane and calculated using a superposition of the Jovian background field and the moon's induced dipole (i.e., no plasma currents included). The trajectory is superimposed on a plot of the magnetic field magnitude $|\mathbf{B}|$, with red denoting regions where the induced field increases $|\mathbf{B}|$ and blue denoting regions where the induced field reduces $|\mathbf{B}|$, compared to the magnitude of the magnetospheric background field alone (white in the color bar). Also displayed are select isolines of the magnetic field strength (black). Each isoline represents the field strength necessary to locally mirror electrons with pitch angles at $z = -10 R_E$ (not shown) between 92° and 96° , as indicated with the black labels. The gold star indicates the impact point of the sample electron on Europa's surface.

the ambient electron flux falls by 5–6 orders of magnitude from 10 keV to 10 MeV (Paranicas et al., 2001). The influx of electrons with energies of 10 keV reaches approximately $10^7 \text{ cm}^{-2} \text{ s}^{-1} \text{ keV}^{-1}$ across much of the surface. The differential surface fluxes of 100 keV, 1 MeV, and 10 MeV electrons maximize at approximately $10^6 \text{ cm}^{-2} \text{ s}^{-1} \text{ keV}^{-1}$, $10^4 \text{ cm}^{-2} \text{ s}^{-1} \text{ keV}^{-1}$, and $10^2 \text{ cm}^{-2} \text{ s}^{-1} \text{ keV}^{-1}$, respectively.

Unlike the electron irradiation patterns determined with perfectly uniform fields (e.g., Dalton et al., 2013; Nordheim et al., 2018; Paranicas et al., 2001), the differential electron surface flux for $E \geq 100 \text{ keV}$ calculated with Europa's induced dipole included is not entirely confined to the two crescent-shaped maxima. When the magnetic equator is sweeping southward over the moon ($\lambda_{\text{III}} = 110^\circ$, Figure 5), the model reveals non-negligible flux contributions exterior to the crescents across the high-latitude southern hemisphere (e.g., light green region in the southern hemisphere of Figure 5c). The flux onto this south polar region is roughly an order of magnitude lower than the maximum value within the crescents. When the magnetic equator is sweeping northward over the moon ($\lambda_{\text{III}} = 284^\circ$), this flux contribution would appear outside of the crescent in the *northern* hemisphere. This additional, asymmetric irradiation is again caused by the induced dipole field. Since at $\lambda_{\text{III}} = 110^\circ \text{ W}$ the $B_{0,x}$ component of the background Jovian magnetic field is positive, Europa's induced magnetic moment is oriented in the $(-x)$ direction (see Table 1 and Equation 2 of Addison et al., 2021). The magnetic field magnitude near the moon in this configuration is shown in Figure 7. The induced field increases the magnetic field magnitude above Europa's southern, upstream hemisphere (red region at $x < 0$, $z < 0$ in Figure 7), since both the Jovian field and Europa's induced field have components pointing southward and toward downstream. Thus, the induced field creates a magnetic field gradient in the southern, upstream hemisphere which points toward Europa.

Although this gradient is only on the order of tens of nT over several R_E from Europa's surface, the mirror force it creates is sufficient to turn away electrons with pitch angles between ≈ 80 and 100° . Such electrons cannot

penetrate this region of enhanced magnetic field magnitude (red area in the lower left of Figure 7), and are mirrored back along their guiding magnetic field lines toward Jupiter's southern hemisphere. These particles will continue to bounce between their mirror points at high southern Jovian latitudes and their mirror points near Europa until they reach a region near the moon where the field magnitude is not sufficiently enhanced by the induced dipole to turn them away. Such a region exists in the southern, downstream hemisphere (blue area in the lower right of Figure 7).

An example of such an electron trajectory, projected into the $y = 0$ plane, is presented in Figure 7. Displayed is the trajectory of a 100 keV electron (green) which enters Europa's interaction region from upstream with its guiding center moving along a magnetic field line (indicated by the green arrow). In forward time, the electron first leaves Europa's interaction region from the southern face of the GENTOO domain at $z = -10 R_E$ (i.e., outside of the smaller domain displayed in Figure 7). The electron then completes a half-bounce in Jupiter's southern hemisphere, and returns to the interaction region displaced in the $+x$ direction by approximately $r_{az} = 0.35 R_E$. The electron's pitch angle upon re-entry into the GENTOO domain is between 92° and 93° . If the magnetic field near Europa were completely uniform, the electron would then proceed northward, exit the GENTOO simulation domain once again out of the $+z$ boundary, bounce, return to Europa's local environment, and so on. In this (hypothetical) uniform-field scenario, the electron would simply impact within one of the crescent-shaped enhancement regions on the moon's upstream hemisphere.

However, since the induced dipole field creates a magnetic field gradient pointing toward Europa in the southern, upstream region (lower left quadrant in Figure 7), the electron repeatedly "hits" an isoline of the magnetic field magnitude (labeled with " 93° ") where $|\mathbf{B}|$ is sufficiently strong to mirror the electron, and is turned back toward the south. In our example, this process occurs seven times, with the electron always completing a half-bounce in Jupiter's southern hemisphere, returning to Europa's interaction region, and being turned away by Europa's induced field. The mirror points of the electron near Europa therefore approximately follow the 93° isoline as the particle drifts in the $+x$ direction. Eventually the electron impacts the moon's south pole (gold star in Figure 7) close to the outer edge of the region with enhanced field magnitude. In Europa's southern, downstream hemisphere the induced field acts to *reduce* the magnetic field magnitude, rather than enhance it (blue region with $x > 0$ and $z < 0$ in Figure 7). Thus, electrons which re-impinge upon Europa's local environment from the south downstream of $x = 0$ will not be mirrored away, but will rather impact the moon.

A similar local mirroring effect on energetic particle trajectories near Europa has previously been proposed by Paranicas et al. (2000). These authors hypothesized that the moon's upstream magnetic pileup region mirrors particles with pitch angles between 60° and 120° , preventing them from approaching Europa's surface and causing a dropout in the pitch angle distribution measured near the moon by the Galileo EPD (see Figure 8 of that study). However, their proposed mechanism assumed a nearly global enhancement in the magnetic field magnitude around Europa caused by the magnetic field pileup. However, the enhancement associated with the induced field *alone* is much more localized (Figure 7). Thus, electrons mirroring near Europa are not able to completely avoid impacting the moon in this setup (as suggested for piled-up fields by Paranicas et al., 2000), but rather impact regions where the field locally drops in magnitude. Modification of energetic particle trajectories via local mirroring between a moon and Jupiter's magnetic poles has also been identified at Ganymede, where the moon's intrinsic field generates substantial field enhancements which can even mirror particles with pitch angles far from 90° (e.g., Truscott et al., 2011; Williams & Mauk, 1997).

This local mirroring effect acts to divert some of the incoming energetic electrons away from the southern crescent-shaped influx maximum and onto Europa's mid-to-high latitude southern hemisphere (Figures 5c, 5e, 5g). In other words, Europa's induced field allows for a small population of electrons to precipitate onto the surface outside of the crescent-shaped enhancement. Since the magnetic field gradients caused by the induced field are small, only electrons with pitch angles from approximately $80^\circ \leq \alpha \leq 100^\circ$ (about 10% of the ambient electrons, assuming an isotropic pitch angle distribution) can be diverted via this local mirroring effect. Thus, the differential surface influx outside of the southern crescent feature is approximately an order of magnitude lower than the maximum flux within the crescent. The mechanism illustrated in Figure 7 also explains why no substantial energetic electron flux is diverted onto Europa's *north* polar regions by the induced field at $\lambda_{III} = 110^\circ$ (when $B_{0,x}$ is positive). Above Europa's northern, upstream hemisphere ($x < 0$, $z > 0$) the induced field mainly points northward (opposite to $B_{0,z}$), and thus reduces the overall magnetic field strength (blue region in the upper left

quadrant of Figure 7). Therefore, no such mirroring process can divert electrons away from the upstream region and cause them to impinge outside of the northern crescent at this system III longitude.

The right column of Figure 5 (Figures 5b, 5d, 5f, and 5h) displays the differential number flux onto the surface of 10 keV, 100 keV, 1 MeV, and 10 MeV electrons calculated using the perturbed electromagnetic fields from AIKEF, that is, with plasma interaction currents included. The alterations to the energetic electron surface flux maps imposed by the field line draping are less prominent than for energetic ions (Addison et al., 2021; Nordheim et al., 2022). The two crescent-shaped flux enhancements on Europa's upstream hemisphere, as well as the southern hemisphere irradiation above $E = 100$ keV, remain the dominant non-uniformities in the influx patterns when the field line draping is considered as well. The similarity of the electron differential number flux patterns between the two model setups (with/without plasma currents) demonstrates that the bounce motion of electrons, rather than the perturbation to the local magnetic field by plasma currents, is the dominant mechanism for shaping energetic electron influx patterns. Observations suggest that upstream flow velocities as low as 65 km/s may occur near Europa's orbit (Bagenal & Dols, 2020). In such a scenario, the electromagnetic field perturbations and any associated protection of the moon's surface would be even weaker than shown in Figure 5 (see also Neubauer, 1998). Thus, the influx patterns with and without draped magnetospheric fields would be even more similar than suggested by our results from Figure 5.

While the draping of the magnetic field lines does not strongly change the macroscopic electron surface flux pattern, it still generates a clearly-discernible redistribution of electron impacts. For 100 keV electrons, the draping increases the latitudinal extension of the downstream region which is inaccessible to electrons (see, e.g., Figure 5c vs. Figure 5d). Since the field lines are wrapped around Europa's upstream hemisphere (see Figure 4a), electrons which travel along those lines are diverted toward upstream before they impact. Thus, even when the "segments" of these field lines far north and south of Europa have already reached the downstream hemisphere, they are still depositing their electron content onto the upstream hemisphere. Thus, the field line draping partially provides enhanced shielding of the downstream hemisphere between 60°S and 60°N latitude. The magnetic pileup also generates enhanced field gradients above Europa's upstream hemisphere, pointing toward the moon. These gradients can repeatedly mirror incoming electrons and divert them away from the moon's equatorial trailing hemisphere (analogous to Figure 7). Such a mechanism has been proposed to explain energetic electron dropouts observed by the Galileo EPD during the E4 and E15 flybys of Europa (Paranicas et al., 2000). This mirroring by the upstream pileup region reduces the electron number flux onto the upstream hemisphere between 30°N and 30°S latitude by a factor of approximately three (e.g., orange region around the equator in Figure 5b and dark green region around the equator in Figure 5d).

At the highest energies considered ($E = 1\text{--}10$ MeV), the electron gyroradii begin to approach 10% of Europa's radius. Above the polar regions, the draping creates an extended region where the field lines are nearly tangential to the surface. This extends the path length along which the electrons traveling along the field lines are within one gyroradius of the surface. Thus, some of these electrons impact the moon at high latitudes, causing nonzero flux onto the polar regions (e.g., black polar regions in Figure 5h).

The electron number flux maps calculated when Europa is located at the Jovian magnetic equator, but the equator is sweeping *northward* over the moon ($\lambda_{\text{III}} = 284^\circ$), are given in Appendix A for draped fields (Figure A1). In this configuration, $B_{0,x}$ is negative, and thus the background magnetic field is tilted by $\approx 10^\circ$ toward *upstream*. The electron flux maps in this case are qualitatively and quantitatively similar to those described in this section for $\lambda_{\text{III}} = 110^\circ$; however the influx patterns are flipped across Europa's equator. The mechanisms determining the shape of the surface influx maps are the same as described in this section for $\lambda_{\text{III}} = 110^\circ$, and we therefore refrain from a detailed description of this case.

3.2.2. Europa Located at Maximum Distance Above the Magnetic Equator ($\lambda_{\text{III}} = 191^\circ$)

Maps of the differential electron number flux onto Europa's surface when the moon is located at its maximum elongation *above* the Jovian magnetic equator are displayed in Figure 8. The layout of the figure is the same as Figure 5: the left column displays the surface influx patterns at various electron energies calculated with a superposition of the Jovian background field and Europa's induced field (i.e., no plasma currents), and the right column displays the flux maps calculated with field line draping included. When Europa is at its maximum distance above the planetary magnetic equator, $B_{0,x}$ is negligible, while $B_{0,y}$ is negative and roughly half the magnitude of the southward field component $B_{0,z}$ (see Table 1). The Jovian background field is therefore rotated away from

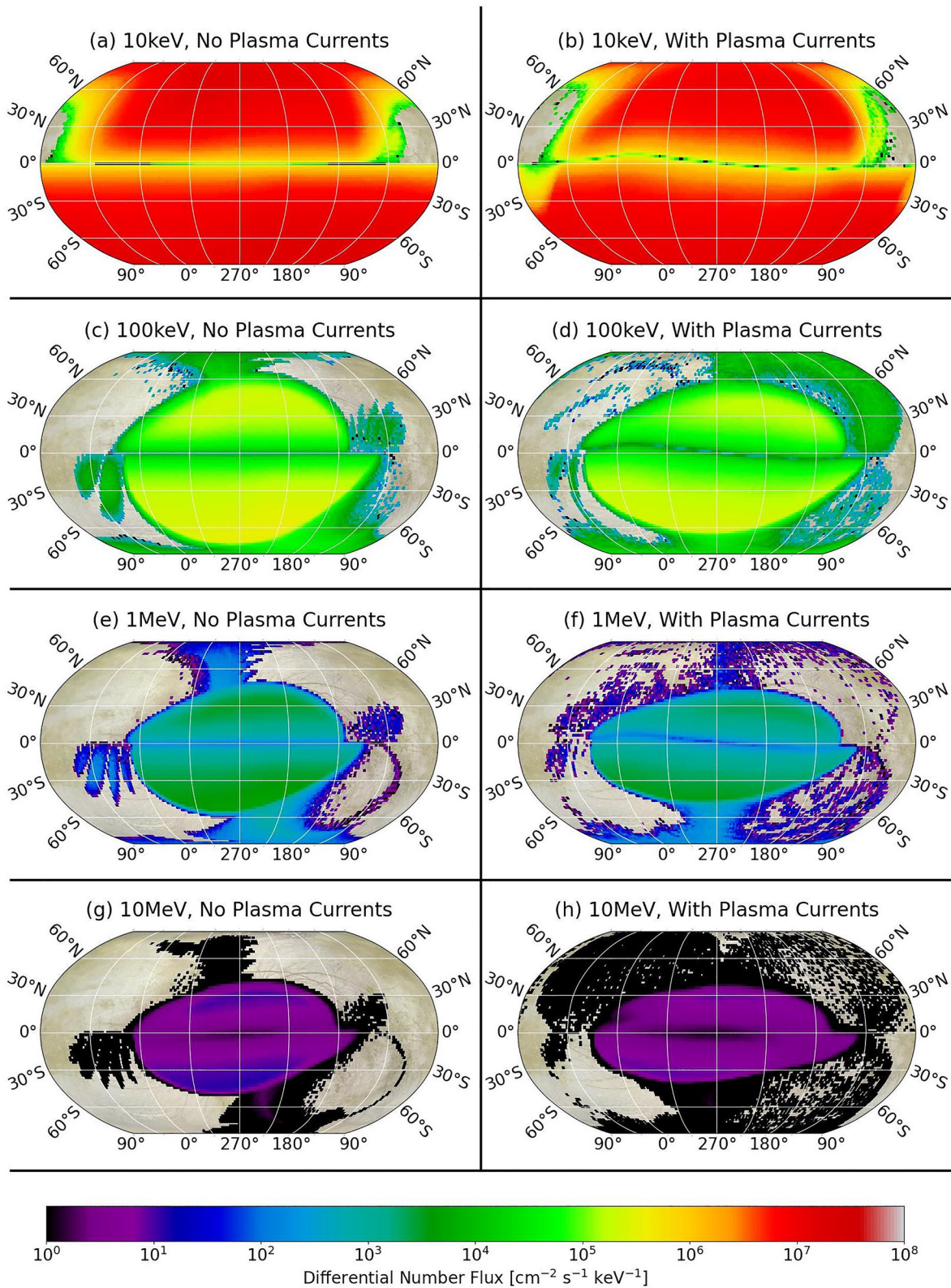


Figure 8. Differential energetic electron number fluxes onto Europa's surface while the moon is located at its maximum distance *above* the Jovian magnetic equator ($\lambda_{III} = 191^\circ$). The layout of the plots is the same as in Figure 5.

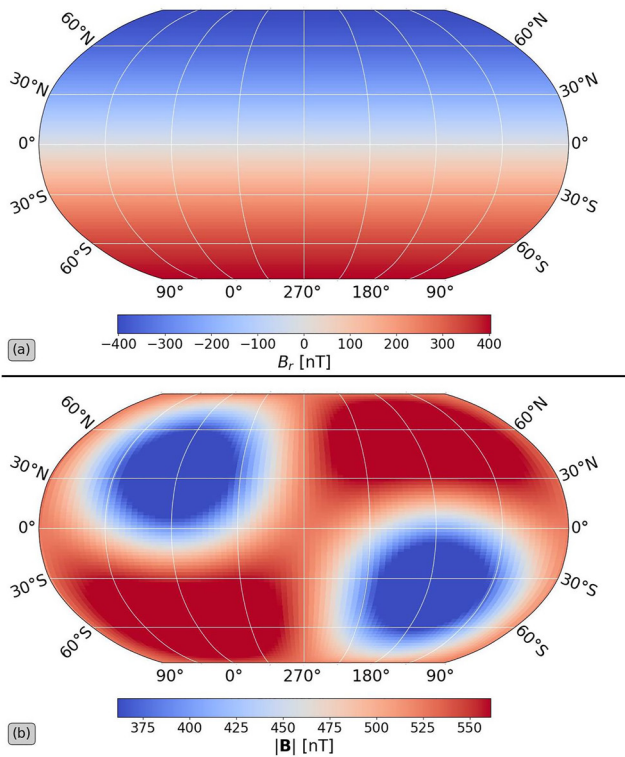


Figure 9. Magnetic field at Europa's surface (i.e., at $r = \sqrt{x^2 + y^2 + z^2} = R_E$), resulting from the superposition of the ambient magnetospheric field \mathbf{B}_0 and Europa's induced field when the moon is located at its maximum distance above the Jovian magnetic equator. Panel (a) displays the radial component of the magnetic field relative to Europa's center B_r , while panel (b) shows the magnitude of the magnetic field $|\mathbf{B}|$.

Jupiter by approximately 30° around the x axis. In this case, the magnitude of Europa's induced magnetic moment is roughly three times higher than at the planetary magnetic equator, and the moment vector points toward Jupiter (i.e., in $+y$ direction, opposite to $B_{0,y}$).

When Europa is located far above the Jovian magnetic equator, and plasma interaction currents are not considered, 10 keV electrons can uniformly reach nearly every region of the moon's surface, with the exception of the equator and part of the northern, downstream hemisphere (Figure 8a). The differential number flux of 10 keV electrons reaches $10^7 \text{ cm}^{-2} \text{ s}^{-1} \text{ keV}^{-1}$ across much of the moon's surface, similar to the differential flux of 10 keV electrons when Europa is located at the magnetic equator (Figure 5a). The large bounce displacements of these electrons (up to $r_{az} = 2 R_E$, see Figure 2) allow them access to nearly every region on the moon's upstream hemisphere and much of the downstream surface. The flux of 10 keV electrons onto the downstream hemisphere is asymmetric between northern and southern latitudes. Namely, the influx onto the northern, downstream hemisphere is several orders of magnitude lower than onto the southern downstream hemisphere, culminating in a void region (zero flux) north of Europa's equator between 45° and 135° west longitude (Figure 8a).

Since the moon is positioned far above the magnetic equator in this model setup, electrons which bounce north of Europa (i.e., with pitch angles $\alpha_0 > 90^\circ$ when exiting Europa's local domain) have a much shorter distance to travel to their mirror points than electrons which bounce south of the moon, that is, $\alpha_0 < 90^\circ$ (see also the blue field line in Figure 1). Thus, electrons which bounce in Jupiter's northern hemisphere have much smaller azimuthal displacements than those which bounce in the planet's southern hemisphere (Figure 2b). For example, a 10 keV electron with a pitch angle near Europa of $\alpha_0 = 30^\circ$ (i.e., which bounces in the south) has an azimuthal displacement of $r_{az} \approx 2 R_E$, that is, an entire European diameter (solid blue line in Figure 2b). Its "counterpart" 10 keV electron which bounces in the north and has the same speed perpendicular to the magnetic field (i.e., $\alpha_0 = 150^\circ$),

only displaces by $r_{az} \approx 1 R_E$ during a bounce period (dashed blue line in Figure 2b). As such, a flux tube which impinges upon Europa depletes its population of energetic electrons onto the moon's northern hemisphere faster than onto the southern hemisphere. Thus, the influx onto Europa's downstream northern hemisphere falls off faster with distance along the x axis than it does in the southern hemisphere, causing the north-south asymmetry in electron flux onto the downstream hemisphere seen in Figure 8a.

Similar to when Europa is located at the Jovian magnetic equator (see Section 3.2.1), the influx of 10 keV electrons onto the moon's surface at its maximum elongation above the magnetic equator is interrupted near the equator by a belt-like region of reduced flux (Figure 8a). Within this equatorial reduction belt the surface number flux drops by up to 8 orders of magnitude, as the gyrating electrons impact the moon at higher latitudes and are prevented from reaching the equator. At Europa's maximum distance above the Jovian magnetic equator, the induced dipole moment points in the $+y$ direction (toward Jupiter), and severely weakens the inducing component of the ambient field at the moon's sub-Jovian and anti-Jovian apices. This is illustrated in Figure 9a, which displays a map of the radial component of the field (i.e., the component pointing toward or away from Europa's center) at the moon's surface. Under the assumption of a highly-conducting ocean (see Equation 2 in Addison et al., 2021), the moon's induced field cancels out the inducing component of the Jovian field ($B_{0,x}, B_{0,y}, 0$) at Europa's geographic equator (white in Figure 9a). The induced field therefore causes the magnetic field to be (nearly) tangent to the surface at each point along the geographic equator, thereby "pinning" the reduction belt to this region (see also Section 3.2.1).

When electron energies increase ($E \geq 100 \text{ keV}$), the reduced azimuthal displacements r_{az} of the bouncing electrons largely restrict their influx to the low-latitude upstream hemisphere, poles, and sub-/anti-Jovian flanks of Europa, where the drifting flux tubes deposit their electron content before being depleted (Figures 8c, 8e, and 8g).

The majority of the influx for electrons with $E \geq 100$ keV again occurs in two crescent-shaped regions on the upstream hemisphere. The azimuthal displacements of electrons which bounce in Jupiter's southern hemisphere are $1 R_E$ (at 10 keV) to $0.1 R_E$ (at 10 MeV) greater than those of electrons which bounce in Jupiter's northern hemisphere (see Figure 2). Therefore, electrons which bounce in the southern hemisphere can reach surface regions which are much farther downstream. Thus, the southern crescent extends much farther toward south polar latitudes (e.g., to 80° south at $E = 100$ keV) than the northern crescent (e.g., to 60° north at $E = 100$ keV). In other words, this dichotomy in the shapes of the northern and southern crescent features is purely a result of the asymmetric azimuthal displacements between electrons which bounce in Jupiter's northern and southern hemispheres. As the electron energy increases, the azimuthal displacements r_{az} drop further and the circular edges of the crescents move toward the equator. However, the southern crescent persistently extends approximately 20° higher in latitude than the northern crescent (e.g., Figures 8c and 8e). The larger azimuthal displacements of electrons which bounce in Jupiter's southern hemisphere also slightly broaden the longitudinal extent of the southern crescent feature. At all energies considered, the northern and southern crescents are interrupted at low latitudes by the equatorial reduction belt.

Since Europa's induced magnetic moment points in the $+y$ direction (i.e., toward Jupiter), the "shamrock leaf" signatures in the magnetic field magnitude seen in Figure 7 (when the moon is located at the magnetic equator) are now rotated by 90° clockwise around the z axis. Figure 9b displays the magnetic field magnitude at Europa's surface resulting from the superposition of the Jovian background field \mathbf{B}_0 and the moon's induced dipole field. The regions where the induced field enhances the field strength are now located above the southern, sub-Jovian hemisphere (red region in the lower left of Figure 9) and the northern, anti-Jovian hemisphere (red region in the upper right). Both of these enhancement regions locally extend into the upstream hemisphere. Some electrons approaching Europa from upstream are mirrored in the northern enhancement region (similar to the mechanism displayed in Figure 7) and are prevented from impacting within the northern crescent flux feature (e.g., yellow in Figure 8c). Instead, these electrons impact at high latitudes near Europa's north pole (e.g., green region above the northern crescent in Figure 8c). Similarly, electrons which approach Europa from the south may be mirrored by the magnetic field enhancement above the moon's southern, sub-Jovian hemisphere and impact near the south pole (e.g., blue region *below* the southern crescent in Figure 8e, and black region below the southern crescent in Figure 8g).

Similar to when Europa is located at the Jovian magnetic equator, the quantitative values of the differential surface number flux fall with increasing energy, following the monotonic decrease of the ambient electron flux distribution with increasing energy (e.g., Paranicas et al., 2001). The differential number flux of 10 keV electrons reaches a maximum value of approximately $1 \times 10^7 \text{ cm}^{-2}\text{s}^{-1} \text{ keV}^{-1}$ across most of the moon's surface (Figure 8a). At higher electron energies, the fluxes maximize within the upstream crescents, with peak values near $3 \times 10^5 \text{ cm}^{-2}\text{s}^{-1} \text{ keV}^{-1}$ at $E = 100$ keV (Figure 8c), $1 \times 10^4 \text{ cm}^{-2}\text{s}^{-1} \text{ keV}^{-1}$ at $E = 1$ MeV (Figure 8e), and $3 \times 10^1 \text{ cm}^{-2}\text{s}^{-1} \text{ keV}^{-1}$ at $E = 10$ MeV (Figure 8g). The maximum differential fluxes at all energies are similar to those calculated at the Jovian magnetic equator.

As can be seen in the right column of Figure 8, the inclusion of magnetic field line draping results in a subtle redistribution of electron surface flux, compared to when no plasma currents are considered. Draping of the magnetic field lines around the moon partially diverts impinging electrons away from Europa's downstream hemisphere. This extends the region on the moon's downstream surface which is completely devoid of 10 keV electron bombardment from latitudes of approximately 45° north to 60° north (Figure 8b). In draped fields, the downstream depletion in 10 keV electron influx maintains the north-south asymmetry seen without plasma currents (Figure 8a). This asymmetry again stems from the larger azimuthal displacements of electrons which bounce in Jupiter's southern hemisphere compared to those which bounce in the northern hemisphere. At all energies, the draping displaces the low-latitude flux depletion belt away from the geographic equator, shifting it slightly northward in Europa's sub-Jovian hemisphere and slightly southward in the moon's anti-Jovian hemisphere. This effect is rather subtle: at all longitudes the depletion belt remains within a 10° latitude of the geographic equator.

Within the upstream pileup region, the magnetic field strength is enhanced by over 100 nT, that is, approximately 22% of $|\mathbf{B}_0|$ (Figure 4h). Using conservation of the first adiabatic invariant, we find that this increase in field magnitude is sufficiently strong to mirror particles with pitch angles upon entering Europa's perturbed field region between $\alpha_0 = 55^\circ$ and $\alpha_0 = 125^\circ$. Electrons which are mirrored away from the upstream hemisphere by the pileup region may instead impact further downstream. This mirroring redistributes some of the electron influx,

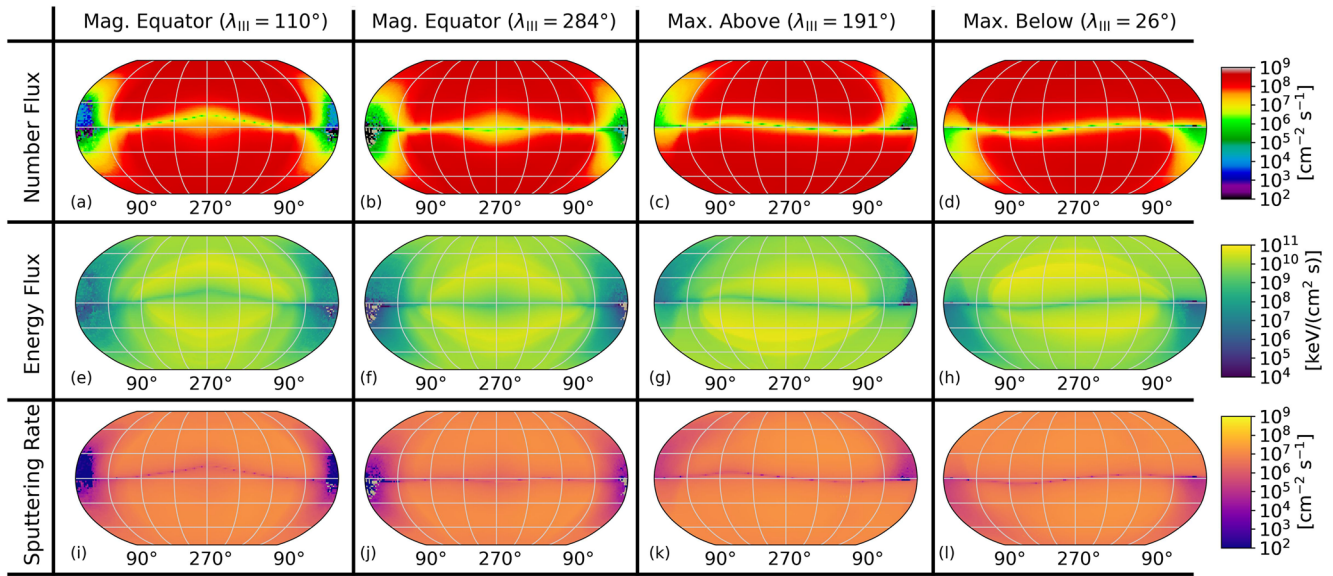


Figure 10. Number influxes (top row, panels a–d), energy influxes (middle row, panels e–h), and O₂ sputtering rates (bottom row, panels i–l) at Europa's surface for all four system III longitudes described in Table 1. All quantities are integrated over the energy range from 5 keV to 10 MeV, and are calculated with the draped fields from the AIKEF model (Figure 4). The first (panels a, e, and i) and second (panels b, f, j) columns display quantities calculated when Europa is located at the Jovian magnetic equator, and the equator is sweeping southward ($\lambda_{III} = 110^\circ$) or northward ($\lambda_{III} = 284^\circ$) across the moon, respectively. The third (panels c, g, and k) and fourth (panels d, h, and l) columns present quantities determined when Europa is at its maximum elongation *above* or *below* the planetary magnetic equator, respectively. Number fluxes and sputtering rates are shown in units of $\text{cm}^{-2} \text{s}^{-1}$, while energy fluxes are shown in units of $\text{keV cm}^{-2} \text{s}^{-1}$. The sputtering rates shown are calculated with the model of Teolis et al. (2017), taking into account surface incidence angles onto a perfect sphere calculated with GENTOO. The grid lines are spaced by 45° in longitude and 30° in latitude, identical to the layout of the surface maps shown in Figures 5, 8, A1, and B1.

“smearing” out the edges of the crescent features for electron energies $E \geq 100$ keV (e.g., green region in the upper right of Figure 8d). The energetic electron influx is therefore less contained within the crescents when the magnetic field draping is included. The redistribution of electron impacts away from the crescents reduces the differential influx within these two features (compared to when plasma currents are not considered) by a factor of roughly two at all energies $E \geq 100$ keV.

Electron number flux maps calculated while Europa is at its maximum elongation *below* the Jovian magnetic equator (i.e., $\lambda_{III} = 26^\circ$) are presented in Appendix B for draped fields. In this case, $B_{0,y}$ is positive, that is, the magnetic field is tilted toward Jupiter. The influx maps in this case are qualitatively very similar to those displayed in Figure 8, but the patterns are flipped across the moon's geographic equator. Since the physical processes generating the influx features are the same as those described in this section, we omit a detailed discussion of those maps.

3.3. Energy-Integrated Fluxes and Sputtering Rates

Figure 10 displays maps of the energy-integrated number influxes (Figures 10a–10d), energy influxes (Figures 10e–10h), and O₂ sputtering rates (Figures 10i–10l) from Europa's surface at the four system III longitudes described in Section 2, calculated with the draped fields from AIKEF (Figure 4). The first column (Figures 10a, 10e, and 10i) presents these quantities calculated when Europa is located at the Jovian magnetic equator, and the equator is sweeping *southward* over the moon ($\lambda_{III} = 110^\circ$). The second column (Figures 10b, 10f, and 10j) displays results from when the moon is located at the planetary magnetic equator and the equator is sweeping *northward* over the moon ($\lambda_{III} = 284^\circ$). The third (Figures 10c, 10g, and 10k) and fourth (Figures 10d, 10h, and 10l) columns display maps of the energy-integrated quantities determined when Europa is located at its maximum elongation *above* ($\lambda_{III} = 191^\circ$) or *below* ($\lambda_{III} = 26^\circ$) the Jovian magnetic equator, respectively. All quantities are integrated across the full energy range considered in this study: 5 keV–10 MeV. Above 10 MeV the intensity of the energetic electron flux observed outside of Europa's interaction region is too low (more than eight orders of magnitude lower than at 10 keV) to notably contribute to surface energy deposition and sputtering (Paranicas et al., 2001).

The number flux patterns of energetic electrons onto Europa's surface at all four system III longitudes (Figures 10a–10d) are dominated by the contributions from electrons at the lower end of the analyzed energy range ($5 \text{ keV} \leq E \leq 50 \text{ keV}$), since these electrons are several orders of magnitude more abundant in the upstream plasma than the higher-energy electrons (Paranicas et al., 2001, 2009). Thus, the energy-integrated number influxes are uniform across much of Europa's upstream surface (see panel b in Figures 5, 8, A1, and B1). An exception to this quasi-uniform influx pattern occurs in the narrow reduction band near the geographic equator (yellow-green in Figures 10a–10d), where the number flux is 2–3 orders of magnitude lower than the influx onto the rest of the upstream hemisphere and the polar regions (red). The crescent-shaped flux enhancements seen in the number flux patterns at energies $E \geq 100 \text{ keV}$ (see, e.g., panel d in Figures 5, 8, A1, and B1) are no longer discernible in the energy-integrated maps (first row of Figure 10), since these features are superposed on the 2–3 orders of magnitude more intense influx patterns of 5–10 keV electrons.

The energetic electron number flux onto the mid-to-low latitude downstream hemisphere is reduced compared to the high-flux regions on the upstream hemisphere, as only 5–10 keV electrons with pitch angles far from 90° can reach these locations (Figures 5, 8, A1, and B1). When the moon is located at the Jovian magnetic equator (Figures 10a and 10b), the number flux onto the downstream hemisphere at 45° northern or southern latitude has fallen by approximately two orders of magnitude compared to the poles. At the downstream equator, the difference to the polar influx grows to 5–6 orders of magnitude. When Europa is located at its maximum distance above the planetary magnetic equator (Figure 10c), the azimuthal displacements of electrons which bounce in Jupiter's southern hemisphere are enhanced compared to when the moon is located at the magnetic equator (Figure 2). These increased azimuthal displacements allow more electrons to reach the mid-to-low latitude, southern downstream hemisphere. The reverse is true when Europa is located below the magnetic equator (Figure 10d), and particles which bounce in Jupiter's northern hemisphere have larger bounce displacements. In this case, more energetic electrons can reach the mid-to-low latitude *northern* hemisphere. Thus, the region near Europa's downstream apex (but only on *one* side of the equator) experiences similar number influxes to the polar regions when the moon is far from the planetary magnetic equator.

The energy flux onto Europa's surface maximizes within the crescent-shaped regions in the moon's northern and southern upstream hemispheres (bright yellow in Figures 10e–10h). The energy flux within these two regions peaks at approximately $5 \times 10^{10} \text{ keV cm}^{-2} \text{ s}^{-1}$, an order of magnitude higher than anywhere on the upstream hemisphere outside of the crescents, and 4–5 orders of magnitude higher than at the downstream apex. Thus, throughout a synodic rotation of Jupiter, energetic electrons with energies $E \leq 10 \text{ MeV}$ deposit far more energy onto Europa's upstream hemisphere than its downstream hemisphere.

The crescent features in the energy influx patterns slightly “wobble” northward and southward as the Jovian magnetic equator sweeps back and forth across Europa (Figures 10e–10h). This change in morphology is caused by the different orientations of the Jovian background field and the moon's induced magnetic moment, as well as the asymmetric azimuthal displacements of electrons which bounce in Jupiter's northern or southern hemispheres (see Section 3.2.2). For example, at maximum elongation above the Jovian magnetic equator, the southern crescent extends approximately 30° in latitude farther poleward than the northern crescent, and vice versa when the moon is located below the Jovian magnetic equator (Figures 10g and 10h). The crescent-shaped maxima in energy influx are, however, always confined latitudinally between roughly 60° north and south, and longitudinally between (approximately) the sub- and anti-Jovian apices. Along Europa's equator, the crescents are separated by a belt-like reduction that similarly appears in the number flux patterns, where the energy flux drops by approximately four orders of magnitude.

The crescent-shaped regions of maximum energy influx visible in Figures 10e–10h appear in a (qualitatively) similar way in the maps of electron energy surface flux calculated by Dalton et al. (2013) using a particle-tracing code and a uniform, southward magnetic field (see Figure 5 of that paper). These authors found these crescent features to be located near 45° northern and southern latitudes. Similar to our results, Dalton et al. (2013) found the energy deposition by energetic electrons onto the upstream hemisphere to decrease toward the equator. However, these authors predicted nearly *zero* electron energy flux onto the downstream hemisphere between approximately 15° – 165° west longitude, as well as the polar regions above 60° north and 60° south latitude. Earlier work by Paranicas et al. (2001) using a guiding-center approach with uniform electromagnetic fields near Europa also predicted zero energy flux onto the poles and the downstream hemisphere. However, our results show that the polar downstream regions also receive substantial levels of electron irradiation. Indeed, the energy

flux onto Europa's polar caps in our model is only approximately one order of magnitude less than within the crescent-shaped maxima. Furthermore, as the moon makes its maximum excursions above (or below) the planetary magnetic equator, the energy flux onto the mid-to-low latitude southern (or northern) downstream hemisphere also reaches levels that are only an order of magnitude below the peak flux onto the upstream hemisphere (Figures 10g and 10h). Electrons at the lower end of the energy regime considered ($E \leq 10$ keV) experience sufficiently large azimuthal displacements during a bounce to reach the poles and mid-to-low latitude downstream surface before their flux tube is depleted.

The maximum energy flux onto Europa's surface when the moon is located at the planetary magnetic equator is located within the crescent features and is approximately 4.2×10^{10} keV cm⁻² s⁻¹ (Figures 10e and 10f). When the moon is located at maximum elongation above or below the planetary magnetic equator, the peak energy flux onto any surface point only slightly increases (by a factor of ≈ 1.4) to 5.8×10^{10} keV cm⁻² s⁻¹. The energy flux maxima are approximately consistent with the value of 3.5×10^{10} keV cm⁻² s⁻¹ predicted by Dalton et al. (2013) using a guiding center model, and over an order of magnitude higher than predicted in that study with a particle-tracing model in uniform fields (4.4×10^9 keV cm⁻² s⁻¹).

The O₂ sputtering rate patterns from energetic electron impacts are displayed in Figure 10i–10l. The sputtering rates shown are calculated with the sputtering yield model of Teolis et al. (2017), scaled with a factor of 0.3 to match experimental data (see Section 2.3 and Figure 3). The surface temperatures used to calculate the sputtering yields are from Figure 3 of Addison et al. (2022), which captures the average surface temperature as Europa completes an entire orbit around Jupiter.

Since the O₂ sputtering yields from electron impacts fall by over an order of magnitude from 10 keV to 10 MeV (Figure 3), the contribution of higher-energy electrons ($E \geq 100$ keV) to the sputtering rates is even weaker than for the number fluxes. The spatial distributions of the sputtering rates at all four system III longitudes therefore largely resemble the patterns seen in the differential number fluxes at $E \leq 10$ keV (Figures 5a and 8a, A1a, and B1a). Hence, the sputtering rates are quasi-uniformly high ($\approx 10^7$ cm⁻² s⁻¹) across much of the moon's upstream hemisphere, polar caps, and sub-/anti-Jovian flanks (Figures 10i–10l). The sputtering rates fall by 2–3 orders of magnitude within the narrow, near-equatorial depletion belt compared to the rest of the upstream hemisphere. Sputtering by energetic electrons is also reduced by 5–6 orders of magnitude on the mid-to-low latitude downstream hemisphere. At maximum elongation above/below the Jovian magnetic equator, the downstream reduction in electron sputtering becomes asymmetric between Europa's northern and southern hemispheres, indicative of the asymmetries in electron influx (see right columns of Figures 5, 8, A1, and B1).

Figure 11 displays the number fluxes, energy fluxes, and sputtering rates from Figure 10 integrated across Europa's entire surface. The resultant quantities are the total precipitation rate of energetic electrons onto Europa's surface (in electrons/second, Figure 11a), the total power deposited by energetic electrons (Figure 11b), and the total production rate of O₂ from the moon's surface through energetic electron impacts (in O₂ molecules/second, Figure 11c). The colors of the bars indicate different system III longitudes of the moon, and correspond to those of the respective magnetic field lines shown in Figure 1.

Figure 11a reveals that the electron precipitation rate onto Europa's surface shows only subtle variations as a function of system III longitude. The precipitation rate is similar (within 3%) for both cases where Europa is located at the Jovian magnetic equator (red and blue bars), and is slightly higher (by approximately 25%) when the moon is far from the planetary magnetic equator (green and orange bars). The upstream thermal plasma density is reduced by a factor of five at the moon's maximum distance from the Jovian magnetic equator compared to the density at the magnetic equator (Table 1). Therefore, the “strength” of Europa's plasma interaction (Simon et al., 2021) and the magnitude of the electromagnetic field perturbations is weaker, with a diminished draping signature and reduced extent of the upstream pileup region (Figure 4). Europa's induced magnetic moment is strongest at large distances from the planetary magnetic equator. However, as described in Section 3.2, the induced dipole field merely *redistributes* the electron flux onto the surface, but does not cause a substantial number of electrons to miss the moon entirely (e.g., Figure 7). Thus, the presence of a strong induced dipole field does not substantially reduce the precipitation rate integrated across Europa's entire surface. Any reduction in the accessibility of the surface to energetic electrons due to the field perturbations results mainly from the draping, and not Europa's induced field. However, due to the weak plasma interaction far from the center of the Jovian plasma sheet, the draped field lines do not substantially deflect the impinging energetic electron population away from the moon's surface. Thus, the integrated electron precipitation rate at large distances to the Jovian magnetic equator is

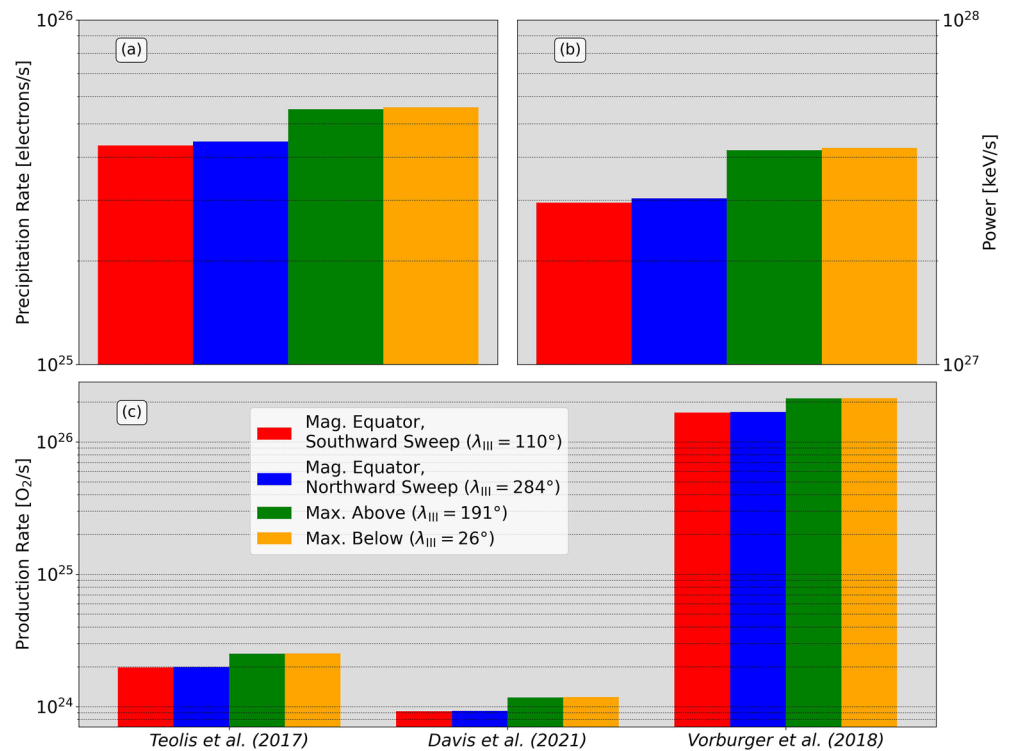


Figure 11. Total precipitation rate (in electrons per second) onto Europa's surface (panel a), total amount of energy deposited into the surface per second (i.e., power) by energetic electrons (panel b), and total production rate of O_2 molecules from the surface via energetic electron impacts (panel c). The quantities displayed are from electron impacts with energies $5 \text{ keV} \leq E \leq 10 \text{ MeV}$. The differently colored bars represent different system III longitudes of the moon, as given in Table 1. Each bar is colored the same as the associated magnetic field line in Figure 1. In panel (c), O_2 production rates as a function of system III longitude, calculated with the sputtering yield models of Teolis et al. (2017), Davis et al. (2021), and Vorburger and Wurz (2018) are shown in the left, center, and rightmost blocks, respectively.

slightly enhanced compared to when the moon is located at the magnetic equator. However, the subtle differences between the two cases suggest that the precipitation rates calculated for, for example, the magnetic equator case, are—to a good approximation—representative of the rates at any point during a synodic rotation.

We remind the reader of the uncertainty in the number density of the ambient thermal plasma upstream of Europa, and how it varies with system III longitude (see also Section 2.1). Plasma data from the Galileo PLS instrument (Bagenal & Delamere, 2011) suggest a lower density of the upstream thermal plasma at the center of Jupiter's plasma sheet ($n_{p,0} = 50 \text{ cm}^{-3}$) and a larger plasma sheet scale height ($H = 1.8R_J$) than the values measured by the Galileo PWS, which are used as input for our model ($n_{p,0} = 200 \text{ cm}^{-3}$ and $H = 0.9R_J$, respectively, see Roth et al., 2014). Inserting the values of $n_{p,0}$ and H from the Galileo PLS into the Gaussian profile (Equation 4 of Bagenal & Delamere, 2011) would suggest that the upstream plasma density at Europa only varies by 20% over the course of a synodic rotation, rather than the factor of 5 suggested by the PWS. In this case, the already weak difference in energetic electron influx at different distances to the magnetic equator would be further attenuated. For our study we have also chosen to use the same ambient electron energy distribution $I(E)$ at all system III longitudes, not taking into account any possible variability in the distribution with magnetic latitude (Section 2.2). Variations in the electron bombardment with system III longitude are thus solely due to changes in the azimuthal displacements r_{az} of particles bouncing at different magnetic latitudes, as well as the variation in the ambient electromagnetic field conditions (Figure 4).

A similarly subtle dependence on system III longitude is seen in the total power deposited by energetic electrons (Figure 11b). At maximum elongation above or below the Jovian magnetic equator (green and orange bars), the power deposited by energetic electrons is about $4.2 \times 10^{27} \text{ keV/s}$ (673 GW). When the moon is located at the magnetic equator (red and blue bars), the power deposited is approximately $3.0 \times 10^{27} \text{ keV/s}$ (480 GW), that is, roughly 29% lower. The increased strength of the magnetospheric field perturbations when Europa is located in

the densest region of the Jovian plasma sheet is therefore able to partially protect the surface from electron power deposition, more so than when the moon is in the dilute plasma above or below the center of the sheet. In contrast, the averaged local energy influx of 6.2×10^{10} keV/s predicted by Cooper et al. (2001) yields a surface-integrated power deposition of approximately 3,000 GW, roughly an order of magnitude higher than calculated here. This difference illustrates the need to consider the full dynamics of energetic electrons, including gyration, bounce motion, and the effect of the field perturbations (from both Europa's inductive response and its plasma interaction) on the particle trajectories.

The total production rate of neutral O₂ from energetic electron sputtering of Europa's surface is shown in Figure 11c for the sputtering yield models of Teolis et al. (2017), Davis et al. (2021), as well as Vorburget and Wurz (2018). The energy dependence of the sputtering yields calculated by Teolis et al. (2017), with a scale factor of 0.3 applied, is shown in Figure 3, while the yield model of Davis et al. (2021) is identical, except scaled by a factor of 0.14 rather than 0.3. At any given surface location, the sputtering rates calculated with the model of Davis et al. (2021) are therefore 47% those calculated with the model of Teolis et al. (2017). For this reason, Figure 10 does not include a dedicated row of sputtering rate maps for the yield model of Davis et al. (2021). The same downscaling factor of 0.47 is applied when converting the total production rates obtained with the sputtering yield model of Teolis et al. (2017) into those corresponding to the yield model of Davis et al. (2021). The sputtering yield model of Vorburget and Wurz (2018) suggests a constant yield of $Y = 2$ across the entire energy range considered in this study, and the production rates calculated with their model are shown in the rightmost block of Figure 11c. Since the sputtering yield model of Vorburget and Wurz (2018) merely multiplies the flux deposited by any electron with the *same*, constant scalar (regardless of energy or incidence angle), we do not present maps of the sputtering rates calculated with this yield model. Such maps would be qualitatively identical to the number influx maps (first row of Figure 10).

Using the constant O₂ sputtering yield from Vorburget and Wurz (2018), we find an energetic electron O₂ production rate that ranges from 8.65×10^{25} s⁻¹ to 1.10×10^{26} s⁻¹ at different system III longitudes (rightmost block of Figure 11c). By assuming that the undisturbed ambient energetic electron distribution uniformly reaches every location on Europa's surface, Vorburget and Wurz (2018) predict an O₂ production rate by energetic electrons of 9.18×10^{25} s⁻¹. This value is roughly in the middle of the range provided by our model with the constant O₂ sputtering yields of Vorburget and Wurz (2018). However, as we have shown, the *spatial distribution* of the sputtering rate by electrons is non-uniform across Europa's surface (see Figures 10i–10l). Europa's mid-to-low latitude downstream hemisphere is accessible only to electrons from the lower end of the energy regime considered (5–10 keV) and a narrow range of pitch angles. Furthermore, a narrow region near the geographic equator consistently experiences O₂ sputtering rates which are several orders of magnitude lower than, for example, those in the mid-latitude upstream hemisphere. Thus, it is imperative to consider a complete model of electron dynamics when mapping the spatial distribution of O₂ sputtering at Europa.

Using the sputtering yield model of Teolis et al. (2017), we calculate O₂ production rates which range between $(1.98\text{--}2.00) \times 10^{24}$ s⁻¹ at the Jovian magnetic equator and $(2.52\text{--}2.53) \times 10^{24}$ s⁻¹ at maximum distance above or below the magnetic equator. In other words, these production rates exhibit a similarly subtle dependence on system III longitude as the precipitation rates (Figure 11a). The production rates that we obtain with the sputtering yield model of Davis et al. (2021) therefore range from 9.31×10^{23} s⁻¹ (at the magnetic equator) to 1.19×10^{24} s⁻¹ (at maximum distance below the magnetic equator).

Davis et al. (2021) also applied their model of sputtering yields to estimate the production rate of O₂ from Europa's surface by *thermal* and *energetic* magnetospheric electron impacts combined. By assuming that the ambient (thermal and energetic) electron population uniformly reaches every location on the moon's surface, these authors obtained a total O₂ production rate of $(1\text{--}2) \times 10^{26}$ s⁻¹. This estimate is 1–2 orders of magnitude higher than the O₂ production rate calculated from our approach for *energetic* electron sputtering alone (using the *yield* model from Davis et al., 2021). Therefore, in order for our calculated O₂ production rates from *energetic* electron impacts to be consistent with the rates suggested by Davis et al. (2021) for the *entire* range of electron energies at Europa (thermal and energetic combined), the thermal electrons would have to produce 10–100 times more O₂ per second than the energetic electrons alone do in our model.

However, Vorburget and Wurz (2018) used their yield model to demonstrate that the thermal electrons (in isolation) sputter a factor of four *less* O₂ from Europa's surface than energetic electrons. These authors estimated the production rate from thermal electron impacts alone to be 2.28×10^{25} s⁻¹. In order to obtain this estimate,

Vorburger and Wurz (2018) assumed that only 20% of the upstream thermal plasma can reach Europa's surface, while the rest of the thermal particles are deflected away from the moon by the field perturbations. Similar to Davis et al. (2021), the study of Vorburger and Wurz (2018) assumed that this reduced thermal electron influx uniformly reaches every location on Europa's surface. Combining the thermal electron production rate for O₂ from Vorburger and Wurz (2018) with our calculated production rates for energetic electrons (using the sputtering yield model of Davis et al., 2021) gives a total O₂ production rate from magnetospheric electron impacts of approximately $(2.36\text{--}2.39) \times 10^{25} \text{ s}^{-1}$. This O₂ production rate is about an order of magnitude lower than the estimated rate from Davis et al. (2021). Thus, the combination of our sputtering rates from energetic electrons with the rates from thermal electron impacts given by Vorburger and Wurz (2018) suggests that the production rates from Davis et al. (2021) are an overestimate by a factor of 10.

3.4. Relative Contributions of Ions and Electrons to Power Deposition and O₂ Production

In order to determine the average distribution of energetic particle influx, energy deposition, and O₂ sputtering from Europa's surface over a full synodic rotation of Jupiter, we now average the surface flux and sputtering rates from all four system III longitudes investigated in this study. Due to the demonstrated influence of the electromagnetic field perturbations on these quantities (see Sections 3.2.1 and 3.2.2), we consider only the cases which use the draped fields from AIKEF (Figure 10). Europa spends more time at positions far from the center of the Jovian plasma sheet than it does at the center of the plasma sheet. The energy influx and O₂ sputtering rates from $\lambda_{\text{III}} = 191^\circ$ (maximum elongation above the magnetic equator) and $\lambda_{\text{III}} = 26^\circ$ (below) would therefore receive higher weights during the averaging than the two cases where Europa is located at the Jovian magnetic equator. However, the thickness of the Jovian plasma sheet is uncertain, with estimates in the literature differing by as much as 100% (e.g., Bagenal & Delamere, 2011; Roth et al., 2014). Thus, the factor with which to weight each of the four system III longitudes studied here cannot be precisely constrained. Previous studies have found that weighting each position differently does not noticeably alter the qualitative features of the particle influx maps, as long as the weights differ by less than a factor of approximately 5 (e.g., Addison et al., 2021; Liuzzo et al., 2020, 2022). We therefore proceed analogous to Addison et al. (2021) and weight all four cases equally in our averaging procedure. Averaging the surface particle fluxes across a full synodic rotation of Jupiter allows for an understanding of surface erosion at Europa over geologic timescales (e.g., millions of synodic rotations). Obtaining maps of the averaged electron influx and sputtering rates also facilitates comparison to the corresponding ion influxes determined by Addison et al. (2021, 2022), thereby constraining the relative contributions of ions and electrons to surface processing at Europa.

Figure 12 displays maps of the surface number flux (top row, Figures 12a–12c), energy influx (middle row, Figures 12d–12f), and O₂ sputtering rates (bottom row, Figures 12g–12i) of energetic magnetospheric particles averaged across a synodic rotation. The first column (Figures 12a, 12d, and 12g) displays the influxes and sputtering rates from energetic electron impacts, as calculated in this study. The second column shows the same quantities, but for energetic magnetospheric ion impacts (H⁺, O²⁺, and S³⁺), as calculated by Addison et al. (2022) employing the same combination of the AIKEF and GENTOO models used here. The study of Addison et al. (2022) modeled the influx patterns of energetic ions at exactly the same discrete energies studied here, also ranging from 5 keV to 10 MeV. We will discuss the ion influxes and associated sputtering rates only in the context of comparison to our electron results, and we encourage the reader to consult Addison et al. (2022) for a more complete description of our ion results. The final column of Figure 12 (Figures 12c, 12f, and 12i) displays the influxes and sputtering rates from energetic ions and electrons combined. For both the ion and electron results, the O₂ sputtering rates shown were calculated with the sputtering yield model of Teolis et al. (2017).

The first row of Figure 12 reveals that the number influx of energetic electrons dominates that of the energetic ions across the majority of Europa's surface. The energetic electron number flux exceeds that of the energetic ions by 1–2 orders of magnitude across the mid-to-high latitude upstream hemisphere and the polar caps (Figures 12a and 12b). The overall dominance of the energetic electron influx over the contribution from energetic ions reflects the higher ambient intensity $I(E)$ of electron fluxes measured by the Galileo EPD (Paranicas et al., 2001, 2009).

The influx pattern of energetic ions is far more spatially uniform than that of electrons, only varying by approximately a factor of 3.5 between different surface locations (Figure 12b), compared to three orders of magnitude for the electrons (Figure 12a). Energetic ion gyroradii can become a significant fraction of a European radius: the gyroradii of MeV ions can even exceed 1 R_E . Therefore, these particles are able to reach even the moon's

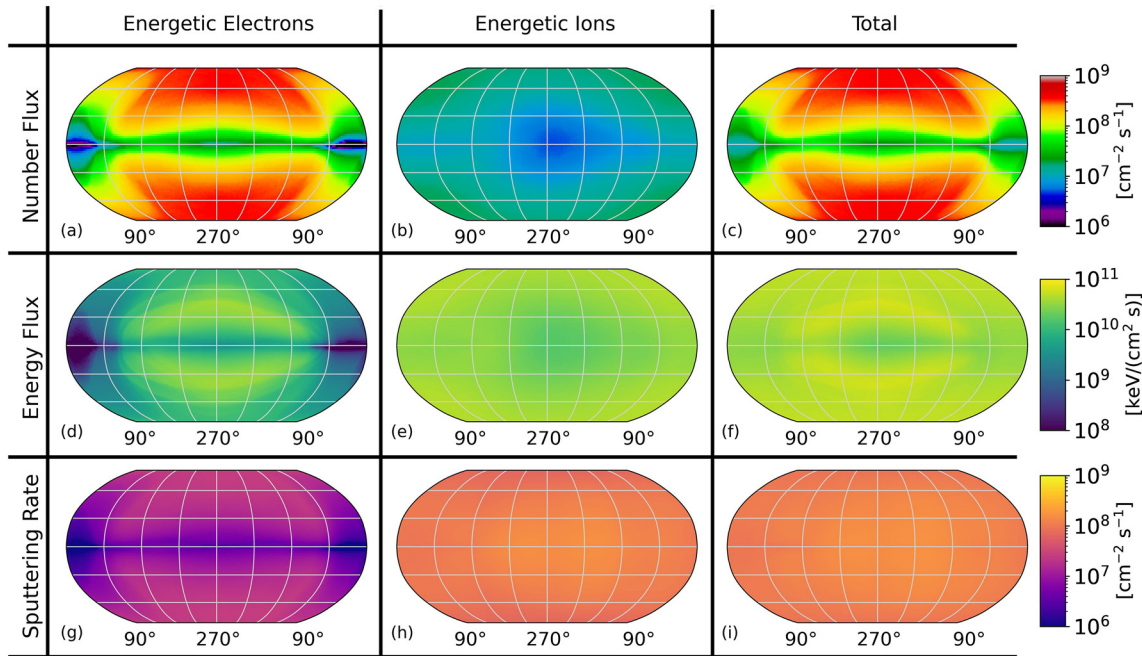


Figure 12. Surface maps of the energy-integrated number influx (panels a–c), energy influx (panels d–f), and O_2 sputtering rates (panels g–i) from energetic charged particles at Europa ($E \geq 5$ keV). All panels show quantities calculated with the draped fields from AIKEF. The first column (panels a, d, and g) displays the surface number flux, energy flux, and O_2 sputtering rate (respectively) from energetic electrons, as calculated in the present study, averaged over a full synodic rotation. The second column (panels b, e, and h) shows the same quantities for energetic *ion* impacts, calculated with averaged magnetospheric parameters over a synodic rotation. The results for the energetic ions have been adopted from Addison et al. (2022), see, for example, their Figure 9 for the sputtering rates. The third column (panels c, f, and i) displays the combined contributions of energetic ions and electrons to number influxes, energy influx, and O_2 sputtering rates. The sputtering rates from both ions and electrons are calculated with the O_2 sputter yield model of Teolis et al. (2017), using a diurnally-averaged surface temperature profile.

low-latitude downstream hemisphere merely through gyration. Over the energy range studied (5 keV–10 MeV), energetic ions also bounce too slowly for their flux tube to become depleted while traversing the moon's surface, in contrast to energetic electrons (Addison et al., 2021; Breer et al., 2019; Paranicas et al., 2009). Thus, while the rapid bounce motion and diminutive gyroradii of the electrons cause their number flux to be largely confined to the upstream hemisphere and poles (red in Figure 12a), the ions are able to more uniformly distribute across Europa's surface (Figure 12b). The superposition of the number flux maps for energetic ions and electrons largely resembles the influx pattern of energetic electrons (see Figure 12c), since the electron number flux exceeds that of the ions by roughly an order of magnitude at almost every surface location.

Similar to the surface number flux patterns, the energy influx of energetic *ions* is much more uniform across Europa's surface than that of energetic electrons, differing by at most a factor of three between different surface locations (Figures 12d and 12e). The quasi-uniform surface access of energetic ions throughout the energy range means that the ion energy flux is uniformly high (approximately 5.0×10^{10} keV $cm^{-2} s^{-1}$) across much of the surface (Figure 12e). The energy influx of energetic ions falls to its minimum value of approximately 1.6×10^{10} keV $cm^{-2} s^{-1}$ near the upstream apex. As described in Section 3.3, the regions of high electron energy flux onto Europa's surface are much more localized: the electron energy influx peaks within the two crescent-shaped enhancement features on the moon's mid-to-high latitude upstream hemisphere (yellow in Figure 12d). Only within the two crescent-shaped flux enhancements does the energy flux of energetic electrons quantitatively rival that of the energetic ions, reaching values near 4.0×10^{10} keV $cm^{-2} s^{-1}$. However, outside of the crescents, the electron energy flux falls as low as 2.0×10^5 keV $cm^{-2} s^{-1}$ (near the downstream apex), and the energy flux from energetic ions exceeds that from energetic electrons by up to four orders of magnitude (Figures 12d and 12e).

When taking the sum of the electron and ion energy fluxes, the resulting map therefore resembles the ion energy flux map across much of the surface, with the crescent-shaped enhancements in electron energy flux still being discernible (Figure 12f). Hence, the energy deposition of energetic magnetospheric particles onto Europa's surface maximizes on the upstream hemisphere near 30° north and 30° south latitude. The total energy influx

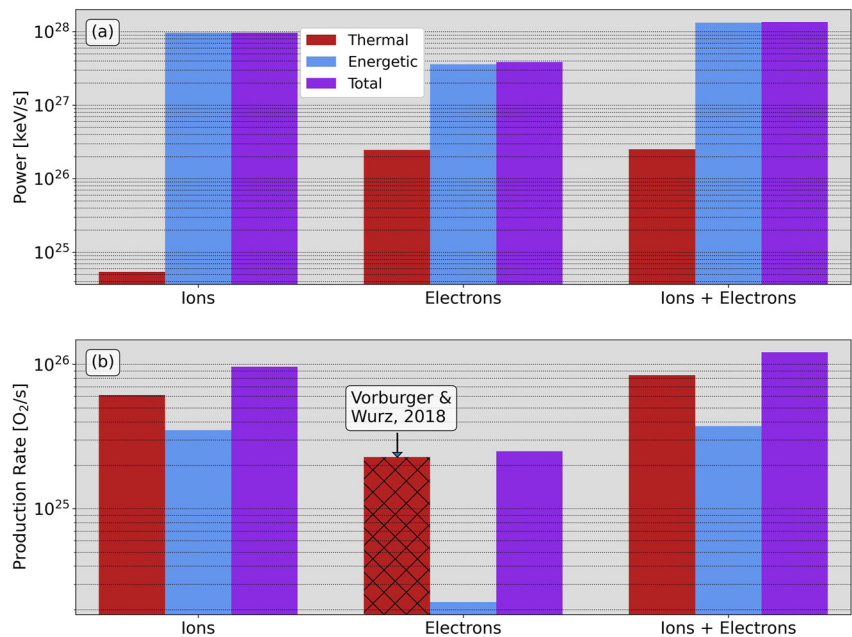


Figure 13. Power deposition (panel a) and O_2 production rates (panel b) from thermal (red), energetic (blue), and thermal plus energetic (purple) magnetospheric charged particle impacts, averaged across a synodic rotation and integrated across Europa's surface. In both panels, the left, center, and rightmost blocks display the integrated quantities from ion impacts (taken from Addison et al., 2022), electron impacts (from this study, as well as thermal electron O_2 production rates from Vorburger & Wurz, 2018), and the sum of the ion and electron contributions, respectively. The thermal electron power deposition was determined using Equation 8.

is lowest near the geographic equator, where the access of both ions and electrons is reduced. Thus, within the energetic regime ($E \geq 5$ keV), magnetospheric ions dominate the energy deposition onto Europa's polar caps and the entire downstream hemisphere, while electrons match the energy deposition of ions only in the mid-latitude upstream hemisphere. The combined energy deposition from ions and electrons maximizes within the upstream crescents at a value of approximately 6.6×10^{10} keV cm^{-2} s^{-1} , and minimizes near the upstream apex at a slightly lower value of about 1.8×10^{10} keV cm^{-2} s^{-1} . In other words, the net energy deposition from energetic magnetospheric particles onto Europa's surface varies at most by a factor of three between different surface locations. In particular, energy deposition by energetic ions refills the "gap" in energetic electron precipitation near the downstream apex.

The time-averaged O_2 sputtering rates from energetic electrons are quasi-uniform across Europa's upstream hemisphere poleward of 10° north/south latitude, but drop by over an order of magnitude near the upstream geographic equator and in the low-latitude downstream hemisphere (Figure 12g). The O_2 sputtering rates from energetic electron impacts maximize on the mid-latitude upstream hemisphere at a value of approximately 2.6×10^7 cm^{-2} s^{-1} . The sputtering rates from ions, in contrast, are largely uniform across the entire surface (Figure 12h), peaking at approximately 1.6×10^8 cm^{-2} s^{-1} near the upstream apex, and minimizing at 6.8×10^7 cm^{-2} s^{-1} at the poles. This slight spatial variability in the ion sputtering rates is largely due to non-uniformities in the diurnally-averaged surface temperature profile (Figure 3 of Addison et al., 2022), which maximizes around the upstream apex and minimizes at the poles. The quasi-uniform sputtering rates from energetic ions exceed those from energetic electrons at every point on Europa's surface: at the polar caps the difference is a factor of approximately 5, while at the upstream apex the difference reaches an order of magnitude. The O_2 sputtering rates from energetic ions again fill in the gap in electron sputtering near the downstream apex. The map of the O_2 sputtering rates from energetic ion and electron impacts combined (Figure 12i) therefore largely resembles the quasi-uniform sputtering map of energetic ions alone (Figure 12h).

In Figure 13 we integrate the energy flux and sputtering rate maps from Figure 12 in order to obtain the entire amount of power deposited onto Europa by energetic particles (Figure 13a) and the total production rate of O_2 from the moon's surface (Figure 13b). Analogous results for the total electron and ion number influxes are

presented and briefly discussed in Appendix C. In order to construct a complete picture of magnetospheric particle irradiation of Europa's surface, Figure 13 also includes the contribution from the thermal, corotating plasma. The contributions of *thermal and energetic ions* (leftmost blocks, red and blue bars, respectively) to power deposition and O₂ production are taken from the study of Addison et al. (2022). The power deposition and O₂ production rate from *energetic electron* impacts (center blocks, blue) have been calculated in this study using the GENTOO model in combination with the draped fields from AIKEF. The surface irradiation by *thermal electrons* (center blocks, red bars), however, cannot be calculated with the same approach. Thermal electrons interact with Europa's exosphere via, for example, excitation and electron-impact ionization (e.g., Carberry Mogan et al., 2023; Saur et al., 1998), processes which cannot be captured in the existing GENTOO backtracing framework. We therefore estimate the contribution of thermal electrons using an analytical approach.

To estimate the power deposition by *thermal electrons*, we assume that these particles isotropically irradiate every location on Europa's surface. The velocity distribution of the ambient thermal electron population follows a Maxwellian profile with temperature $k_B T_0 = 100$ eV (Kivelson et al., 2009), and drifts at the bulk velocity $u_0 = 100$ km/s along the x direction (see also Section 2.1). The half-width of the electron velocity distribution at Europa's orbit is $v_{th} = \sqrt{2k_B T_0/m_e} \approx 6,000$ km/s, substantially larger than the bulk velocity. Thus, in the absence of, for example, field line draping or electron-neutral interactions, the thermal electron influx onto Europa's surface would be largely isotropic. The energy flux onto any surface location is then given by

$$J_E = \int d^3v f(v) v_r \cdot \frac{1}{2} m_e v^2, \quad (5)$$

where d^3v is a volume element in velocity space, $f(v)$ is the ambient velocity distribution of the thermal electrons, v_r is the radial component of an electron macroparticle's velocity vector \mathbf{v} relative to Europa's center, and m_e is the electron mass. Neglecting the bulk velocity u_0 , the Maxwellian distribution is given by

$$f(v) = n_0 \left(\frac{m_e}{2\pi k_B T_0} \right)^{3/2} \exp\left(-\frac{m_e v^2}{2k_B T_0}\right). \quad (6)$$

Equation 5 can then be rewritten as

$$J_E = \int_{v=0}^{v_{\max}} \int_{\phi_v=0}^{2\pi} \int_{\theta_v=0}^{\pi/2} n_0 \left(\frac{m_e}{2\pi k_B T_0} \right)^{3/2} \exp\left(-\frac{m_e v^2}{2k_B T_0}\right) \frac{m_e}{2} v^5 \cos(\theta_v) \sin(\theta_v) d\theta_v d\phi_v dv, \quad (7)$$

where θ_v and ϕ_v are the polar and azimuthal angles in velocity space, with θ_v measured against the local surface normal (as described in Section 2.2), n_0 is the upstream density, and v_{\max} is the maximum velocity where we cut off the integration. Equation 7 then yields

$$J_E = n_0 k_B T_0 \sqrt{\frac{2k_B T_0}{m_e \pi}} \left\{ 1 - \exp(-\lambda) \left[\frac{1}{2} \lambda^2 + \lambda + 1 \right] \right\}, \quad (8)$$

where $\lambda = \frac{E_{\max}}{k_B T_0}$ is the ratio of the maximum energy of the integration $E_{\max} = \frac{1}{2} m_e v_{\max}^2$ to the thermal energy $k_B T_0$. We select a value of $E_{\max} = 2$ keV, corresponding to $v_{\max} = 26,524$ km/s, which is more than four standard deviations v_{th} from the peak of the Maxwellian distribution, thereby effectively encompassing the entire thermal electron population.

We use Equation 8 to calculate the (uniform) value of the *local* energy influx for all four of system III longitudes examined in this study, using the different values of n_0 given in Table 1. We then combine the results to obtain the average local energy influx by thermal electrons over a full synodic rotation. Following this procedure, we obtain a value of $\langle J_E \rangle = 4.02 \times 10^9$ keV cm⁻² s⁻¹. Integrating this value across the entire surface yields a total power deposition from thermal electrons of $4\pi R_E^2 \langle J_E \rangle = 1.23 \times 10^{27}$ keV s⁻¹. Analogous to Vorburger and Wurz (2018), we reduce this value by 80% to account for deflection of the thermal electrons around Europa by the electromagnetic field perturbations. Thus, we derive an approximate power deposition from thermal electrons onto Europa's surface of 2.46×10^{26} keV s⁻¹, represented by the red bar in the middle block of Figure 13a.

As seen in Figure 13a, energetic ions deposit the vast majority of the power from charged particle impacts onto Europa's surface. Of the total power deposited onto the surface (1.35×10^{28} keV s⁻¹, or 2,163 GW, purple bar

in the rightmost block), ions contribute approximately 72% (9.66×10^{27} keV s⁻¹, or 1548 GW, purple bar in the leftmost block), while electrons contribute the remaining 28% (3.85×10^{27} keV s⁻¹, or 617 GW, purple bar in the center block). The power deposited by ions consists of 99.9% the energetic ion contribution, and 0.1% the thermal ion contribution (left block in Figure 13a). For the electron power deposition, energetic electrons contribute approximately 93.6%, while thermal electrons contribute the remaining 6.4% (middle block in Figure 13a).

Our estimate for the total power deposited onto Europa's surface by charged particle impacts (2,163 GW) is approximately 44% lower than suggested by Cooper et al. (2001), who estimated a value of 3,826 GW. In our model, local reductions in the electron influx patterns are caused by two effects: (a) the partial shielding of the surface by the electromagnetic field perturbations and (b) the emptying of flux tubes due to the bounce motion of the electrons. Neither of these two effects was included in the calculations of Cooper et al. (2001), explaining the somewhat higher power deposition onto Europa's surface in their estimate. In addition, the relative contributions of ions and electrons to the total power deposition in our model are reversed compared to the findings of those authors: Cooper et al. (2001) estimate that *electrons* contribute approximately 75% of the total power, while ions contribute only 25% (compared to 28% and 72% in our model, respectively). Our results show that electrons with energies above approximately 10 keV can reach only localized regions of Europa's surface, while ions can uniformly access nearly every surface location across the entire energy range (Addison et al., 2021, 2022). However, due to the saturation of the observed ambient electron count rates (see Section 2.2), the contribution of electrons to energy deposition may be somewhat higher than suggested here.

Figure 13b displays the O₂ production rates of impinging ions (leftmost block), electrons (center block), and the combined rate of both ions and electrons (rightmost block). Similar to the power deposition, the production rates from magnetospheric ion impacts (thermal and energetic) are taken from Addison et al. (2022), while the rates from energetic electron impacts have been calculated in the present study. The O₂ production rate by thermal electron impacts is represented by the estimation of Vorburgeter and Wurz (2018), see also Section 3.3. Figure 13b reveals that the total O₂ production rate from Europa, averaged over a synodic rotation, is approximately 1.22×10^{26} O₂ molecules per second, or about 6.5 kg of O₂ per second (purple bar, rightmost block). Magnetospheric ions impacts contribute about 79% of this sputtered O₂ (5.16 kg/s, purple bar, leftmost block), while magnetospheric electrons contribute the other 21% (1.34 kg/s, purple bar, center block). Roughly 64% of the total ion production rate of O₂ (purple bar, leftmost block) is a result of thermal ion impacts (red bar, leftmost block), while the remaining 36% is contributed by energetic ions (blue bar, leftmost block). Of the contribution of electrons to O₂ production (purple bar, center block), 91% comes from thermal electron impacts (red bar, center block), while only 9% comes from energetic electrons (blue bar, center block).

Davis et al. (2021) estimate the production rate of O₂ from magnetospheric electron sputtering at Europa to range from 8.5 to 11.75 kg/s, which is a factor of 8–10 higher than our estimate (1.34 kg/s), and slightly higher than our calculated production rate for magnetospheric ions and electrons combined (6.5 kg/s). Davis et al. (2021) compared their estimated O₂ production rates from electrons to the production rates from ion impacts in uniform fields (5.35 kg/s) calculated by Cassidy et al. (2013). In this way, Davis et al. (2021) asserted that electrons are the dominant agents of O₂ production at Europa. However, our results indicate that the O₂ production rate from electron impacts given by Davis et al. (2021) is an overestimate, and that magnetospheric ions actually sputter roughly four times more O₂ from Europa's surface than electrons. Vorburgeter and Wurz (2018) suggest that magnetospheric ions sputter roughly 1.7 times more O₂ than magnetospheric electrons, slightly less than the factor of four suggested by our study. However, in agreement with the findings of both Vorburgeter and Wurz (2018) and Davis et al. (2021), our results do indicate that sputtering of O₂ from Europa's surface by magnetospheric *electrons* is not negligible, constituting roughly 20% of the total O₂ production. It is therefore critical that future analysis incorporate the contributions of both ions *and* electrons to O₂ sputtering when investigating the generation and evolution of Europa's exosphere.

Dalton et al. (2013) utilized their modeled maps of the ion and electron influx patterns (calculated with uniform electromagnetic fields) to search for correlations to the concentrations of sulfuric acid (H₂SO₄) on Europa's surface, observed at various locations by the Galileo Near Infrared Mapping Spectrometer (NIMS). These authors found a strong correlation between the observed local H₂SO₄ concentrations and both (a) magnetospheric sulfur ion *number* influx and (b) magnetospheric electron *energy* influx at the respective locations (correlation coefficient $r = 0.93$ and $r \approx 0.75$, respectively). Dalton et al. (2013) hypothesized that the presence of observable H₂SO₄ at a certain surface location requires (a) magnetospheric sulfur ions

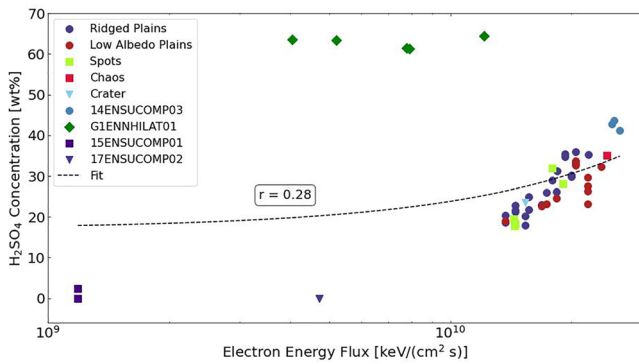


Figure 14. Sulfuric acid (H_2SO_4) concentration at selected locations on Europa's surface, as observed by the Galileo NIMS instrument (Dalton et al., 2013), versus the electron energy influx at the respective locations, as calculated in our study. The electron energy influx used is the sum of the energetic electron energy influx calculated with our numerical modeling framework (Figure 12d) and the spatially-uniform energy flux from thermal electrons derived with Equation 8. Different markers denote observations from different locations and geomorphological features on Europa's surface (see Dalton et al. (2013) for more information on the NIMS observations). To guide the reader's eye, a linear fit is shown with a black, dashed line, and the correlation coefficient r is indicated in the black box. The NIMS data set contains *three* measurements labeled 15ENSUCOMP01 (purple squares in the lower left corner), however, the positions of two of these measurements overlap in the plot.

to implant into the surface ice and serve as the “feedstock” for sulfuric acid production and (b) impinging electrons to “heat” the surface at the same locations, thereby allowing sulfur ions to implant more effectively. Addison et al. (2021) investigated whether the correlation between local H_2SO_4 surface concentration and sulfur ion number influx persists when field line draping is taken into account in the model of sulfur ion bombardment. These authors found that the inclusion of the draped fields only slightly weakens the correlation obtained by Dalton et al. (2013) with uniform fields: Addison et al. (2021) calculated a correlation coefficient of $r = 0.77$ between these two quantities. Thus, the findings of Addison et al. (2021) support the notion that local implantation of exogenic sulfur provides the “feedstock” necessary for sulfuric acid production on Europa's surface.

Using the new results from our electron model, we now investigate whether the correlation between modeled electron *energy* influx and observed sulfuric acid concentration across Europa's surface (Dalton et al., 2013) still persists when field line draping is considered. Figure 14 displays the H_2SO_4 concentrations observed by the Galileo NIMS across a diverse array of surface terrains (indicated by the different markers, taken from Dalton et al., 2013) versus the modeled electron energy influx at each location. The H_2SO_4 concentrations were observed across a diverse array of surface terrains, distributed largely across the low-to-mid latitude regions of the moon's upstream to anti-Jovian hemisphere. To obtain the energy flux deposited by magnetospheric electrons at each of these locations, we take the energy influx maps from energetic electrons (Figure 12d) and uniformly add our estimated energy flux from the thermal electrons (Equation 8), again reduced by 80% to account for the field perturbations (Vorburger & Wurz, 2018).

Figure 14 reveals that the strong correlation between H_2SO_4 concentration and electron energy surface flux found by Dalton et al. (2013) does *not* persist when the field perturbations are taken into account. The linear correlation coefficient of $r \approx 0.75$ calculated by those authors for uniform electromagnetic fields drops to a value of only $r = 0.28$ when using the electron energy fluxes from our model. Our results suggest that the electron energy influx across Europa's surface is much more uniform than in the model of Dalton et al. (2013): their approach predicts differences of up to nine orders of magnitude between the energy flux onto the upstream and downstream hemispheres.

The uniform energy influx from thermal electrons used in our analysis (derived from Equation 8) is below the energy influx from energetic electrons at nearly every surface location except a narrow region in the low-latitude downstream hemisphere (dark blue in Figure 12d). Only 3 of the 55 NIMS data points (Table 2 of Dalton et al., 2013) were from this region, namely those marked 15ENSUCOMP01, indicated with purple squares in Figure 14. These observations were taken at 7.3° north latitude, and 114° west longitude, that is, on the low-latitude downstream hemisphere 24° west of the downstream apex. Thus, only these three data points lie in the region where our estimated, uniform thermal electron energy influx exceeds our numerically-modeled energetic electron influx. If we remove these three data points when determining the correlation between electron energy influx and H_2SO_4 concentration, the correlation coefficient falls to $r = 0.07$. Thus, the correlation is even *weaker* than with all data points from Dalton et al. (2013) included. In other words, even discarding the few data points that are strongly affected by our approximate treatment of the thermal electron energy influx would not strengthen the proposed correlation, since the electron energy flux at nearly every surface location included in our initial analysis (Figure 14) is dominated by the energetic particles.

Our results therefore indicate that local electron “heating” of Europa's surface is *not* required for the production of H_2SO_4 in the respective region, as proposed by Dalton et al. (2013). Neither is heating by magnetospheric ion impacts required, as both the studies of Dalton et al. (2013) and Addison et al. (2022) have shown that (modeled) ion *energy* influx and (observed) H_2SO_4 concentrations are not strongly correlated. Thus, the combination of our results for electron *energy* influx with those of Addison et al. (2021) for sulfur ion *number* influx suggests that

the only requirement for the production of H_2SO_4 at a certain location on Europa's surface, as detected by NIMS, is the local availability of exogenic, magnetospheric sulfur ion “feedstock.”

However, we point out that the weak correlation between electron energy deposition and H_2SO_4 concentration in our model is strongly affected by the five outliers represented by green diamonds in Figure 14 (data set GIENN-HILAT01). If we remove these five data points, the correlation coefficient drastically increases to $r = 0.95$. Assuming that this series of measurements is—for some reason—anomalous, our model would suggest that there exists a very strong correlation between electron energy influx and sulfuric acid concentration at the sampled surface locations. Such a result would confirm the hypothesis of Dalton et al. (2013). The five locations indicated by the green diamonds are clustered around Europa's upstream apex, that is, within the region where the sulfur ion number flux onto the surface peaks (see Figure 9 of Addison et al., 2021). We hypothesize that this surplus of sulfur ion influx allows the surface sampled at these five locations to sustain a high H_2SO_4 concentration, despite the low electron energy influx. This may be a possible explanation why these five points are above the proposed linear trend.

3.5. Role of an Anisotropic Pitch Angle Distribution in Shaping Energetic Electron Surface Influx Patterns

For our model runs presented in Sections 3.2–3.4, we have treated the pitch angle distribution (PAD) of the ambient energetic electrons as isotropic. To constrain the robustness of our results, we now investigate how including an anisotropic PAD would alter the surface influx maps of energetic electrons. Observations by the Galileo and Juno spacecraft (e.g., Ma et al., 2021; Nénon et al., 2022) suggest that the PAD of energetic electrons near Europa changes with time and magnetic latitude, and varies between isotropic and pancake distributions (i.e., with higher particle fluxes near pitch angles of 90° and fewer near 0° and 180°). We therefore calculated maps of the surface number flux of energetic electrons using a pancake PAD ($\propto \sin(\alpha)$, where α is the pitch angle). Results are presented here for a single simulation setup: Europa located at the magnetic equator (southward sweep, $\lambda_{\text{III}} = 110^\circ$) with the draped fields from AIKEF. Figure 15 displays maps of the surface number fluxes calculated with a pancake PAD for electrons with energies of 10 keV (Figure 15a), 100 keV (Figure 15b), 1 MeV (Figure 15c), and 10 MeV (Figure 15d). The corresponding influx maps calculated with an isotropic PAD are given in the second column of Figure 5.

For the entire range of electron energies considered, the influx maps calculated with an isotropic PAD and with a pancake PAD are qualitatively identical (right column of Figure 5 vs. Figure 15). Differences between the two cases are highly localized, and only on the order of a few percent. Since a pancake PAD contains more particles with pitch angles close to 90° , a slightly higher number of particles are locally mirrored by Europa's field perturbations (similar to the trajectory shown in Figure 7), and ultimately impact the moon outside of the crescent features. This difference is, however, too subtle to be discernible in the flux maps shown in Figure 15. Overall, changing the ambient electron PAD from isotropic to pancake does not make a substantial quantitative difference in the influx patterns of energetic electrons.

4. Summary and Concluding Remarks

We have presented the first model of magnetospheric electron bombardment of Europa which takes into account the electromagnetic field perturbations arising from both (a) induction in the moon's subsurface ocean and (b) the moon's interaction with the upstream Jovian plasma. Our approach combines an established hybrid model of the draped fields near Europa (e.g., Addison et al., 2021, 2022) with a relativistic electron backtracing code to model magnetospheric electron dynamics (Liuzzo et al., 2019a, 2022). In order to capture the bounce motion of energetic electrons in Jupiter's magnetosphere, we have coupled our local European interaction model with the latest Juno-era models of Jupiter's internal and magnetodisc fields (Connerney et al., 2020, 2022). We have investigated energetic electron precipitation onto Europa at four discrete positions of the moon relative to the Jovian magnetic equator. These results have then been combined to obtain a picture of the averaged electron precipitation patterns onto the moon over a synodic rotation. In addition to the number flux patterns of energetic electrons on Europa's surface, we have also calculated maps of the energy flux and O_2 sputtering rates resulting from electron impacts. By comparing our results for magnetospheric electron bombardment with those of Addison et al. (2022) for *ion*

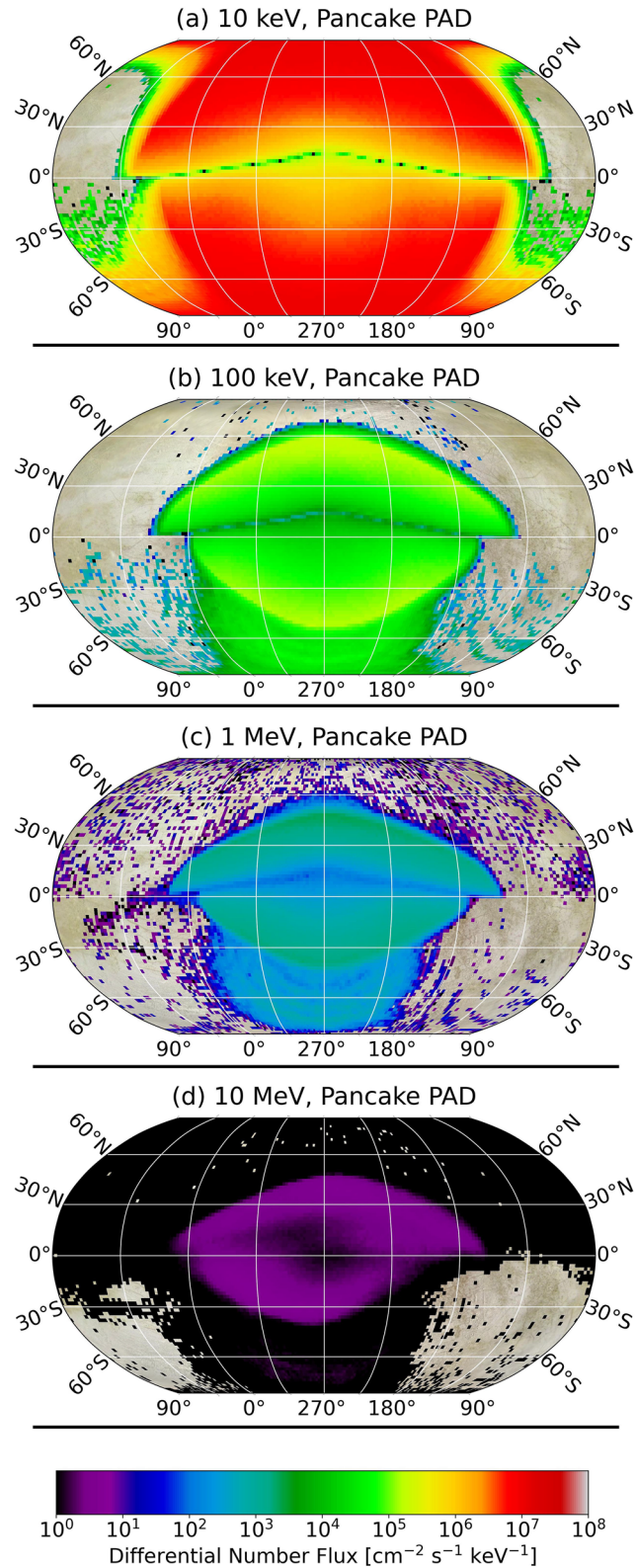


Figure 15. Maps of the surface number flux calculated with a pancake PAD for 10 keV, 100 keV, 1 MeV, and 10 MeV electrons (panels a, b, c, and d, respectively). In each case, the influx patterns were calculated with the draped fields from AIKEF, while Europa is located at a system III longitude of $\lambda_{\text{III}} = 110^\circ$ (magnetic equator, southward sweep).

bombardment, we have constrained the relative contributions of ions and electrons to power deposition and O₂ production at Europa.

Our main results are as follows.

- In contrast to the case of magnetospheric ion impacts (Addison et al., 2021, 2022), the perturbed fields near Europa do *not* substantially alter the influx patterns of energetic electrons onto the moon's surface. The spatial distribution of the energetic electron influx is largely determined by the bounce motion of these particles between Europa and their mirror points at higher Jovian magnetic latitudes. The energetic electron influx is largely focused in two crescent-shaped regions which cover the poles and mid-latitude upstream hemisphere at low electron energies ($E \leq 10$ keV), and gradually move toward the upstream equator as the electron energy increases. Inclusion of the electromagnetic field perturbations causes a slight redistribution of these influx patterns.
- The intensities and patterns of energetic electron influx onto Europa's surface show subtle variations with system III longitude (i.e., distance between the moon and the planetary magnetic equator). For instance, the crescent-shaped enhancements slightly warp in response to the different magnetospheric conditions. Europa's induced dipole acts as a local magnetic mirror for energetic electrons with pitch angles near 90°, allowing some of these particles to impact the surface outside of the crescent-shaped influx maxima. The induced dipole moment and hence, the locations where these locally mirrored particles finally hit the surface change as a function of Europa's system III longitude.
- Europa's downstream hemisphere receives non-negligible amounts of energetic electron energy influx (locally reaching up to $\approx 10^9$ keV cm⁻²s⁻¹), even below the “critical” energy (≈ 20 –25 MeV) where electrons begin to drift antiparallel to the corotation direction. Electrons with energies below $E \leq 10$ keV possess sufficiently large azimuthal displacements r_{ac} to reach the moon's downstream hemisphere entirely through their bounce motion in Jupiter's magnetic field. Only a narrow region around Europa's downstream apex is entirely protected from such electron impacts.
- For our chosen model setup, the power deposited onto the entire surface from magnetospheric ions and electrons is 2,163 GW, roughly 44% lower than suggested by Cooper et al. (2001). The total power deposition onto Europa's surface via magnetospheric particle impacts is dominated by ions (72%), with a smaller contribution from electrons (28%). However, given the uncertainty in the ambient thermal plasma density and electron flux, electrons and ions may make comparable contributions to power deposition onto Europa's surface. Magnetospheric particle impacts deposit energy quasi-uniformly across Europa's surface: between different surface locations, the power deposition varies by no more than a factor of 3.5. In particular, energy deposition from energetic ions refills the “gap” in the electron precipitation pattern near the downstream apex.
- In our model, roughly 80% of the sputter-generated O₂ in Europa's exosphere is released by magnetospheric ion impacts, with the remaining 20% released by electrons. Since electrons and ions make substantial contributions to surface sputtering at Europa, both must be taken into consideration when constraining O₂ source processes for the moon's exosphere. Magnetospheric ions and electrons combine to release approximately 6.5 kg of O₂ per second from Europa's surface through sputtering.
- We find only a weak correlation between surface concentrations of H₂SO₄ observed by Galileo NIMS (Dalton et al., 2013) and our modeled electron energy influx patterns. This result, in conjunction with those of Addison et al. (2021) for ion precipitation, suggests that electron energy deposition is not an agent required to facilitate the production of H₂SO₄ on Europa's surface. However, there exists a strong correlation between the influx patterns of sulfur ions onto the moon and observed H₂SO₄ concentrations (Addison et al., 2021). We therefore suggest that the sole requirement for H₂SO₄ production within Europa's surface is a supply of exogenic sulfur “feedstock.” However, the correlation would be strengthened drastically if a set of outlier observations near Europa's upstream apex were removed from the data set.
- In general, plasma interaction models like AIKEF reproduce large-scale trends observed in the electromagnetic fields at Europa very well (e.g., pileup or draping). However, transient features like, for example, ion cyclotron waves (e.g., Desai et al., 2017; Volwerk et al., 2001) are not captured by this type of model. Such electromagnetic features can locally deflect electron trajectories, thus introducing some degree of uncertainty into the calculated precipitation patterns. Our analysis is based on the implicit assumption that such electromagnetic signatures would not affect the average morphology of surface precipitation at a certain orbital position.

The combination of the AIKEF hybrid model and the GENTOO particle-tracer used here cannot capture the detailed patterns of *thermal* electron precipitation onto Europa's surface. Thermal electrons interact with Europa's exosphere through, for example, impact ionization and excitation of neutral O₂ (Carberry Mogan et al., 2023; Saur et al., 1998). The AIKEF model alone cannot provide a self-consistent description of thermal electron dynamics either, since it treats these particles as a massless fluid (Müller et al., 2011). Thus, throughout this paper we have resorted to (semi-)analytical estimations of the thermal electron number flux (Appendix C), energy influx (Section 3.4), and O₂ sputtering rate (Vorburger & Wurz, 2018). As such, the contribution of thermal electrons remains an uncertainty in our model results. Consequently, the next step in refining the model is to trace the dynamics of the thermal electrons through Europa's perturbed electromagnetic environment while including the interaction of these particles with the moon's neutral envelope. Such an investigation requires either (a) a forward-tracing model of electron dynamics near Europa or (b) a substantial rethinking of the backtracing approach applied here.

Appendix A: Europa Located at the Magnetic Equator (Northward Sweep, $\lambda_{\text{III}} = 284^\circ$)

Figure A1 displays maps of the differential number flux deposited by energetic electrons at 10 keV, 100 keV, 1 MeV, and 10 MeV, calculated while Europa is located at the Jovian magnetic equator, and the equator is sweeping *northward* over the moon ($\lambda_{\text{III}} = 284^\circ$). The layout of the Figure is the same as that of Figures 5 and 8. However, only the flux maps calculated with the draped fields from AIKEF are shown. The maps shown in Figure A1 are highly similar to those shown in Figure 5 (magnetic equator, *southward* sweep, i.e., $\lambda_{\text{III}} = 110^\circ$). The background magnetic field vector is similar to that at $\lambda_{\text{III}} = 110^\circ$, but has a *negative* $B_{0,x}$ component instead of a positive one. Therefore, the most prominent features in the flux patterns are mirrored across Europa's geographic equator compared to Figure 5.

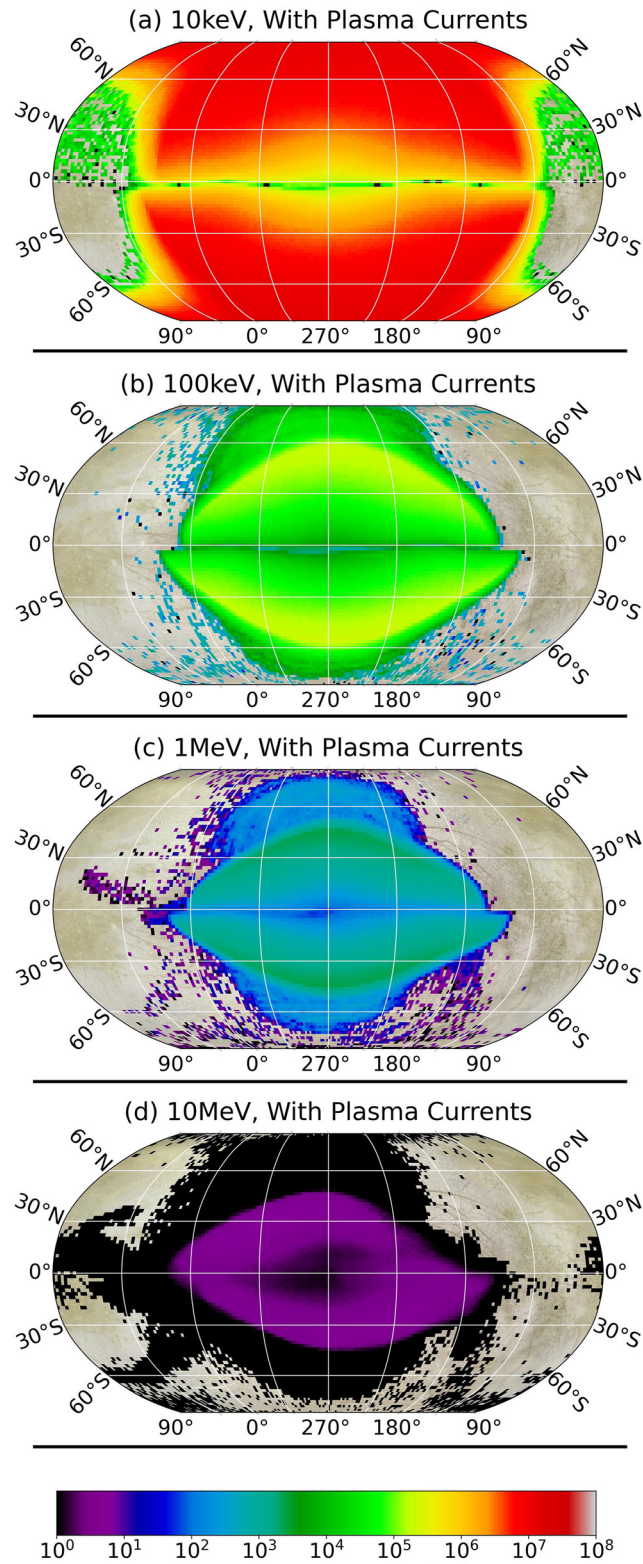


Figure A1. Differential energetic electron number fluxes onto Europa's surface while the moon is located at the Jovian magnetic equator and the equator is sweeping *northward* across the moon ($\lambda_{\text{III}} = 284^\circ$). The differential surface number fluxes were calculated with the draped electromagnetic fields from AIKEF.

Appendix B: Europa Located at Maximum Distance Below the Magnetic Equator ($\lambda_{\text{III}} = 26^\circ$)

In Figure B1 we show maps of the differential surface number flux of energetic electrons at 10 keV, 100 keV, 1 MeV, and 10 MeV, calculated with the draped fields from AIKEF while Europa is located at its maximum distance *below* the Jovian magnetic equator ($\lambda_{\text{III}} = 26^\circ$). The layout of the figure is the same as that of Figure A1. The Jovian magnetospheric field vector near the moon is very similar to that when Europa is located at its maximum distance *above* the planetary magnetic equator ($\lambda_{\text{III}} = 191^\circ$, see Table 1). However, while $B_{0,y}$ was negative in Figure 8, the horizontal component of the ambient field points toward Jupiter in the scenario shown here (i.e., $B_{0,y} > 0$). The spatial distribution of the energetic electron influx features is very similar to the patterns seen in Figure 8.

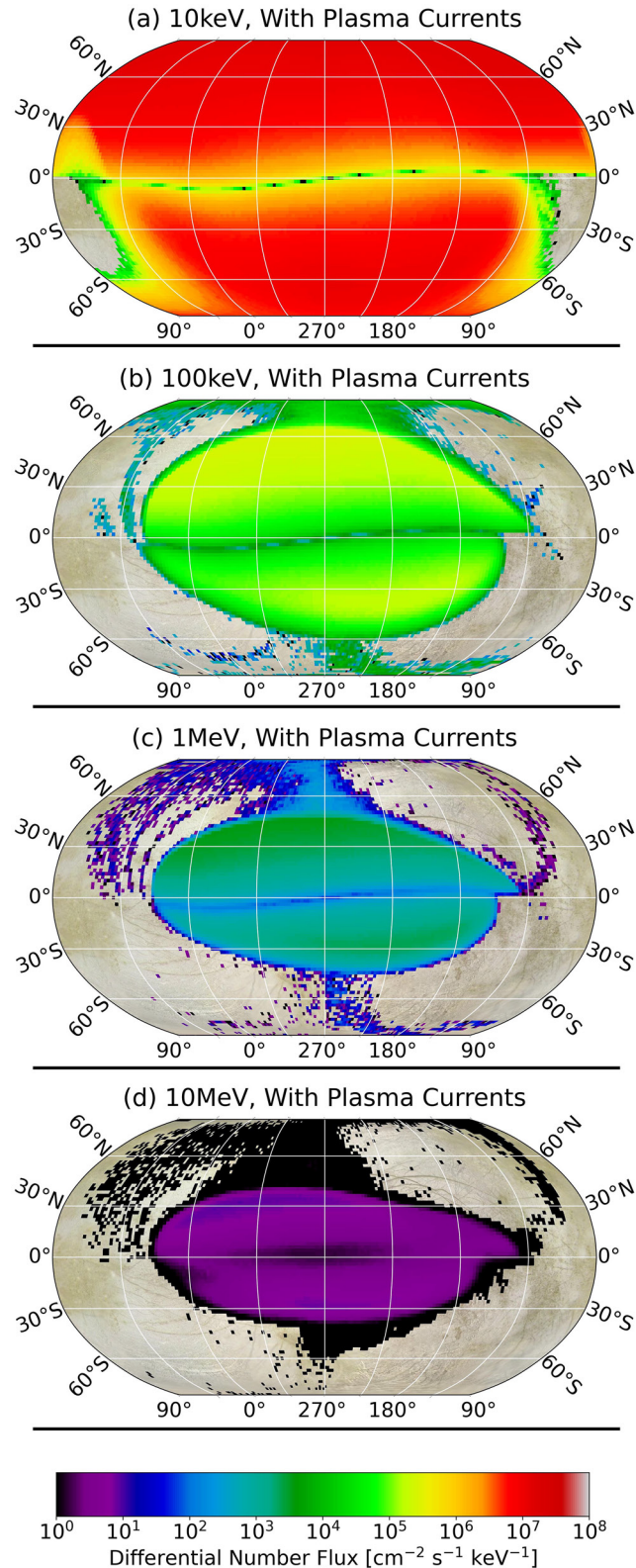


Figure B1. Differential energetic electron number fluxes onto Europa's surface while the moon is located at its maximum distance below the magnetic equator ($\lambda_{\text{III}} = 26^\circ$). The layout of the plots is the same as in Figure A1. The differential surface number fluxes were calculated with the draped electromagnetic fields from AIKEF.

Appendix C: Average Precipitation Rate of Ions and Electrons Onto Europa's Surface Across a Synodic Rotation

Figure C1 displays the precipitation rates of magnetospheric ions (leftmost block), electrons (center block), and the combined precipitation rates of both ions and electrons (rightmost block) onto Europa's entire surface, averaged over a synodic rotation (analogous to Figure 13 for power deposition and O₂ production rates). The contributions of thermal particles are shown in red, while the contributions of energetic particles are displayed in blue, and the combined rates of thermal and energetic particles are in purple. Results are again shown for draped electromagnetic fields only. Similar to Section 3.4, the precipitation rates of (thermal and energetic) ions are taken from Addison et al. (2022), while the precipitation rates of *energetic* electrons have been calculated with GENTOO in this study. For the surface influx of *thermal* electrons we use an analytical estimation of the thermal electrons in the ambient flow analogous to Equation 8: we integrate the Maxwellian velocity distribution, assuming that the number influx J is uniform across the entire surface:

$$J = \int d^3v f(v) v_r. \quad (C1)$$

Transforming this expression into polar coordinates yields

$$J = \int_{v=0}^{v_{\max}} \int_{\phi_v=0}^{2\pi} \int_{\theta_v=0}^{\pi/2} n_0 \left(\frac{m_e}{2\pi k_B T_0} \right)^{3/2} \exp\left(-\frac{m_e v^2}{2k_B T_0}\right) v^3 \cos(\theta_v) \sin(\theta_v) d\theta_v d\phi_v dv. \quad (C2)$$

Performing the integration then leads to

$$J = n_0 \sqrt{\frac{k_B T_0}{2\pi m_e}} \{1 - \exp(-\lambda)(\lambda + 1)\}, \quad (C3)$$

where again $\lambda = E_{\max}/(k_B T_0)$ and $E_{\max} = \frac{1}{2} m_e v_{\max}^2$ is the integration cut-off energy. Similar to Section 3.4, we perform this integration over the energy range from 0 to 2 keV, thereby encompassing the entire thermal electron distribution. We again average this value across all four system III longitudes investigated in this study. This procedure then yields a thermal electron number influx at each surface location of $\langle J \rangle = 2.01 \times 10^{10} \text{ cm}^{-2} \text{ s}^{-1}$. Integrating this value across the entire surface yields an average thermal electron precipitation rate of $4\pi R_E^2 \langle J \rangle = 6.15 \times 10^{27} \text{ s}^{-1}$. Analogous to Vorburger and Wurz (2018), we reduce this value by 80% to account for deflection of the thermal plasma around Europa by the electromagnetic field perturbations. Thus, we arrive at an average thermal electron precipitation rate of $1.23 \times 10^{27} \text{ s}^{-1}$.

Figure C1 reveals that the electrons, particularly in the thermal regime (red bar, center block), dominate the charged particle number flux onto Europa's surface. Of the total precipitation rate (purple bar, rightmost block), electrons contribute 98.8% ($1.28 \times 10^{27} \text{ s}^{-1}$, red bar, rightmost block), while ions contribute 1.2% ($1.49 \times 10^{25} \text{ s}^{-1}$,

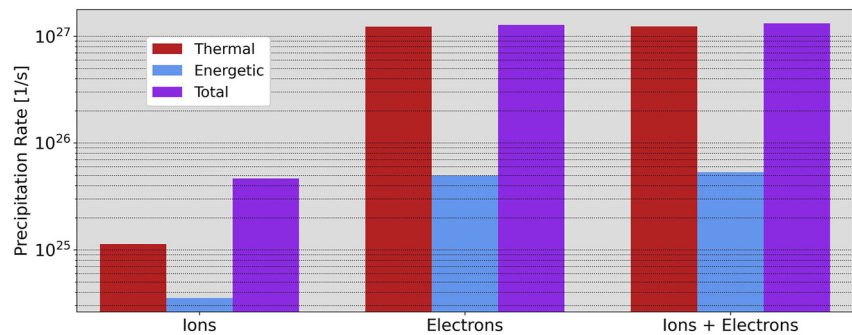


Figure C1. Precipitation rates of ions and electrons, integrated across Europa's entire surface, and averaged across a synodic rotation. The leftmost block displays the precipitation rates of magnetospheric ions, taken from Addison et al. (2022) and calculated with draped fields. The center block shows the precipitation rates of magnetospheric electrons, while the rightmost block displays the combined precipitation rates of magnetospheric ions and electrons. The precipitation rate of energetic electrons is determined using the GENTOO model and the draped fields from AIKEF, while the precipitation rate of thermal electrons is determined from Equation C3.

blue bar, rightmost block). The bulk of the electron number flux is imparted by the thermal electrons (96% of the electron contribution, red bar, center block), while 76% of the ion contribution is provided by the thermal ions (red bar, leftmost block). For both ions and electrons, the energetic populations are less abundant in the ambient plasma, causing their surface precipitation rates (blue bars) to be 1–2 orders of magnitude lower than those of the thermal particles (red bars). However, since particles with $E \geq 5$ keV carry substantially more energy than thermal particles, they still make by far the dominant contribution to the surface power deposition (Figure 13).

Data Availability Statement

Results from both the AIKEF hybrid model and the GENTOO particle-tracing code can be downloaded from the data set provided in Addison et al. (2023).

Acknowledgments

The authors are grateful to the NASA Solar System Workings 2018 Program (Grant 80NSSC20K0463) for financial support. The authors would also like to thank both reviewers for their careful inspection of the manuscript and valuable comments.

References

- Abdulgalil, A. G. M., Rosu-Finsen, A., Marchione, D., Thrower, J. D., Collings, M. P., & McCoustra, M. R. S. (2017). Electron-promoted desorption from water ice surfaces: Neutral gas-phase products. *ACS Earth and Space Chemistry*, 1(4), 209–215. <https://doi.org/10.1021/acsearthspacechem.7b00028>
- Addison, P., Liuzzo, L., Arnold, H., & Simon, S. (2021). Influence of Europa's time-varying electromagnetic environment on magnetospheric ion precipitation and surface weathering. *Journal of Geophysical Research: Space Physics*, 126(5), e2020JA029087. <https://doi.org/10.1029/2020JA029087>
- Addison, P., Liuzzo, L., & Simon, S. (2022). Effect of the magnetospheric plasma interaction and solar illumination on ion sputtering of Europa's surface ice. *Journal of Geophysical Research: Space Physics*, 127(2), e2021JA030136. <https://doi.org/10.1029/2021JA030136>
- Addison, P., Liuzzo, L., & Simon, S. (2023). Data for "Surface-plasma interactions at Europa in draped magnetospheric fields: The contribution of energetic electrons to energy deposition and sputtering" by Addison et al., 2023. [Dataset]. Zenodo. <https://doi.org/10.5281/zenodo.7982893>
- Arnold, H., Liuzzo, L., & Simon, S. (2019). Magnetic signatures of a plume at Europa during the Galileo E26 flyby. *Geophysical Research Letters*, 46(3), 1149–1157. <https://doi.org/10.1029/2018GL081544>
- Arnold, H., Liuzzo, L., & Simon, S. (2020). Plasma interaction signatures of plumes at Europa. *Journal of Geophysical Research: Space Physics*, 125(1), e2019JA027346. <https://doi.org/10.1029/2019JA027346>
- Arnold, H., Simon, S., & Liuzzo, L. (2020). Applying ion energy spectrograms to search for plumes at Europa. *Journal of Geophysical Research: Space Physics*, 125(9), e2020JA028376. <https://doi.org/10.1029/2020JA028376>
- Bagenal, F., & Delamere, P. A. (2011). Flow of mass and energy in the magnetospheres of Jupiter and Saturn. *Journal of Geophysical Research*, 116(A5), A05209. <https://doi.org/10.1029/2010JA016294>
- Bagenal, F., & Dols, V. (2020). The space environment of Io and Europa. *Journal of Geophysical Research (Space Physics)*, 125(5), e27485. <https://doi.org/10.1029/2019JA027485>
- Bagenal, F., Sidrow, E., Wilson, R. J., Cassidy, T. A., Dols, V., Cray, F. J., et al. (2015). Plasma conditions at Europa's orbit. *Icarus*, 261, 1–13. <https://doi.org/10.1016/j.icarus.2015.07.036>
- Bagenal, F., Wilson, R. J., Siler, S., Paterson, W. R., & Kurth, W. S. (2016). Survey of Galileo plasma observations in Jupiter's plasma sheet. *Journal of Geophysical Research (Planets)*, 121(5), 871–894. <https://doi.org/10.1002/2016JE005009>
- Breer, B. R., Liuzzo, L., Arnold, H., Andersson, P. N., & Simon, S. (2019). Energetic ion dynamics in the perturbed electromagnetic fields near Europa. *Journal of Geophysical Research: Space Physics*, 124(9), 7592–7613. <https://doi.org/10.1029/2019JA027147>
- Carberry Mogan, S., Johnson, R., Vorburger, A., & Roth, L. (2023). Electron impact ionization in the icy Galilean satellites' atmosphere. *The European Physical Journal D*, 77(2), 26. <https://doi.org/10.1140/epjd/s10053-023-00606-8>
- Cassidy, T., Paranicas, C., Shirley, J., Dalton, J., III, Teolis, B., Johnson, R., et al. (2013). Magnetospheric ion sputtering and water ice grain size at Europa. *Planetary and Space Science*, 77, 64–73. <https://doi.org/10.1016/j.pss.2012.07.008>
- Cervantes, S., & Saur, J. (2022). Constraining Europa's subsolar atmosphere with a joint analysis of HST spectral images and Galileo magnetic field data. *Journal of Geophysical Research (Space Physics)*, 127(9), e30472. <https://doi.org/10.1002/jgra.v127.9>
- Clark, G., Mauk, B. H., Kollmann, P., Paranicas, C., Bagenal, F., Allen, R. C., et al. (2020). Heavy ion charge states in Jupiter's polar magnetosphere inferred from auroral megavolt electric potentials. *Journal of Geophysical Research: Space Physics*, 125(9), e2020JA028052. <https://doi.org/10.1029/2020JA028052>
- Connerney, J. E. P., Acuña, M. H., & Ness, N. F. (1981). Modeling the Jovian current sheet and inner magnetosphere. *Journal of Geophysical Research*, 86(A10), 8370–8384. <https://doi.org/10.1029/JA086iA10p08370>
- Connerney, J. E. P., Acuña, M. H., Ness, N. F., & Satoh, T. (1998). New models of Jupiter's magnetic field constrained by the Io flux tube footprint. *Journal of Geophysical Research*, 103(A6), 11929–11940. <https://doi.org/10.1029/97JA03726>
- Connerney, J. E. P., Timmins, S., Hecceg, M., & Joergensen, J. L. (2020). A Jovian magnetodisc model for the Juno era. *Journal of Geophysical Research: Space Physics*, 125(10), e2020JA028138. <https://doi.org/10.1029/2020JA028138>
- Connerney, J. E. P., Timmins, S., Oliverson, R. J., Espley, J. R., Joergensen, J. L., Kotsiaros, S., et al. (2022). A new model of Jupiter's magnetic field at the completion of Juno's prime mission. *Journal of Geophysical Research: Planets*, 127(2), e2021JE007055. <https://doi.org/10.1029/2021JE007055>
- Cooper, J. F., Johnson, R. E., Mauk, B. H., Garrett, H. B., & Gehrels, N. (2001). Energetic ion and electron irradiation of the icy Galilean satellites. *Icarus*, 149(1), 133–159. <https://doi.org/10.1006/icar.2000.6498>
- Dalton, J. B., Cassidy, T., Paranicas, C., Shirley, J. H., Prockter, L. M., & Kamp, L. W. (2013). Exogenic controls on sulfuric acid hydrate production at the surface of Europa. *Planetary and Space Science*, 77, 45–63. <https://doi.org/10.1016/j.pss.2012.05.013>
- Davis, M. R., Meier, R. M., Cooper, J. F., & Loeffler, M. J. (2021). The contribution of electrons to the sputter-produced O₂ exosphere on Europa. *The Astrophysical Journal*, 908(2), L53. <https://doi.org/10.3847/2041-8213/abe415>
- Desai, R. T., Cowee, M. M., Wei, H., Fu, X., Gary, S. P., Volwerk, M., & Coates, A. J. (2017). Hybrid simulations of positively and negatively charged pickup ions and cyclotron wave generation at Europa. *Journal of Geophysical Research: Space Physics*, 122(10), 10408–10420. <https://doi.org/10.1002/2017JA024479>

- Divine, N., & Garrett, H. B. (1983). Charged particle distributions in Jupiter's magnetosphere. *Journal of Geophysical Research*, 88(A9), 6889–6903. <https://doi.org/10.1029/JA088iA09p06889>
- Eviatar, A., Bar-Nun, A., & Podolak, M. (1985). European surface phenomena. *Icarus*, 61(2), 185–191. [https://doi.org/10.1016/0019-1035\(85\)90100-9](https://doi.org/10.1016/0019-1035(85)90100-9)
- Famà, M., Shi, J., & Baragiola, R. (2008). Sputtering of ice by low-energy ions. *Surface Science*, 602(1), 156–161. <https://doi.org/10.1016/j.susc.2007.10.002>
- Galli, A., Vorbürger, A., Wurz, P., Pommerol, A., Cerubini, R., Jost, B., et al. (2018). 0.2 to 10 keV electrons interacting with water ice: Radiolysis, sputtering, and sublimation. *Planetary and Space Science*, 155, 91–98. <https://doi.org/10.1016/j.pss.2017.11.016>
- Guio, P., Staniland, N. R., Achilleos, N., & Arridge, C. S. (2020). Trapped particle motion in magnetodisk fields. *Journal of Geophysical Research: Space Physics*, 125(7), e2020JA027827. <https://doi.org/10.1029/2020JA027827>
- Hall, D. T., Strobel, D. F., Feldman, P. D., McGrath, M. A., & Weaver, H. A. (1995). Detection of an oxygen atmosphere on Jupiter's moon Europa. *Nature*, 373(6516), 677–679. <https://doi.org/10.1038/373677a0>
- Harris, C. D. K., Jia, X., & Slavin, J. A. (2022). Multi-fluid MHD simulations of Europa's plasma interaction: Effects of variation in Europa's atmosphere. *Journal of Geophysical Research: Space Physics*, 127(9), e2022JA030569. <https://doi.org/10.1029/2022JA030569>
- Harris, C. D. K., Jia, X., Slavin, J. A., Toth, G., Huang, Z., & Rubin, M. (2021). Multi-fluid MHD simulations of Europa's plasma interaction under different magnetospheric conditions. *Journal of Geophysical Research: Space Physics*, 126(5), e2020JA028888. <https://doi.org/10.1029/2020JA028888>
- Hendrix, A. R., Cassidy, T. A., Johnson, R. E., Paranicas, C., & Carlson, R. W. (2011). Europa's disk-resolved ultraviolet spectra: Relationships with plasma flux and surface terrains. *Icarus*, 212(2), 736–743. <https://doi.org/10.1016/j.icarus.2011.01.023>
- Hill, T. W., & Michel, F. C. (1976). Heavy ions from the Galilean satellites and the centrifugal distortion of the Jovian magnetosphere. *Journal of Geophysical Research (1896-1977)*, 81(25), 4561–4565. <https://doi.org/10.1029/JA081i025p04561>
- Hwang, W., Kim, Y. K., & Rudd, M. E. (1996). New model for electron-impact ionization cross sections of molecules. *The Journal of Chemical Physics*, 104(8), 2956–2966. <https://doi.org/10.1063/1.471116>
- Johnson, R. E., Burger, M. H., Cassidy, T. A., Leblanc, F., Marconi, M., & Smyth, W. H. (2009). Composition and detection of Europa's sputter-induced atmosphere. In R. T. Pappalardo, W. B. McKinnon, & K. K. Khurana (Eds.), *Europa* (p. 507).
- Johnson, R. E., Lanzerotti, L. J., & Brown, W. L. (1982). Planetary applications of ion induced erosion of condensed-gas frosts. *Nuclear Instruments and Methods in Physics Research*, 198(1), 147–157. [https://doi.org/10.1016/0167-5087\(82\)90066-7](https://doi.org/10.1016/0167-5087(82)90066-7)
- Kanik, I., Trajmar, S., & Nickel, J. C. (1993). Total electron scattering and electronic state excitations cross sections for O₂, CO, and CH₄. *Journal of Geophysical Research*, 98(E4), 7447–7460. <https://doi.org/10.1029/92JE02811>
- Khurana, K. K. (1997). Euler potential models of Jupiter's magnetospheric field. *Journal of Geophysical Research*, 102(A6), 11295–11306. <https://doi.org/10.1029/97JA00563>
- Khurana, K. K., Leinweber, H. K., Hospodarsky, G. B., & Paranicas, C. P. (2022). Radial and local time variations in the thickness of Jupiter's magnetospheric current sheet. *Journal of Geophysical Research: Space Physics*, 127(10), e2022JA030664. <https://doi.org/10.1029/2022JA030664>
- Kim, T. K., Ebert, R. W., Valek, P. W., Allegrini, F., McComas, D. J., Bagenal, F., et al. (2020). Survey of ion properties in Jupiter's plasma sheet: Juno JADE-I observations. *Journal of Geophysical Research: Space Physics*, 125(4), e2019JA027696. <https://doi.org/10.1029/2019JA027696>
- Kivelson, M. G., Khurana, K. K., Russell, C. T., Volwerk, M., Walker, R. J., & Zimmer, C. (2000). Galileo magnetometer measurements: A stronger case for a subsurface ocean at Europa. *Science*, 289(5483), 1340–1343. <https://doi.org/10.1126/science.289.5483.1340>
- Kivelson, M. G., Khurana, K. K., Stevenson, D. J., Bennett, L., Joy, S., Russell, C. T., et al. (1999). Europa and Callisto: Induced or intrinsic fields in a periodically varying plasma environment. *Journal of Geophysical Research*, 104(A3), 4609–4626. <https://doi.org/10.1029/1998JA000095>
- Kivelson, M. G., Khurana, K. K., & Volwerk, M. (2009). Europa's interaction with the Jovian magnetosphere. In R. T. Pappalardo, W. B. McKinnon, & K. K. Khurana (Eds.), *Europa* (p. 545).
- Kollmann, P., Roussos, E., Paranicas, C., Woodfield, E. E., Mauk, B. H., Clark, G., et al. (2018). Electron acceleration to MeV energies at Jupiter and Saturn. *Journal of Geophysical Research: Space Physics*, 123(11), 9110–9129. <https://doi.org/10.1029/2018JA025665>
- Ligier, N., Poulet, F., Carter, J., Brunetto, R., & Gourgout, F. (2016). VLT/SINFONI observations of Europa: New insights into the surface composition. *The Astrophysical Journal*, 151(6), 163. <https://doi.org/10.3847/0004-6256/151/6/163>
- Lindsay, B. G., & Stebbings, R. F. (2005). Charge transfer cross sections for energetic neutral atom data analysis. *Journal of Geophysical Research*, 110(A12), A12213. <https://doi.org/10.1029/2005JA011298>
- Liuzzo, L., Feyerabend, M., Simon, S., & Motschmann, U. (2015). The impact of Callisto's atmosphere on its plasma interaction with the Jovian magnetosphere. *Journal of Geophysical Research: Space Physics*, 120(11), 9401–9427. <https://doi.org/10.1002/2015JA021792>
- Liuzzo, L., Paty, C., Cochrane, C., Nordheim, T., Luspay-Kuti, A., Castillo-Rogez, J., et al. (2021). Triton's variable interaction with Neptune's magnetospheric plasma. *Journal of Geophysical Research: Space Physics*, 126(11), e2021JA029740. <https://doi.org/10.1029/2021JA029740>
- Liuzzo, L., Poppe, A. R., Addison, P., Simon, S., Nénon, Q., & Paranicas, C. (2022). Energetic magnetospheric particle fluxes onto Callisto's atmosphere. *Journal of Geophysical Research: Space Physics*, 127(11), e2022JA030915. <https://doi.org/10.1029/2022JA030915>
- Liuzzo, L., Poppe, A. R., Paranicas, C., Nénon, Q., Fatemi, S., & Simon, S. (2020). Variability in the energetic electron bombardment of Gany-mede. *Journal of Geophysical Research: Space Physics*, 125(9), e2020JA028347. <https://doi.org/10.1029/2020JA028347>
- Liuzzo, L., Simon, S., & Feyerabend, M. (2018). Observability of Callisto's inductive signature during the Jupiter ICy moons explorer mission. *Journal of Geophysical Research: Space Physics*, 123(11), 9045–9054. <https://doi.org/10.1029/2018JA025951>
- Liuzzo, L., Simon, S., Feyerabend, M., & Motschmann, U. (2016). Disentangling plasma interaction and induction signatures at Callisto: The Galileo C10 flyby. *Journal of Geophysical Research: Space Physics*, 121(9), 8677–8694. <https://doi.org/10.1002/2016JA023236>
- Liuzzo, L., Simon, S., Feyerabend, M., & Motschmann, U. (2017). Magnetic signatures of plasma interaction and induction at Callisto: The Galileo C21, C22, C23, and C30 flybys. *Journal of Geophysical Research: Space Physics*, 122(7), 7364–7386. <https://doi.org/10.1002/2017JA024303>
- Liuzzo, L., Simon, S., & Regoli, L. (2019a). Energetic electron dynamics near Callisto. *Planetary and Space Science*, 179, 104726. <https://doi.org/10.1016/j.pss.2019.104726>
- Liuzzo, L., Simon, S., & Regoli, L. (2019b). Energetic ion dynamics near Callisto. *Planetary and Space Science*, 166, 23–53. <https://doi.org/10.1016/j.pss.2018.07.014>
- Ma, Q., Li, W., Zhang, X.-J., Shen, X.-C., Daly, A., Bortnik, J., et al. (2021). Energetic electron distributions near the magnetic equator in the Jovian plasma sheet and outer radiation belt using Juno observations. *Geophysical Research Letters*, 48(24), e2021GL095833. <https://doi.org/10.1029/2021GL095833>
- Matsumoto, H., & Omura, Y. (1985). Particle simulation of electromagnetic waves and its application to space plasmas. *Computer Simulation of Space Plasmas*, 43.
- Mauk, B. H., Mitchell, D. G., McEntire, R. W., Paranicas, C. P., Roelof, E. C., Williams, D. J., & Lagg, A. (2004). Energetic ion characteristics and neutral gas interactions in Jupiter's magnetosphere. *Journal of Geophysical Research*, 109(A9), A09S12. <https://doi.org/10.1029/2003JA010270>

- McEwen, A. S. (1986). Exogenic and endogenic albedo and color patterns on Europa. *Journal of Geophysical Research*, 91(B8), 8077–8097. <https://doi.org/10.1029/JB091iB08p08077>
- Meier, R. M., & Loeffler, M. J. (2020). Sputtering of water ice by keV electrons at 60 K. *Surface Science*, 691, 121509. <https://doi.org/10.1016/j.susc.2019.121509>
- Momoki, N., & Toh, H. (2022). Updated model parameters of current sheet and magnetic field in the Jovian magnetosphere for pre-Galileo, Galileo and Juno eras. *Journal of Geophysical Research: Planets*, 127(11), e2022JE007493. <https://doi.org/10.1029/2022JE007493>
- Moore, K. M., Yadav, R. K., Kulowski, L., Cao, H., Bloxham, J., Connerney, J. E. P., et al. (2018). A complex dynamo inferred from the hemispheric dichotomy of Jupiter's magnetic field. *Nature*, 561(7721), 76–78. <https://doi.org/10.1038/s41586-018-0468-5>
- Müller, J., Simon, S., Motschmann, U., Schüle, J., Glassmeier, K.-H., & Pringle, G. J. (2011). A.I.K.E.F.: Adaptive hybrid model for space plasma simulations. *Computer Physics Communications*, 182(4), 946–966. <https://doi.org/10.1016/j.cpc.2010.12.033>
- Nénon, Q., & André, N. (2019). Evidence of Europa neutral gas Torii from energetic sulfur ion measurements. *Geophysical Research Letters*, 46(7), 3599–3606. <https://doi.org/10.1029/2019GL082200>
- Nénon, Q., Miller, L. P., Kollmann, P., Liuzzo, L., Pinto, M., & Witasse, O. (2022). Pitch angle distribution of MeV electrons in the magnetosphere of Jupiter. *Journal of Geophysical Research: Space Physics*, 127(8), e2022JA030627. <https://doi.org/10.1029/2022JA030627>
- Nénon, Q., Sicard, A., Kollmann, P., Garrett, H. B., Sauer, S. P. A., & Paranicas, C. (2018). A physical model of the proton radiation belts of Jupiter inside Europa's orbit. *Journal of Geophysical Research: Space Physics*, 123(5), 3512–3532. <https://doi.org/10.1029/2018JA025216>
- Neubauer, F. M. (1980). Nonlinear standing Alfvén wave current system at Io - theory. *Journal of Geophysical Research*, 85(A3), 1171–1178. <https://doi.org/10.1029/JA085iA03p01171>
- Neubauer, F. M. (1998). The sub-Alfvénic interaction of the Galilean satellites with the Jovian magnetosphere. *Journal of Geophysical Research*, 103(E9), 19843–19866. <https://doi.org/10.1029/97JE03370>
- Neubauer, F. M. (1999). Alfvén wings and electromagnetic induction in the interiors: Europa and Callisto. *Journal of Geophysical Research*, 104(A12), 28671–28684. <https://doi.org/10.1029/1999JA900217>
- Nordheim, T. A., Hand, K. P., & Paranicas, C. (2018). Preservation of potential biosignatures in the shallow subsurface of Europa. *Nature Astronomy*, 2(8), 673–679. <https://doi.org/10.1038/s41550-018-0499-8>
- Nordheim, T. A., Regoli, L. H., Harris, C. D. K., Paranicas, C., Hand, K. P., & Jia, X. (2022). Magnetospheric ion bombardment of Europa's surface. *Planetary Science Journal*, 3(1), 5. <https://doi.org/10.3847/PSJ/ac382a>
- Orlando, T. M., & Sieger, M. T. (2003). The role of electron-stimulated production of O₂ from water ice in the radiation processing of outer solar system surfaces. *Surface Science*, 528(1), 1–7. [https://doi.org/10.1016/S0039-6028\(02\)02602-X](https://doi.org/10.1016/S0039-6028(02)02602-X)
- Paranicas, C., Carlson, R. W., & Johnson, R. E. (2001). Electron bombardment of Europa. *Geophysical Research Letters*, 28(4), 673–676. <https://doi.org/10.1029/2000GL012320>
- Paranicas, C., Cooper, J. F., Garrett, H. B., Johnson, R. E., & Sturmer, S. J. (2009). Europa's radiation environment and its effects on the surface. In R. T. Pappalardo, W. B. McKinnon, & K. K. Khurana (Eds.), *Europa* (p. 529).
- Paranicas, C., McEntire, R. W., Cheng, A. F., Lagg, A., & Williams, D. J. (2000). Energetic charged particles near Europa. *Journal of Geophysical Research*, 105(A7), 16005–16015. <https://doi.org/10.1029/1999JA000350>
- Paranicas, C., Ratliff, J. M., Mauk, B. H., Cohen, C., & Johnson, R. E. (2002). The ion environment near Europa and its role in surface energetics. *Geophysical Research Letters*, 29(5), 18-1–18-4. <https://doi.org/10.1029/2001GL014127>
- Patterson, G. W., Paranicas, C., & Prockter, L. M. (2012). Characterizing electron bombardment of Europa's surface by location and depth. *Icarus*, 220(1), 286–290. <https://doi.org/10.1016/j.icarus.2012.04.024>
- Phipps, P., & Bagenal, F. (2021). Centrifugal equator in Jupiter's plasma sheet. *Journal of Geophysical Research: Space Physics*, 126(1), e2020JA028713. <https://doi.org/10.1029/2020JA028713>
- Plainaki, C., Cassidy, T. A., Shematovich, V. I., Milillo, A., Wurz, P., Vorbürger, A., et al. (2018). Towards a global unified model of Europa's tenuous atmosphere. *Space Science Reviews*, 214(1), 40. <https://doi.org/10.1007/s11214-018-0469-6>
- Plainaki, C., Milillo, A., Mura, A., Saur, J., Orsini, S., & Massetti, S. (2013). Exospheric O₂ densities at Europa during different orbital phases. *Planetary and Space Science*, 88, 42–52. <https://doi.org/10.1016/j.pss.2013.08.011>
- Poppe, A. R., Fatemi, S., & Khurana, K. K. (2018). Thermal and energetic ion dynamics in Ganymede's magnetosphere. *Journal of Geophysical Research: Space Physics*, 123(6), 4614–4637. <https://doi.org/10.1029/2018JA025312>
- Regoli, L. H., Roussos, E., Feyerabend, M., Jones, G. H., Krupp, N., Coates, A. J., et al. (2016). Access of energetic particles to Titan's exobase: A study of Cassini's T9 flyby. *Planetary and Space Science*, 130, 40–53. <https://doi.org/10.1016/j.pss.2015.11.013>
- Roederer, J. G. (1967). On the adiabatic motion of energetic particles in a model magnetosphere. *Journal of Geophysical Research (1896-1977)*, 72(3), 981–992. <https://doi.org/10.1029/JZ072i003p00981>
- Roth, L. (2021). A stable H₂O atmosphere on Europa's trailing hemisphere from HST images. *Geophysical Research Letters*, 48(20), e2021GL094289. <https://doi.org/10.1029/2021GL094289>
- Roth, L., Retherford, K. D., Ivchenko, N., Schlatter, N., Strobel, D. F., Becker, T. M., & Grava, C. (2017). Detection of a hydrogen Corona in HST Ly α images of Europa in transit of Jupiter. *The Astrophysical Journal*, 153(2), 67. <https://doi.org/10.3847/1538-3881/153/2/67>
- Roth, L., Retherford, K. D., Saur, J., Strobel, D. F., Feldman, P. D., McGrath, M. A., & Nimmo, F. (2014). Orbital apocenter is not a sufficient condition for HST/STIS detection of Europa's water vapor aurora. *Proceedings of the National Academy of Sciences*, 111(48), E5123–E5132. <https://doi.org/10.1073/pnas.1416671111>
- Roth, L., Saur, J., Retherford, K. D., Strobel, D. F., Feldman, P. D., McGrath, M. A., et al. (2016). Europa's far ultraviolet oxygen aurora from a comprehensive set of HST observations. *Journal of Geophysical Research: Space Physics*, 121(3), 2143–2170. <https://doi.org/10.1002/2015JA022073>
- Rubin, M., Jia, X., Altwegg, K., Combi, M. R., Daldorff, L. K. S., Gombosi, T. I., et al. (2015). Self-consistent multifluid MHD simulations of Europa's exospheric interaction with Jupiter's magnetosphere. *Journal of Geophysical Research: Space Physics*, 120(5), 3503–3524. <https://doi.org/10.1002/2015JA021149>
- Saur, J., Duling, S., Roth, L., Jia, X., Strobel, D. F., Feldman, P. D., et al. (2015). The search for a subsurface ocean in Ganymede with Hubble Space Telescope observations of its auroral ovals. *Journal of Geophysical Research: Space Physics*, 120(3), 1715–1737. <https://doi.org/10.1002/2014JA020778>
- Saur, J., Neubauer, F. M., & Glassmeier, K.-H. (2010). Induced magnetic fields in solar system bodies. *Space Science Reviews*, 152(1–4), 391–421. <https://doi.org/10.1007/s11214-009-9581-y>
- Saur, J., Strobel, D. F., & Neubauer, F. M. (1998). Interaction of the Jovian magnetosphere with Europa: Constraints on the neutral atmosphere. *Journal of Geophysical Research*, 103(E9), 19947–19962. <https://doi.org/10.1029/97JE03556>
- Schilling, N., Neubauer, F. M., & Saur, J. (2007). Time-varying interaction of Europa with the Jovian magnetosphere: Constraints on the conductivity of Europa's subsurface ocean. *Icarus*, 192(1), 41–55. <https://doi.org/10.1016/j.icarus.2007.06.024>

- Schulz, M., & Lanzerotti, L. J. (1974). Particle diffusion in the radiation belts. <https://doi.org/10.1007/978-3-642-65675-0>
- Shen, X.-C., Li, W., Ma, Q., Nishimura, Y., Daly, A., Kollmann, P., et al. (2022). Energetic proton distributions in the inner and middle magnetosphere of Jupiter using Juno observations. *Geophysical Research Letters*, 49(16), e2022GL099832. <https://doi.org/10.1029/2022GL099832>
- Shprits, Y. Y., Menietti, J. D., Drozdov, A. Y., Horne, R. B., Woodfield, E. E., Groene, J. B., et al. (2018). Strong whistler mode waves observed in the vicinity of Jupiter's moons. *Nature Communications*, 9(1), 3131. <https://doi.org/10.1038/s41467-018-05431-x>
- Simon, S., Addison, P., & Liuzzo, L. (2022). Formation of a displaced plasma wake at Neptune's moon triton. *Journal of Geophysical Research: Space Physics*, 127(1), e2021JA029958. <https://doi.org/10.1029/2021JA029958>
- Simon, S., Liuzzo, L., & Addison, P. (2021). Role of the ionospheric conductance profile in sub-Alfvénic moon-magnetosphere interactions: An analytical model. *Journal of Geophysical Research: Space Physics*, 126(7), e2021JA029191. <https://doi.org/10.1029/2021JA029191>
- Simon, S., van Treeck, S. C., Wennmacher, A., Saur, J., Neubauer, F. M., Bertucci, C. L., & Dougherty, M. K. (2013). Structure of Titan's induced magnetosphere under varying background magnetic field conditions: Survey of Cassini magnetometer data from flybys TA-T85. *Journal of Geophysical Research (Space Physics)*, 118(4), 1679–1699. <https://doi.org/10.1002/jgra.50096>
- Smith, H. T., Mitchell, D. G., Johnson, R. E., Mauk, B. H., & Smith, J. E. (2019). Europa neutral torus confirmation and Characterization based on observations and modeling. *The Astrophysical Journal*, 871(1), 69. <https://doi.org/10.3847/1538-4357/aad38>
- Smyth, W. H., & Marconi, M. L. (2006). Europa's atmosphere, gas tori, and magnetospheric implications. *Icarus*, 181(2), 510–526. <https://doi.org/10.1016/j.icarus.2005.10.019>
- Spencer, J. R., Tampari, L. K., Martin, T. Z., & Travis, L. D. (1999). Temperatures on Europa from Galileo photopolarimeter-radiometer: Night-time thermal anomalies. *Science*, 284(5419), 1514–1516. <https://doi.org/10.1126/science.284.5419.1514>
- Teolis, B. D., Plainaki, C., Cassidy, T. A., & Raut, U. (2017). Water ice radiolytic O₂, H₂, and H₂O₂ yields for any projectile species, energy, or temperature: A model for icy astrophysical bodies. *Journal of Geophysical Research: Planets*, 122(10), 1996–2012. <https://doi.org/10.1002/2017JE005285>
- Truscott, P., Heynderickx, D., Sicard-Piet, A., & Bourdarie, S. (2011). Simulation of the radiation environment near Europa using the Geant4-based PLANETOCOSMICS-J model. *IEEE Transactions on Nuclear Science*, 58(6), 2776–2784. <https://doi.org/10.1109/TNS.2011.2172818>
- Vance, S., Styczinski, M. J., Bills, B. G., Cochrane, C. J., Soderlund, K. M., Gómez-Pérez, N., & Paty, C. (2021). Magnetic induction responses of Jupiter's ocean moons including effects from adiabatic convection. *Journal of Geophysical Research (Planets)*, 126(2), e06418. <https://doi.org/10.1029/2020JE006418>
- Vay, J.-L. (2008). Simulation of beams or plasmas crossing at relativistic velocity. *Physics of Plasmas*, 15(5), 056701. <https://doi.org/10.1063/1.2837054>
- Volwerk, M., Kivelson, M. G., & Khurana, K. K. (2001). Wave activity in Europa's wake: Implications for ion pickup. *Journal of Geophysical Research*, 106(A11), 26033–26048. <https://doi.org/10.1029/2000JA000347>
- Vorburger, A., & Wurz, P. (2018). Europa's ice-related atmosphere: The sputter contribution. *Icarus*, 311, 135–145. <https://doi.org/10.1016/j.icarus.2018.03.022>
- Wang, J.-z., Huo, Z.-x., & Zhang, L. (2021). A modular model of Jupiter's magnetospheric magnetic field based on Juno data. *Journal of Geophysical Research: Space Physics*, 126(5), e2020JA029085. <https://doi.org/10.1029/2020JA029085>
- Williams, D. J., & Mauk, B. (1997). Pitch angle diffusion at Jupiter's moon Ganymede. *Journal of Geophysical Research*, 102(A11), 24283–24287. <https://doi.org/10.1029/97JA02260>
- Ziegler, J., & Manoyan, J. (1988). The stopping of ions in compounds. *Nuclear Instruments and Methods in Physics Research Section B: Beam Interactions with Materials and Atoms*, 35(3), 215–228. [https://doi.org/10.1016/0168-583X\(88\)90273-X](https://doi.org/10.1016/0168-583X(88)90273-X)
- Zimmer, C., Khurana, K. K., & Kivelson, M. G. (2000). Subsurface oceans on Europa and Callisto: Constraints from Galileo magnetometer observations. *Icarus*, 147(2), 329–347. <https://doi.org/10.1006/icar.2000.6456>